**Chemical Geology**
May 2021, Volume 568, Pages 120126 (28p.)
https://doi.org/10.1016/j.chemgeo.2021.120126
https://archimer.ifremer.fr/doc/00680/79215/



# When a mid-ocean ridge encroaches a continent: Seafloor-type hydrothermal activity in Lake Asal (Afar Rift)

Dekov V.M. [1, *], Guéguen B. [2, 3], Yamanaka T. [1], Moussa N. [4], Okumura T. [5], Bayon Germain [6], Liebetrau V. [7], Yoshimura T. [8], Kamenov G. [9], Araoka D. [10], Makita H. [1], Sutton Jill [11]

[1] Department of Ocean Sciences, Tokyo University of Marine Science and Technology, 4-5-7 Konan, Minato-ku, Tokyo 108-8477, Japan
[2] CNRS, Univ Brest, UMR 6538 Laboratoire Géosciences Océan, F-29280 Plouzané, France
[3] CNRS, Univ Brest, UMS 3113, F-29280 Plouzané, France
[4] IST, Centre d'Etude et de Recherche de Djibouti (CERD), BP 486, Route de l'Aéroport, Djibouti
[5] Center for Advanced Marine Core Research, Kochi University, 200 Monobe-Otsu, Nankoku, Kochi 783-8502, Japan
[6] IFREMER, Marine Geosciences Unit, 29280 Plouzané, France
[7] Helmholtz Centre for Ocean Research Kiel, GEOMAR, Wischhofstr. 1-3, D-24124 Kiel, Germany
[8] Japan Agency for Marine-Earth Science and Technology (JAMSTEC), Research Institute for Marine Resources Utilization, Biogeochemistry Program, 2-15 Natsushima-cho, Yokosuka-city, Kanagawa, 237-0061, Japan
[9] Department of Geological Sciences, University of Florida, 241 Williamson Hall, Gainesville, FL 32611, USA
[10] Geological Survey of Japan (GSJ), National Institute of Advanced Industrial Science and Technology (AIST), Central-7, 1-1-1 Higashi, Tsukuba, Ibaraki 305-8567, Japan
[11] Univ Brest, CNRS, IRD, Ifremer, Institut Universitaire Européen de la Mer, LEMAR, Rue Dumont d'Urville, 29280 Plouzané, France

* Corresponding author : V. M. Dekov, email address : vdekov0@kaiyodai.ac.jp

**Abstract :**

At the place where the submarine Aden Ridge encroaches on the African continent and interacts with the East African Rift system, two small basins form: Ghoubbet-al-Kharab and Lake Asal. Whereas Ghoubbet-al-Kharab is connected to the open ocean, Lake Asal is a typical example of oceanic “embryo”, which is defined as a system that is detached from the ocean, but has features of a marine basin with an oceanic type crust and a seawater-based water body. In order to shed light on the source of water, type of hydrothermal activity and hydrothermal deposits, and controls on the water chemistry in an oceanic “embryo”, we undertook a mineralogical-geochemical study of the lake water, hydrothermal fluids and hydrothermal carbonate deposits of Lake Asal. The geochemical analyses of lake water and hydrothermal fluids show that Lake Asal (located in an arid zone with strong evaporation and with no riverine input) is fed by seafloor-type hydrothermal fluids according to the following scenario: percolation of seawater along faults and cracks of extension in the rift, reaction of seawater with the hot basaltic rocks and hydrothermal fluid generation, discharge of the hydrothermal fluid in the Asal depression and accumulation of the Lake Asal water body. The fluid venting at the Lake Asal bottom is a mixture of 97% end-member hydrothermal fluid and 3% lake water. The calculated end-member hydrothermal fluid of this oceanic “embryo” is poorer in metals than the seafloor hydrothermal fluids of an open and evolved ocean. In addition to the

seawater/rock interaction, the chemistry of Lake Asal is also controlled by evaporation leading to hyper salinity. In a hyper saline water body a number of hydrothermally supplied metals are stabilized as chloride complexes and accumulate. This results in a metal rich and mildly acidic “embryonic” ocean. Unlike an open and evolved modern ocean, the “embryonic” ocean located in an arid zone has heavy C and O isotope composition and light Zn and Fe isotope composition. Calcium isotope compositions of both types of ocean are similarly heavy. There are two genetically different sources of elements to the Lake Asal that are vertically separated: hydrothermal (lower, or bottom) and aeolian (upper, or surficial). Another important control on the lake water chemistry is the formation of carbonate spires at the lake bottom. Ca-carbonate precipitation immobilizes substantial amount of hydrothermally supplied Ca and drives up the (Mg/Ca)mol of the lake water. Increasing (Mg/Ca)mol of the evolving lake water leads to changes in the mineralogy of spires: from low-Mg calcite to aragonite. Thus, the spire formation exerts a self-control on its mineralogy. Carbonate spire deposition affects also the Ca, Zn and Fe isotope composition of the lake water through adsorption or/and co-precipitation induced isotope fractionation.

**Highlights**

► Lake Asal (Afar Rift) is fed by seafloor-type hydrothermal fluids. ► An oceanic “embryo” in arid climate is mildly acidic and metal rich. ► It has heavy C, O and Ca, and light Zn isotope composition. ► Lake chemistry is controlled by hydrothermal discharge and aeolian input.

**Keywords** : Asal Rift, carbonate spires, C-O-Ca-Fe-Zn-Sr-U-Th isotopes, continental rift, “embryonic” ocean, seafloor hydrothermal activity

## 1. Introduction

At present we have extensive understanding of the hydrothermal processes and related mineral deposits at all tectonic settings in the open ocean: mid-ocean ridges, volcanic arcs, back-arc spreading centers, and hot spots (German and Von Damm, 2004). Our knowledge of the same type of processes and deposits at continental rift setting is also substantial (Tiercelin et al., 1993; Benson, 1994; Pflumio et al., 1994; Barrat et al., 2000; Rosen et al., 2004; Branchu et al., 2005; Granina et al., 2007; Renaut et al., 2013; Dekov et al., 2014). However, the hydrothermal processes and deposits at the transition from continental rifting to oceanic spreading in *sensu stricto*, at the point of mid-ocean ridge encroachment on a continent where oceanic "embryos" form on land, are not well understood. In fact, there is only one place on Earth where this happens: the Asal Rift (East Africa) (Fig. 1 A). The Asal Rift, a part of the Asal-Ghoubbet Rift (Fig. 1 A), forms where the submarine Aden Ridge impinges on the continent and interacts with the continental East African Rift system. Two small basins form at the point of impingement: Ghoubbet-al-Kharab and Lake Asal (Fig. 1 A). The Ghoubbet-al-Kharab is a semi-closed basin connected with the ocean (Bäcker et al., 1973) whereas Lake Asal is a landlocked hypersaline (~300‰) basin with a dense network of hydrothermal manifestations around it (Gasse and Fontes, 1989).

The scarce knowledge on these processes and deposits motivated us to undertake mineralogical and geochemical investigations at this oceanic "embryo" in order to answer three major questions: (1) What is the source of water in an oceanic "embryo" isolated from the ocean with no riverine supply and where evaporation is dominant over rainfall?, (2) What is the type of hydrothermal activity and deposits at the transitional setting of continental rifting – oceanic spreading?, and (3) What are the major controls on the chemistry of an ocean at the "embryonic" stage?

## 2. Geological setting

The Aden Ridge, a ridge system in the NW Indian Ocean that separates the Arabian and Somalian plates, is known to have propagated westward to the western tip of the Gulf of Tadjoura where it encroaches on the African continent (Courtillot et al., 1980, 1984; Manighetti et al.,

1998). Here, at the Afar region, the Red Sea spreading ridge has also jumped on land. Both spreading ridges meet the East African Rift and form a triple junction between the separating Arabian, Somalian and Nubian plates (Manighetti et al., 1998). Over the past 30 million years the rifting in the Afar region has evolved from continental extension to nascent seafloor spreading (Audin et al., 2004; Bastow and Keir, 2011; Wright et al., 2012).

Tadjoura Rift (Fig. 1 A) is the last submarine segment of the Aden Ridge. The first segment of the ridge that is exposed above sea level is the Asal-Ghoubbet Rift (Fig. 1 A). Morphologically, it is a NW-SE striking graben bounded by steep, inward dipping normal fault scarps (Stein et al., 1991) (Fig. 1 A,B). According to its crustal structure, magmatic processes, and tectonics, the Asal-Ghoubbet Rift is similar to slow-spreading ridges (Barberi et al., 1972; Needham et al., 1976; Manighetti et al., 1998). It is currently opening at 16 ± 1 mm/yr (Vigny et al., 2007) and propagates northwestward (Manighetti et al., 1998).

The crust of the Asal Rift is dominantly basaltic (Barrat et al., 1993). Volcanism in and around the Asal Rift is a tectonically-controlled association of typical oceanic basaltic volcanism (along the rift axis) and typical continental rift volcanism (on both sides of the rift axial zone) (Barberi et al., 1972). Early studies (Stieltjes, 1975) inferred that this volcanism is fed by a magma chamber still present below the central part of the rift. Recent seismological investigations (Doubre et al., 2007) showed that the central Fieale-Shark Bay volcanic complex is an important element of the rift plumbing system. The Fieale and Shark Bay calderas were inferred to overlay a ~2-km-wide pipe of hot rocks above a deeper (>5-6 km) magma chamber. This conclusion is supported by endogenous heat studies in geothermal wells in the Asal Rift revealing temperatures of up to 358°C at ~2000 m depth (Zan et al., 1990). The dominantly basaltic crust of the rift between the Lake Asal and Ghoubbet-al-Kharab is cut by clusters of open fissures (up to several meters wide) parallel to the normal faults (Vellutini, 1990; Manighetti et al., 1998) and therefore, the crust appears to be highly permeable.

## 3. Samples

During two sampling campaigns at the Afar Rift (Republic of Djibouti) in April and November 2017, we collected two major types of samples from the Lake Asal: fluids and carbonate spires (Fig. 1 A,B). For comparison, we collected the same types of samples from the

Lake Abhé (Fig. 1 A,B): a lake located in a continental rift setting, in arid zone with dominance of evaporation over rainfall, but fed by river water (Awash River) (Dekov et al., 2014). In addition to these samples we also collected samples from the local basalts (Site 6, Lake Asal; Fig. 1 B) and salts precipitated at the Lake Asal bottom (Site 4; Fig. 1 B).

The fluid samples were of three sub-types: lake water, hot spring water (hydrothermal fluid) and seawater (Table 1). Seawater from Ghoubbet-al-Kharab (Fig. 1 B, Table 1) was sampled as a baseline for our fluid study. Lake water samples were collected at sites close to the lake shores and along two vertical profiles (C1 and C2) across the Lake Asal water body (Table 1; Fig. 1 A,B). Hydrothermal fluids were collected from hot springs jetting at the lake shores. After preliminary measurement of some basic physical-chemical parameters of the sampled fluids (pH, T, alkalinity, density, dissolved oxygen and dissolved inorganic carbon; Table 1) we focused our further studies on a refined selection of samples: (1) seawater; (2) Lake Asal (lake water from both vertical profiles across the lake, two hydrothermal fluids); (3) Lake Abhé (one lake water and two hydrothermal fluid samples).

The fluid samples were collected with both 50 mL syringes (TERUMO; cleaned with ultrapure $HNO_3$) (seawater, hydrothermal fluids and nearshore lake water) and standard 5 L Niskin bottle (lake water vertical profiles). Immediately after sample recovery 100 mL of each sample were filtered (0.2 μm, 25 mm, PTFE; HPLC Millex), transferred into 100 mL HDPE bottles, acidified to pH<2 (with ultrapure 6*M* HCl) and sealed (Parafilm) until lab processing and analyses.

Tips of spires standing at the shores of both lakes (Figs 1 A,B; 2 A,B) and close to the shoreline were sampled (one from each lake) for investigations. We collected samples (~4 g) from the macroscopically different layers of the spires after cross-cutting them and using a diamond mini drill (Fig. 3 A,B). The spire samples along with those of basalt and salt were ground into fine powders in an agate mortar for further analyses. Thin polished sections from the same cross-sections were prepared for optical microscopy observations.

## 4. Methods of investigation

### *4.1. Mineralogy investigations of the spires*

We investigated the mineralogy and texture of the spires (thin polished sections) with optical polarizing microscope (Eclipse LV100N POL, Nikon). After the observations of the thin sections in transmitted light and acquiring of photographs we stained the same thin sections with Feigl's solution (Friedman, 1959) in order to distinguish between aragonite and calcite and document the spatial relations between them.

The bulk mineralogy of the different internal layers of the spires was studied by X-ray diffractometry (XRD) (PANalytical B.V. X'Pert PRO MPD X-ray diffractometer with monochromatic Cu $K_\alpha$ radiation, graphite monochromator, 45 kV, 40 mA) of random powder mounts: scans from 10 to 75 °2θ, with steps of 0.008 °2θ, at 10 s/step. Obtained XRD patterns were compared with established peak sets using X'Pert HighScore Plus software to determine mineralogical composition of the samples. The amount of $MgCO_3$ (in mol. %) in the calcite crystal lattice was calculated using $d_{104}$ values of the XRD patterns recorded from 20 to 40 °2θ, with steps of 0.02 °2θ, at 1.5 s/step (Rigaku Ultima IV X-ray diffractometer with monochromatic Cu $K_\alpha$ radiation, MacDiff software).

*4.2. Elemental concentrations measurement in the spires, basalt and salt*

Major elements concentrations in the basalt and salt samples were measured by X-ray fluorescence (XRF) at the Geological Survey of Japan (GSJ) of the National Institute of Advanced Industrial Science and Technology (AIST) in Japan. For the XRF analysis glass beads were prepared by mixing 0.5 g of powdered sample with 5.0 g of lithium tetraborate flux. The mixture was heated to 1200°C for 10 min in a 95% Pt-5% Au crucible using a semi-automatic fusion device HAG-M-HF (Herzog). Ten major elements ($SiO_2$, $TiO_2$, $Al_2O_3$, total $Fe_2O_3$, MnO, MgO, CaO, $Na_2O$, $K_2O$, and $P_2O_5$) were quantified by an X-ray fluorescence instrument ZSX Primus III+ (Rigaku) with an Rh tube. The calibration curves of each element were prepared using GSJ geochemical reference samples with their chemical compositions varying from mafic to felsic. The accuracy was verified each day using two GSJ geochemical reference samples: JB-1b and JG-3. The analytical uncertainties for each element were better than 1.5%, as estimated from the long-term reproducibility of the measurements of JB-1b (Morita et al., 2016; Damak et al., 2019).

The concentrations of Al, Mg, Ti, P, Fe, Mn, Sr, Ba, Rb, Li, Cu, Co, Ni, V, Zn, Pb, Cd, Mo, Tl, Cr, W, Ga, Sc, Hf, Th, U, Y and rare earth elements (REE) in the spire, basalt and salt samples were measured by High Resolution-Inductively Coupled Plasma-Mass Spectrometry (HR-ICP-MS). Between 80 and 100 mg of powdered samples were weighted in PTFE vials and dissolved using a mixture of HF-$HNO_3$. The solutions were evaporated to dryness and re-dissolved in aqua regia. After evaporation, the residues were dissolved in 5 mL 6 *M* HCl for archiving. Splits of 100 µL from the archive solutions were taken in HDPE vials and diluted in 5 mL ~0.28 *M* $HNO_3$ for HR-ICP-MS measurements. Two geostandards (BHVO-2 and CAL-S) and a procedural blank were prepared along with the samples following the same dissolution protocol. Elemental concentrations in the sample solutions (in ~0.28 *M* $HNO_3$) were measured with a HR-ICP-MS Element XR (ThermoFisher Scientific) at the Pôle de Spectrométrie Océan (PSO) (IUEM/Ifremer, Brest, France) using indium as an internal standard for drift signal correction. Concentrations were calibrated using external calibration standards prepared for the measurements. Results on the geostandards were within the range published in the literature.

For Si concentrations measurements in the spires we processed the powdered spire samples following the protocol detailed in Ragueneau et al. (2005). This method transforms the silica into dissolved silica, permitting its analysis by a continuous flow auto-analyzer at a wavelength of 820 nm (SEAL-BRAN+LUEBBE AA3 HR auto-analyzer). The method used to analyze the Si concentration in the dissolved silica (spire and fluid samples) is based on the reaction of silicates with molybdate (pH = 1.5) to form the β-silicomolybdic complex, which is reduced by ascorbic acid to form a blue compound (Aminot and Kérouel, 2007). We used a Si concentration standard (Certipur) ranging from 0 to 60 µM in an 18.2 MΩ water based solution. The standard deviation of the analyses within this range was ≤0.5%.

*4.3. Basic physical-chemical parameters of the fluids*

Temperature (T), pH and dissolved oxygen (DO) of the fluids were measured *in situ* immediately after sampling using electrodes (D-55; Horiba Ltd.). Alkalinity of the fluids was determined by titration with 0.05 *N* $H_2SO_4$ (Bromocresol Green–Methyl Red method) within 5 hours after sampling. The fluid density was determined by weighing of constant-volume (100-200 µL) samples and 18.2 MΩ water (10-20 replicates) at laboratory temperature (~22°C).

Dissolved inorganic carbon (DIC) concentrations in the fluid samples were calculated with the computer program PHREEQC version 3 (Parkhurst and Appelo, 2013) using the measured fluid chemical composition, pH and temperature.

*4.4. Elemental concentrations measurement in the fluids*

*4.4.1. Major elements*

Major cations ($Na^+$, $K^+$, $Mg^{2+}$, $Ca^{2+}$) and anions ($Cl^-$ and $SO_4^{2-}$) concentrations in the fluids were measured using an ion chromatograph ICS-1600 (DIONEX). Bromide ($Br^-$) and $NO_3^-$ concentrations in the fluids were measured by a high-performance liquid chromatograph according to the procedure described by Maruo et al. (2006).

Silicon concentrations in the fluids were analyzed following the method described in *4.2*.

*4.4.2. Lithium and Sr*

Lithium and Sr concentrations in the fluids were measured by quadrupole inductively coupled plasma mass spectrometry (ICP-MS) iCAP Q (ThermoFisher Scientific) at the Japan Agency for Marine-Earth Science and Technology. Prior to analysis by ICP-MS, the fluid samples were diluted in polypropylene vials, followed by the addition of 0.3 *M* $HNO_3$ (Tamapure AA-100) to each vial. To control for instrument drift, internal standards for Be, Sc, Y, and In were used. Laboratory standard solutions were measured after every fifth sample for data correction purposes. The reproducibility of the measurements of each element were better than 5% (2 RSD), estimated by repeated measurements of standard solutions (Araoka and Yoshimura, 2019).

*4.4.3. Iron, Mn, Co, Ni, Cu, Zn, Cd, Mo, Pb, Ag, Sn, U, V, Y and REE*

Since most of the studied fluid samples were highly saline a direct and simple analysis of the trace element chemistry was difficult. Therefore, a method for the determination of concentrations for a set of elements (Fe, Mn, Co, Ni, Cu, Zn, Cd, Mo, Pb, Ag, Sn, U, V, Y and REE) in the collected fluids was used by applying a separation procedure that adjusts the fluid sample pH to ~6 and applying a single preconcentration step (Sohrin et al., 2008; Minami et al., 2015). The elements were separated from ~2 mL of fluid sample using a column filled with the NOBIAS Chelate-PA1 resin (with ethylenediaminetriacetic acid and iminodiacetic acid

functional groups; Hitachi High-Technologies) and collected for concentration measurement with HR-ICP-MS. The procedure starts with preparation of a buffer with pH~9 by mixing 30 g of acetic acid, 70 g of 18.2 MΩ water, and 50 g of 20% $NH_3$ (Minami et al., 2015), which was used to adjust the samples to pH~6 prior to column purification. Then, the columns were loaded with 0.5 mL of clean NOBIAS Chelate-PA1 resin. The resin was rinsed with 30 mL 18.2 MΩ water, 0.5 mL 3 *M* $HNO_3$, and 10 mL 18.2 MΩ water. Before the sample load the resin was conditioned with 1 mL 2.5% $HNO_3$ + 120 µL buffer at final pH~6. The sample matrix was eluted with 10 mL 18.2 MΩ water. Trace elements were eluted with 23 mL 3 *M* $HNO_3$. At the end the resin was rinsed with 20 mL 18.2 MΩ water and the columns stored for further separation procedures.

The solutions with eluted trace elements were evaporated to dryness and re-dissolved in 2 mL ~0.28 *M* $HNO_3$ for HR-ICP-MS measurements. Concentrations of trace elements in these solutions were measured with a HR-ICP-MS Element XR (ThermoFisher Scientific) at the PSO. Indium was used as an internal standard for correcting drift of the signal and concentrations were calibrated using external calibration standards. A referenced seawater standard (CASS-4; National Research Council, Canada) and two blanks were also processed following the above protocol and analyzed with the same HR-ICP-MS instrument.

*4.4.4. Boron*

Boron concentrations in the fluid samples were determined following the analytical procedure of Cotten et al. (1995) at the PSO. Boron was measured by Inductively Coupled Plasma-Atomic Emission Spectrometry (ICP-AES) using a Horiba Jobin Yvon® Ultima 2 spectrometer. Calibrations were made using the international standard CASS-6 (National Research Council Canada). The standard deviation on the standard was ≤5%.

*4.5. Carbon and O isotope analyses*

*4.5.1. Carbon and O isotope analyses of the spires*

Carbon and oxygen stable isotope compositions of the spire samples were analyzed using an isotope ratio mass spectrometer (IsoPrime, GV Instruments Ldt.) with an automated carbonate reaction system (Multiprep). The $\delta^{13}C$ and $\delta^{18}O$ values are reported with respect to the Vienna Pee Dee Belemnite (VPDB) standard. Analytical errors (95% probability) were estimated to be

within 0.1‰ for both oxygen and carbon, based on repeated measurements of authentic (NBS-19; $\delta^{13}C$ = +1.95‰ and $\delta^{18}O$ = -2.20‰) and laboratory working standards.

*4.5.2. Carbon and O isotope analyses of the fluids*

Fluid samples for C and O isotopic analysis were collected in 12 mL glass vials after filtering (0.2 μm pore-size filters, ADVANTEC). The vials were filled with fluid, sealed with a rubber stopper and an aluminum cap for preventing gas leakage.

The $\delta^{13}C$ of dissolved inorganic carbon (hereafter notated as $\delta^{13}C_{DIC}$) and $\delta^{18}O_{H2O}$ in the sampled fluids were measured with Finnigan MAT Delta Plus stable isotope ratio mass spectrometer accompanied by a Gas Bench. The $CO_2$ was separated by gas chromatography and introduced into the mass spectrometer. For analyzing $\delta^{13}C_{DIC}$ and $\delta^{18}O_{H2O}$, 0.3~0.6 mL of fluid sample were added to one drop of $H_3PO_4$ (~0.02 mL) in 4.5 mL glass vial, filled under 1 atm He and kept at 25.0°C for three days to gain isotopic equilibrium. $\delta^{13}C_{DIC}$ and $\delta^{18}O_{H2O}$ values were calculated with respect to the Vienna Pee Dee Belemnite (VPDB) and VSMOW standards, respectively. Analytical precision of the laboratory standard (HRS-dc) was <0.2‰ (2σ; Hori et al. 2009). The reported $\delta^{13}C_{DIC}$ values were calculated from the measured $\delta^{13}C_{DIC}$ values by taking into account the amount of the remaining aqueous $CO_2$. We used the isotopic equilibrium constant for gaseous and aqueous $CO_2$ of Zhang et al. (1995).

*4.6. Iron-Zn-isotope analyses*

*4.6.1. Iron-Zn-isotope separation from the spire samples*

Polypropylene columns (Kimble Chase) were filled with 2 mL AG MP-1M resin (100-200 mesh; chloride form) for Fe-Zn-isotope separation in two purification steps. In the first purification step, the resin was cleaned with 8 mL 3 *M* $HNO_3$ and 15 mL 18.2 MΩ water, and conditioned with 4 mL 6 *M* HCl before sample load. An aliquot from the 6 *M* HCl archive solution of the spire samples was collected for column load for Fe-Zn-isotope separation. Iron (along with Cu) was eluted with 2.5 mL 6 *M* HCl, 10 mL 2 *M* HCl and 4 mL 0.24 *M* HCl in 30 mL PTFE vials. The solutions were evaporated on hot (90°C) plate to dryness, re-dissolved in 3 mL 6 *M* HCl and stored in 4 mL HDPE tubes for further Fe from Cu isotope separation. Zinc was eluted from the same columns with 18 mL 0.012 *M* HCl in 23 mL PTFE vials. The solutions

were evaporated on hot (90°C) plate to dryness, re-dissolved in ~0.28 *M* $HNO_3$ and transferred in HDPE tubes for MC-ICP-MS analysis.

In the second purification step, the same columns (with 2 mL AG MP-1M resin) were used for separation of Fe from Cu isotopes. The resin was cleaned with 8 mL 3 *M* $HNO_3$ and 15 mL 18.2 MΩ water, and conditioned with 4 mL 6 *M* HCl before sample load. After the sample load (in 3 mL 6 *M* HCl) the matrix was eluted with 2 mL 6 *M* HCl. Copper was eluted with 50 mL 6 *M* HCl in 30 mL PTFE vials and archived in 50 mL centrifuge tubes. From the same columns, Fe was eluted with 12.5 mL 0.24 *M* HCl in 30 mL PTFE vials, evaporated on hot (90°C) plate to dryness, re-dissolved in ~0.28 *M* $HNO_3$ and transferred in tubes for MC-ICP-MS analysis.

*4.6.2. Iron-Zn-isotope separation from the fluid samples*

Fluid samples for Fe-Zn-isotope analysis were selected on the basis of their Fe and Zn concentrations measured by HR-ICP-MS. The samples with low Fe and Zn concentrations (<10 ppb) were not processed for isotope separation and were not analyzed for isotopic compositions.

Aliquots from the fluid samples were taken in PTFE vials and adjusted to pH~6 with the pH~6 buffer (see above). The samples were first purified from the saline matrix and preconcentrated using the NOBIAS Chelate-PA1 resin following the protocol described above. Preconcentrated samples were then processed through columns filled with AG MP-1M resin following the same procedure described above for the spire samples for separation of the isotopes of Fe and Zn.

*4.6.3. Iron-Zn isotope measurements*

Iron and Zn isotopes in spire and fluid samples were measured on a MC-ICP-MS Neptune (ThermoFisher Scientific) at the PSO. Zinc isotope composition was analyzed in low resolution mode using a cyclonic spray chamber as the introduction system. The instrumental mass bias for Zn isotopes was corrected by addition of Cu NIST SRM-3114 standard to samples (Marechal et al., 1999). $^{66}Zn/^{64}Zn$ ratios are reported according to the conventional delta notation (equation 1) using Zn NIST SRM-683 as reference standard for Zn isotope ratio:

$$\delta^{66/64}Zn = [(^{66}Zn/^{64}Zn)_{sample}/(^{66}Zn/^{64}Zn)_{SRM683} - 1] \times 1000 \quad (1)$$

All data from the literature used for comparison in this study were recalculated against the NIST SRM-683 standard.

Iron isotope compositions were measured in high resolution mode and samples were introduced in the plasma with a cyclonic spray chamber. Nickel addition to the samples was used for correcting the instrumental fractionation during the analysis. $^{56}Fe/^{54}Fe$ ratios are reported relative to IRMM-14 according to the conventional delta notation (equation 2) used for stable isotope systematics:

$$\delta^{56/54}Fe = [(^{56}Fe/^{54}Fe)_{sample}/(^{56}Fe/^{54}Fe)_{IRMM\text{-}14} - 1] \times 1000 \quad (2)$$

All data from the literature used for comparison in this study were recalculated against the IRMM-14 standard.

A standard-sample-bracketing scheme was employed for the two isotope system (Fe, Zn) measurements and the USGS Certified Reference Material BHVO-2 was processed through the columns and analyzed along with the samples following the same protocols for comparison with the published values. The typical two-standard deviation on bracketing standards was 0.07‰ for Zn isotope values and 0.07‰ for Fe isotope values.

*4.7. Uranium-Th age dating of the spires*

The chemical procedure for U-Th age dating of carbonate spires followed that described in Bayon et al. (2015). About 75 mg of powdered sample were put in pre-cleaned PTFE vials together with a mixed $^{233}U$-$^{229}Th$ spike, and digested on hotplate with 7.5 *M* $HNO_3$. After evaporation, each sample was taken up in diluted $HNO_3$ prior to addition of ultrapure Fe solution and ammonia to induce Fe-oxide co-precipitation. The resulting Fe-oxides were centrifuged, rinsed in ultrapure water, and further dissolved in 7.5 *M* $HNO_3$. Finally, U and Th were separated using conventional anion exchange techniques. Uranium and Th concentrations and isotope ratios were measured with a MC-ICP-MS Neptune (ThermoFisher Scientific) at the PSO, using a standard-bracketing measurement protocol with IRMM-184 (U) and IRMM-036 (Th) reference solutions, respectively. U-Th carbonate age calculation was performed by the isochron method using the Isoplot/Ex program (version 4.15; Ludwig, 2011) in order to correct measured ratios

from detrital contamination. The mean isochron age was determined using theoretical end-member at the secular equilibrium (activity ratios = 1.0 ± 0.5).

*4.8. Strontium isotope analysis*

About 20 mg powdered spire samples were dissolved in 3 *M* $HNO_3$, prior to separation using Sr resin (Eichrom). Strontium isotopic ratios were determined by MC-ICP-MS Neptune (ThermoFisher Scientific) at the PSO. Measured $^{87}Sr/^{86}Sr$ ratios were normalized to NIST SRM-987 standard solutions. Repeated Sr isotopic analyses of NIST SRM-987 solutions were associated with an uncertainty of 0.000016 (2SD), taken as the external reproducibility of measured $^{87}Sr/^{86}Sr$ ratios. The analysis of a solution of BHVO-2 certified reference material (0.703470 ± 0.000009) agreed well with the recommended value (0.703481 ± 0.000020) of Weis et al. (2005).

The Sr isotopic composition of the fluid samples was determined following a procedure reported by Yoshimura et al. (2018) and Araoka and Yoshimura (2019). We used an offline method for the purification of Sr with ion chromatograph (IC) coupled to an automated fraction collector prior to stable isotope measurements. Samples were introduced into IC on a Metrohm 930 Compact IC Flex (Metrohm AG) instrument coupled to an Agilent 1260 Infinity II Bio-Inert analytical-scale FC system (Agilent Technologies). Then, they were loaded in 0.8 mM ultrapure $HNO_3$ acid (Tamapure AA-100, Tama Chemicals) and passed through a Metrohm Metrosep C6-260/4.0 column at a flow rate of 0.9 mL/min. The purified samples were pooled in 7 mL PTFE vials, then dried out. The dried residue was dissolved in 0.3 *M* ultrapure $HNO_3$ for isotope analysis. We also conducted the separation procedure in a class-1000 clean bench, to avoid contamination.

Strontium isotope ratios were measured by MC-ICP-MS Neptune Plus (ThermoFisher Scientific) at the GSJ, AIST. Instrumental mass fractionation was calibrated by $^{88}Sr/^{86}Sr$ ratio of 8.3752, followed by a standard-sample bracketing method using NIST SRM-987. The reproducibility of multiple measurements of purified Sr solution from IAPSO seawater standard by this IC-FC system during each analytical session: 0.70917 ± 0.00003 (2SD, n = 11) (Araoka and Yoshimura, 2019), which agrees well with the reported values of 0.709169 ± 0.000029 (2SD, n = 5) (Liu et al., 2012).

*4.9. Calcium isotope analysis*

For Ca isotope analyses ~20 mg of the powdered samples from the Lake Asal spire were dissolved in 2.25 *M* $HNO_3$ at room temperature. All chemical preparations were done in a laminar flow bench within clean lab facilities using acids purified by a 2-step Teflon cascade still. After no remaining residues could be observed, aliquots of 1500 ng Ca equivalent of these solutions as well as of hydrothermal fluid and of lake water were mixed with a $^{43}Ca/^{48}Ca$ double spike and evaporated. The samples were treated with a mixture of 0.75 mL 8 *M* $HNO_3$ and 0.25 mL $H_2O_2$ for at least 12 h at 80°C to disintegrate potentially Ca purification hampering organics. After evaporation to dryness at 80ºC and re-suspension in 2.2 *M* $HNO_3$ at room temperature, procedures for Ca extraction with MCI-Gel, isotope measurement with a Finnigan Triton Thermal Ionisation Mass Spectrometer (TIMS), and data reduction were followed as described by Heuser et al. (2002) and Böhm et al. (2006).

As matrix matching whole procedure repeatability and blank sensitivity test aliquots of two samples (Site 3 vent and Lake Abhé site 14) were also processed on half Ca amount (750 ng equivalent). The results for these additional samples showed within uncertainties identical mean values when compared to their double-sized routine equivalents (differences of mean values 0.03 and 0.04‰, respectively). With keeping identical, or very similar uncertainties (95% confidence level) this small sample duplicate approach implies adequate repeatability, method robustness and no significant blank contribution (typical below 50 ng Ca for this method and facility).

Each sample run through the clean-lab procedures described above was measured 3 to 7 times (indicated as "n") and each of these measurements was performed on its own filament. The accuracy of the reported mean results is supported by distributing the measurements on at least two of seven different and independent TIMS sessions involved in this study. These sessions were individually normalized on the session specific mean of NIST SRM-915a measurement sets (n=3), which were operated similarly to the samples by running each measurement on own and originally loaded filament from one source solution. The NIST SRM-915a repeatability was ± 0.2‰ (95% confidence level, $n_{sessions}$ = 7), typical for this method and measurement facility. Based on increased "n" values all samples analyzed during the course of the study reached repeatability better than this limit.

Isotope data are reported as $\delta^{44/40}Ca$ (‰) relative to the NIST standard SRM-915a, where:

$$\delta^{44/40}Ca = [(^{44}Ca/^{40}Ca)_{sample}/(^{44}Ca/^{40}Ca)_{SRM\text{-}915a} - 1] \times 1000 \quad (3)$$

All Ca isotope data from the literature used for comparison in this work was converted relative to the NIST standard SRM-915a.

*4.10. Sulfur isotope analysis of the fluids*

Sulfur isotope composition of $SO_4^{2-}$ in the fluids was analyzed after $SO_4^{2-}$ recovery as $BaSO_4$ precipitated upon adding 0.5 *M* BaCl solution in the samples. Sulfur isotope ratio of the precipitate was measured using a continuous-flow mass-spectrometer with an elemental analyzer IsoPrime EA (GV Instruments). Sulfur isotope values are reported using the common notation, $\delta^{34}S$, per mil deviation relative to the international standard Canyon Diablo Troilite (CDT).

**5. Results**

*5.1. Mineralogy of the spires*

The spire from Lake Asal (LAs) is composed of low-Mg calcite and aragonite (Table 2). The different layers of the spire wall (Fig. 3 A) are composed of different proportions of these two minerals. In the central zone (LAs-3) low-Mg calcite dominates over aragonite, whereas in the outer layers (LAs-2 and -1) aragonite content is close to that of low-Mg calcite (Table 2). The low-Mg calcite crystals in the central zone (LAs-3) are concentrically zoned (Fig. 4 A,B). At the transition between the low-Mg calcite dominated central zone (LAs-3) and the next layer where low-Mg calcite and aragonite are in comparable proportions (LAs-2) the low-Mg calcite crystals are overgrown by needle-like aragonite crystals, which in turn are coated by low-Mg calcite (Fig. 4 C,D). The outer layers (LAs-2 and -1) of the spire are composed of botryoids of needle-like aragonite overgrown by low-Mg calcite (Fig. 4 E,F,G,H).

The spire from Lake Abhé (LAb) is composed of low-Mg calcite and high-Mg calcite (Table 2). Different proportions of these calcite varieties compose the layers of the spire wall (Fig. 3 B). In general, most of the internal layers (around the central zone) are low-Mg calcite dominated, whereas the external layers are high-Mg calcite dominated (Table 2). The high-Mg calcite dominated layers have botryoidal surface composed of fine radial high-Mg calcite crystals (Fig. 5 A,B). The low-Mg calcite dominated layers are composed of skeletal low-Mg calcite crystals (Fig. 5 C,D).

Salt from the salt plain of Lake Asal is composed of halite and traces of gypsum (Table 2).

*5.2. Chemical composition of the spires*

Trace element concentrations in the carbonate spire from Lake Asal (LAs) increase from the innermost (central) zone towards the outermost zone (layer) (Table 3). The total amount of the REE (ΣREE) also increases from the innermost to the outermost zone (Table 3). The Post-Archean Australian Shale-normalized (PAAS-normalized) REE distribution patterns of the spire layers are similar to that of the local basalt (LAs-basalt): they show no Ce anomaly (Ce/Ce* ~1), positive Eu anomaly (Eu/Eu*>1) and depletion in the light REE in respect to the heavy REE ($La_{PAASN}/Lu_{PAASN}$<1) (Table 3; Fig. 6 A). The positive Eu anomaly decreases from the innermost to the outermost zone (Table 3).

Most trace element (Si, Mg, P, Mn, Sr, Ba, Li, Ni, V, Pb, Cr, Th, Y and REE) concentrations in the carbonate spire from Lake Abhé (LAb) show a clear correlation with spire layer mineralogy: higher concentrations are observed in the high-Mg calcite layers (LAb-3, -5, -6, -7, -8) compared to the low-Mg calcite layers (LAb-1, -2, -4) (Table 3). Low-Mg calcite layers have higher both positive Ce (Ce/Ce*>1) and positive Eu (Eu/Eu*>1) anomalies, and are more depleted in the light REE relative to the heavy REE than the high-Mg calcite layers (Table 3; Fig. 6 B). Aluminum, Ti, Fe, Rb, Mo, Ga, U, Cu, Co and Zn do not demonstrate clear dependence on the mineralogy of the spire layers (Table 3).

The major element concentrations in the studied Asal Rift basalt (Table 4) are similar to those previously reported for the local basalts (Barrat et al., 1993). Using the major element composition (Table 4) and bulk mineralogy (Table 2) of the salt from the Lake Asal salt plain we

estimated that in addition to the halite (NaCl) and gypsum ($CaSO_4 \cdot 2H_2O$) the salt precipitated at the Lake Asal bottom contains also $MgCl_2$ and KCl (Table 4).

*5.3. Chemical composition of the fluids*

Previous studies suggested genetic relations among the seawater in the Ghoubbet-al-Kharab, hydrothermal fluids in the Asal Rift and Lake Asal water (Bäcker et al., 1973; Gasse and Fontes, 1989; Sanjuan et al., 1990; D'Amore et al., 1998), therefore, we will compare the elemental concentrations in these three fluid types. Relationship between the lake water and local hydrothermal fluids was inferred for Lake Abhé (Dekov et al., 2014) and thus, the chemistry of these two fluids are also compared.

Sodium, $SO_4$, K and Mg have the lowest concentrations in the hydrothermal fluids, then in the seawater and the highest concentrations in the Lake Asal water (Table 5). Their contents show a similar increase from the hydrothermal fluid to Lake Abhé water (Table 5). Chlorine content is the lowest in the seawater and the highest in the Lake Asal water (hydrothermal fluid being in between) and similar concentration trend is found in the Lake Abhé system as well: lower in the hydrothermal fluid and higher in the lake water (Table 5). Calcium shows another type of concentration gradation: lowest in the seawater and highest in the Lake Asal hydrothermal fluid (Lake Asal water being in between) (lower in the lake water and higher in the hydrothermal fluid at the Lake Abhé) (Table 5). A similar increase (low in the Lake Asal water and high in the hydrothermal fluid) can be observed for Si and $NO_3$ conventrations, whereas the concentration of Br demonstrates an opposite trend (low in the hydrothermal fluid and high in the Lake Asal water) (Table 5).

Iron, Mo, V, Ag, Cd and La have higher concentrations in the hydrothermal fluids jetting around Lake Asal than in the Lake Asal water (Table 5). Manganese, Cu, Zn, Co, U, Sn, Pb, Li, Sr, Y, Pr and Nd show higher contents in the Lake Asal water than in the hydrothermal fluids (Table 5). Particularly high enrichment in the lake water relative to the hydrothermal fluid show Zn, U and Mn. Lithium is very high in both fluids. Nickel, Ce and Sm are in relatively similar amounts in both Lake Asal water and hydrothermal fluids (Table 5).

Generally speaking, Lake Abhé hydrothermal fluid has higher Li and Sr content, whereas Lake Abhé water has higher Fe, Mn, Cu, Ni, Co, Pb, Y and REE content (Table 5). Notably,

Lake Abhé water is strongly enriched in Fe, Ni and REE when compared to the hydrothermal fluid (Table 5). Both the Lake Abhé water and hydrothermal fluid contain similar amounts of Zn and Sn.

Vertical distributions of pH, T, alkalinity, and concentrations of major and trace elements across the Lake Asal water body were investigated in detail along one vertical profile, C1 (Fig. 7; Tables 1, 5). As a reference sample we have considered the hydrothermal fluid (3-nov) jetting at Site 3 and emptying in the lake. According to the vertical distributions of these physical and chemical parameters the lake water body can be divided in bottom, intermediate and surface zones at this site (Fig. 7). The bottom water (~15-23 m depth) has low pH (6.5-6.6), elevated T (27-28°C), high alkalinity, low concentrations of $Cl^-$, $SO_4^{2-}$, V, Ni and Co, and high concentrations of $Br^-$, $NO_3^-$, Zn, Cu, Mn, Sn, Ag, Pb, U, Mo and Si (Fig. 7). The prominent features of the intermediate water (~10 m depth) are an elevated pH (~6.9), temperature (~25°C) lower than that in the other two water zones, and the lowest Mn and highest Mo contents (Fig. 7). The surface water (0-5 m depth) has high T (~27°C), low alkalinity, the highest concentrations of $Cl^-$, $SO_4^{2-}$, Fe, Mn, V, Ni and Co, and the lowest concentrations of Zn, Sn, Ag, Mo and Si (Fig. 7).

The REE concentrations in the Lake Asal water and hydrothermal fluids are very low: medium (Eu - Dy) and heavy (Ho - Lu) REE are below the limits of detection (Table 5). The REE concentrations are also very low in the Lake Abhé hydrothermal fluids, but in the Lake Abhé water they showed measurable contents (Table 5). Therefore, at the fragmentary PAAS-normalized REE distribution patterns of the Lake Asal waters we can only see the weak negative Ce anomaly ($Ce/Ce^* <1$) and a hint for no fractionation between the light and heavy REE ($La_{PAASN}/Lu_{PAASN}$~1) (Table 5; Fig. 6 C). The PAAS-normalized REE distribution pattern of the Lake Abhé water shows a well-pronounced positive Ce anomaly ($Ce/Ce^* >1$), a weak positive Eu anomaly ($Eu/Eu^*>1$) and depletion in the light REE in respect to the heavy REE ($La_{PAASN}/Lu_{PAASN}<1$) (Table 5; Fig. 6 C).

*5.4. Isotope composition of the spires*

U-Th age dating of the studied spires shows that their most internal (central) zones are the oldest zones and the age of the different zones (layers) decreases outwards (Table 6).

The stable isotope composition of the different layers of Lake Asal spire (LAs) is a linear function of the age of the layers: $\delta^{13}C$, $\delta^{18}O$, $\delta^{44}Ca$, $\delta^{56}Fe$ and $\delta^{66}Zn$ become heavier with decreasing age (Table 6). Strontium isotope ratio ($^{87}Sr/^{86}Sr$) decreases (becomes less radiogenic) in the same direction (Table 6). Measured $^{87}Sr/^{86}Sr$ ratio of the local basalts (Table 6) is similar to that measured in previous works (Barberi et al., 1980).

Carbon, O, Fe and Sr isotope compositions of the Lake Abhé spire (LAb) show correlations with the mineralogy of the spire layers. $\delta^{13}C$ and $\delta^{18}O$ are heavier, $\delta^{56}Fe$ is lighter, and $^{87}Sr/^{86}Sr$ is more radiogenic in the high-Mg calcite layers than in the low-Mg calcite layers (Table 6).

*5.5. Isotope composition of the fluids*

The hydrothermal fluids jetting around Lake Asal (sample 3-nov) have light C isotope composition ($\delta^{13}C$ = -2.73‰) close to that of the local seawater ($\delta^{13}C$ = -2.89‰) (Table 7). In contrast, Lake Asal water has heavy C isotope composition ($\delta^{13}C$ >6‰) that varies across the lake water body (Table 7; Fig. 7). A similar trend is observable in Lake Abhé: light $\delta^{13}C$ in the hydrothermal fluids and heavier (although not reaching positive $\delta^{13}C$ values) in the lake water (Table 7).

Oxygen isotope composition of the seawater collected in Ghoubbet-al-Kharab ($\delta^{18}O$ = 0.85‰; Table 7) is within the $\delta^{18}O$ range measured in the surface seawater in the adjacent Gulf of Aden ($\delta^{18}O$ = 0.5 – 1.0‰; Schmidt et al., 1999). The hydrothermal fluids discharging around Lake Asal have O isotope composition heavier than that of the neighbor seawater ($\delta^{18}O_{3\text{-nov}}$ = 2.79‰), but lighter than the O isotope composition of the Lake Asal water ($\delta^{18}O$ > 4‰) (Table 7). Water close to the Lake Asal bottom has $\delta^{18}O$ lighter than that of the intermediate and surface waters (Fig. 7). The negative $\delta^{18}O$ values of the hydrothermal fluids jetting around Lake Abhé (Table 7) are similar to those of the groundwater from the lower Awash River (Bretzler et al., 2011) that feeds the lake. The Lake Abhé water has positive $\delta^{18}O$ values (Table 7).

Sulfur isotope composition of sulfate in the Lake Asal hydrothermal fluids (Table 7) is between those of the terrestrial mantle (-0.91±0.50‰; Labidi et al., 2012) and seawater (20.97‰; Paris et al., 2013). The seawater from the Ghoubbet-al-Kharab has $\delta^{34}S$ very close to that of the mean seawater value (Table 7). Sulfur isotope composition (sulfate) of the Lake Asal water varies

between 19.0 and 19.6‰ with the lightest values at the lake bottom and heaviest at the lake surface (Fig. 7; Table 7).

$\delta^{44}$Ca of the mean seawater standard (IAPSO) showed a value (1.85 ± 0.09 ‰, SE, n=9; Table 7) in accord with published average seawater value (1.92‰; Fantle and Tipper, 2014). Calcium isotope composition of the Lake Asal hydrothermal fluids (0.92‰; Table 7) is within the range of the Ca isotope composition of the seafloor hydrothermal fluids [0.72 – 1.92‰; Amini et al. (2008), Scheuermann et al. (2018)] and close to that of the seafloor end-member hydrothermal fluid [0.88‰; Amini et al. (2008), Scheuermann et al. (2018)]. Hydrothermal fluids from Lake Abhé tend to even lighter Ca isotope composition (0.74-0.93‰; Table 7) similar to the one we measured earlier [0.90‰; Dekov et al. (2014)]. Calcium isotope composition of the Lake Asal water (1.22-1.64‰; Table 7) is significantly heavier than that of the local hydrothermal fluids and approaches the seawater isotope composition. The heaviest isotope values are observed close to the lake floor whereas the lightest values are below the lake surface (Fig. 7). Lake Abhé water has heavier Ca isotope composition (2.84‰) than the Lake Asal (Table 7) and slightly lighter than the previously measured [3.45‰; Dekov et al. (2014)]. However, it is distinctly heavier than the Ca isotope composition of river water (0.2 – 1.7‰; Fantle and Tipper, 2014).

Zinc isotope composition of the Lake Asal water is mostly negative ranging from -0.15 to 0.02‰ ($\delta^{66}$Zn) (Table 7). The lightest $\delta^{66}$Zn values are observed close to the lake bottom and $\delta^{66}$Zn increases towards the lake surface (Fig. 7). The only hydrothermal fluid in which we were able to measure the Zn isotope composition was from a hot spring at the Lake Abhé shore which had $\delta^{66}$Zn = 0.26‰ (Table 7). $\delta^{66}$Zn of the Lake Asal water (Table 7) is at the lighter end of the $\delta^{66}$Zn range of both the seafloor hydrothermal fluids (-0.12 - +1.21‰; John et al., 2008) and seafloor sulfides (-0.21 - +1.05‰; John et al., 2008).

Lake Asal hydrothermal fluid has $^{87}Sr/^{86}Sr$ ratio similar to that of the Asal Rift basalt (Tables 6, 7). Lake Asal water has more radiogenic Sr isotope composition than the hydrothermal fluid, but it is less radiogenic than the seawater (Table 7). $^{87}Sr/^{86}Sr$ ratio is the lowest close to the lake bottom and slightly increases upward to the lake surface (Fig. 7). Hydrothermal fluids jetting at the Lake Abhé shore have Sr isotope composition (Table 7) close to that of the local basalts (Dama Ale volcano; Barberi et al., 1980). Strontium isotope composition of the Lake Abhé water (Table 7) is close to that of the Awash River (Bretzler et al., 2011), which feeds the lake.

## 6. Discussion

### *6.1. Lake Asal: a lake fed by seafloor-type hydrothermal fluids*

A lake located in tropical arid zone with scarce rainfall and with apparent lack of riverine water supply from distant wet zones will always provoke the question about its water source. The hypothesis that Lake Asal [a tropical-arid lake with no river supply; Gasse and Fontes (1989)] receives its water from the ocean (via Ghoubbet-al-Kharab) through fissures and faults was suggested long ago (Bäcker et al., 1973) and investigated to some extent recently (Boschetti et al., 2018). In a study of the Holocene (~10 – 0 kyr B.P.) palaeohydrology of the lake, Gasse and Fontes (1989) suggested that the strong water level fluctuations (from +160 to -150 m) in the lake have been controlled by both climate and water source changes. They hypothesized that the fresh groundwater from the Awash River system and seawater from the neighbor ocean have been the major sources of water to the lake and either of them had dominated over different stages of the lake history: e.g., fresh groundwater had dominated between ~8.6 and 6 kyr B.P., while seawater has dominated between ~5 and 0 kyr B.P.. Their conclusions relied on indirect geological evidence and climatic mass-balance calculations. Although Gasse and Fontes (1989) inferred the seawater was one of the major components of the Lake Asal water, their work implied that this component was comparable with the fresh groundwater input. The seawater supply was regarded as an infiltration (seemingly in physical sense) through the rocks between the ocean and the lake without any water-rock interaction and related consequences for the lake water chemistry.

Although we cannot completely rule out fresh groundwater supply to the Lake Asal (there is no riverine input and the rainfall is scarce) our data show that this possible water component is negligible in Recent time. The strong evaporation of a lake water body dominated by a fresh water component would result in a saline, but basic lake (pH>7), similar to what is observed for Lake Abhé (Table 1). Lake Asal, which is also subjected to strong evaporation, is hypersaline and slightly acidic (pH<7; Table 1), suggesting that a fresh groundwater supply to this lake is either insignificant or lacking altogether.

Later studies from 1990s inferred that the hot spring fluids jetting in the Asal Rift were a result of seawater-basalt interaction (Sanjuan et al., 1990). Investigations of these fluids in geothermal wells showed that deep in the crust the fluids were hot (260-359°C), enriched in Fe, Zn, Pb, Si, Ca and Li, and depleted in Mg and $SO_4$ (D'Amore et al., 1998). Although they were inferred to

originate from seawater after interaction with hot basement rocks these hot mineralized fluids were considered disconnected from the Lake Asal water body (D'Amore et al., 1998).

Based on the ideas from previous works (Bäcker et al., 1973; Gasse and Fontes, 1989; Sanjuan et al., 1990; D'Amore et al., 1998) and our data on the chemistry (including isotope composition) of the lake water and hydrothermal fluids jetting around the lake we hypothesize that the Lake Asal is essentially fed by hydrothermal fluids of seafloor-type: seawater modified during its passage through the hot basement rocks.

*6.1.1. Major element evidence for seafloor-type hydrothermal recharge of Lake Asal*

Seawater was recognized as a mother fluid of the hydrothermal fluids jetting into the Asal Rift and their nature appears to be similar to that of the seafloor hydrothermal fluids. However, this begs the question: is Lake Asal fed by hydrothermal fluids (seafloor type; i.e., born upon high-temperature seawater-rock interaction) or is it filled gradually by seawater percolating through rocks (without any high-temperature seawater-rock interaction)? The major element composition of the Lake Asal water and hydrothermal fluids can provide constraints on these two possibilities.

A fundamental feature of the seawater chemistry is that the major ions are present in relatively constant ratios. These constant ratios are not maintained in the seafloor hydrothermal fluids because of the gains and losses of elements during sub-seafloor seawater-rock interactions. Chlorine is a conservative element through these interactions. According to the previous works (Gasse and Fontes, 1989; Sanjuan et al., 1990) and our physical-chemical parameters measurements (Table 1) the Asal Rift hydrothermal fluids and Lake Asal water are seawater-based. The element/Cl ratios in these fluids will be indicators for gains or losses of elements relative to the starting fluid (seawater) if the starting fluid has interacted with the rocks. Na/Cl of the Lake Asal hydrothermal fluid (0.31) and, particularly, that of the Lake Asal water (0.22-0.24) are lower than that of the seawater (0.53-0.56) (Table 8). This means that the seawater has lost Na during its reaction with the basement rocks. It is well-known that Na can be lost from the hydrothermal fluids due to Na for Ca replacement reactions in plagioclase, known as albitization (German and Von Damm, 2003). Potassium is obviously also involved in similar type of replacement reaction (e.g., palagonitization) showing depletion in the hydrothermal fluids and even stronger depletion in the Lake Asal water relative to the seawater (Table 8).

Although Lake Abhé is not seawater-fed we can use the same type of element/Cl ratios for estimation of the enrichment or depletion of the major elements in the studied fluids. Sodium is enriched in the lake water relative to the hydrothermal fluids, whereas K shows similar ratios in both fluids (Table 8). This may mean that the "excess" of Na in the lake water is a result of Na riverine input likely surpassing the Na deficiency of the hydrothermal fluids. The similar K/Cl ratios of the lake water and hydrothermal fluids imply for a balance between the excess and deficiency of K in these two fluids.

Magnesium and $SO_4^{2-}$ are quantitatively removed from the seawater during its interaction with the basement rocks at the mid-ocean ridges and the end-member seafloor hydrothermal fluids at this setting do not contain them (German and Von Damm, 2003). Although not reaching zero concentrations, these two species are depleted in the Lake Asal hydrothermal fluids (Table 8). The Lake Asal waters are also depleted in Mg and $SO_4^{2-}$ relative to the seawater, but they are slightly enriched in these species in respect to the hydrothermal fluids (Table 8).

Sulfate is enriched in the Lake Abhé waters relative to the hydrothermal fluid which suggests excess riverine supply of $SO_4^{2-}$ to the lake over the hydrothermal $SO_4^{2-}$ input.

The identical Br/Cl ratio in both the Lake Asal hydrothermal fluids and lake water, and its similarity to that of the seawater (Table 8) suggests that Br behaves conservatively along the entire passage of the seawater through the hot basement rocks to the Lake Asal.

Calcium enrichment in the Lake Asal hydrothermal fluids relative to the seawater (Table 8) is similar to that of the seafloor hydrothermal fluids. Following the analogy with the seafloor hydrothermal circulation (German and Von Damm, 2003) we may infer that although part of the seawater Ca might have been immobilized as $CaSO_4$ (anhydrite) in the crust, the dissolution of Ca-plagioclases in the Asal Rift basement rocks by hydrothermal fluids has provided a net surplus of Ca in the vent fluids. However, the Ca/Cl ratio in the lake water decreases more than 10 times relative to that of the hydrothermal fluids (Table 8). If the hydrothermal fluids are the major source of water to Lake Asal then the drop in the Ca concentration in the lake water (Tables 5, 8) suggests a removal process of Ca from the water. Even more dramatic depletion in Ca of the Lake Abhé waters relative to the Lake Abhé hydrothermal fluids (Tables 5, 8) testifies to a more efficient mechanism of Ca removal from the lake water.

*6.1.2. REE evidence for seawater-based fluid recharge of the Lake Asal*

The PAAS-normalized REE distribution patterns of the Lake Asal water (Fig. 6 C) give additional evidence that the lake water precursor was a seawater-based fluid. These distribution patterns show negative Ce anomaly (Fig. 6 C) similar to the well-documented negative Ce anomaly of the seawater that is recognized as its common feature (Elderfield and Greaves, 1982; Alibo and Nozaki, 1999; Deng et al., 2017). The Lake Asal water Ce anomaly ($Ce/Ce^* = 0.39$, average of 9 samples, Table 5) is smaller than that of the seawater ($Ce/Ce^* = 0.29$, average of 18 samples along the water column of the Pacific; Deng et al., 2017). A reasonable explanation for this decrease is that the lake water is a fluid evolved from seawater (with pronounced negative Ce anomaly) towards seafloor end-member hydrothermal fluid with no Ce anomaly (Michard et al., 1983; Klinkhammer et al., 1994).

The PAAS-normalized REE distribution pattern of the Lake Abhé water (Fig. 6 C) shows features discussed in a previous study (Dekov et al., 2014). The pronounced positive Ce anomaly and heavy REE enrichment in the lake water was accounted for by stablilization of carbonato- Ce and HREE aqueous complexes at high alkalinity, whereas the weak positive Eu anomaly could likely be a result of hydrothermal fluid discharge close to the sampling site (Dekov et al., 2014).

*6.1.3. Chemistry of the end-member hydrothermal fluid*

We used the hydrothermal fluid from Site 3 (sample 3-nov; Table 1) as a fluid close to the hypothetical end-member hydrothermal fluid for Lake Asal because it has $^{87}Sr/^{86}Sr$ ratio (0.704396, Table 7) close to that of the local basalt (0.704027, Table 6), and also has very low $SO_4/Cl$ and Mg/Cl ratios (Table 8).

By analogy with the seafloor venting fluids (German and Von Damm, 2003), the Lake Asal hydrothermal fluid (e.g., sample 3-nov) can be considered as a mixture of the end-member hydrothermal fluid and Lake Asal water. The theoretical end-member hydrothermal fluid should have $[SO_4^{2-}] = 0$ g/L and chloride concentration ($[Cl^-]$) equal to that of seawater if no subsurface boiling and phase separation occurred. However, the venting fluid at the Lake Asal bottom (e.g., 3-nov at Site 3) cannot be described by mixing of such a theoretical end-member hydrothermal fluid with Lake Asal water (Fig. 8). It lies on the mixing line between the Lake Asal water and a fluid with seawater chlorinity ($[Cl^-] = 19.6$ g/L; Table 5) and $[SO_4^{2-}] = 0.215$ g/L (Fig. 8). We will consider this fluid as actual end-member hydrothermal fluid (Fig. 8), which has not completely lost its original seawater sulfate during seawater/rock interaction. Mixing calculations

show that the fluid venting at the Lake Asal bottom (3-nov) is a mixture of 97% actual end-member hydrothermal fluid and 3% lake water (Fig. 8).

The calculated chemistry of the actual end-member hydrothermal fluid of the Lake Asal (Table 9) implies that the end-member hydrothermal fluid of an "embryonic" ocean seems to be poorer in metals than the seafloor hydrothermal fluids of an open and evolved ocean.

*6.2. Isotope composition of an oceanic "embryo" in arid climate: heavy O, C and Ca, and light Zn*

Our results suggest that the hydrothermal fluids in the Asal Rift that feed Lake Asal are of seafloor type. Hence, these hydrothermal fluids should have stable isotope signatures similar to those of the seafloor hydrothermal fluids. $\delta^{18}O$ of the Lake Asal hydrothermal fluids (2.79‰; Table 7) is heavier than that of the seafloor hydrothermal fluids, which have $\delta^{18}O$ varying between 0 and 2‰ (Shanks, 2001). This heavier $\delta^{18}O$ value may be attributed to a greater exchange of O with the crust during hydrothermal circulation ($\delta^{18}O_{\text{Asal Rift rocks}}$ = +4.6 - +12.2‰; Fouillac et al., 1989) probably due to longer reaction path and low water/rock ratio. Another possible explanation of this isotope difference is a subsurface mixing of the upwelling hydrothermal fluids with presumably $\delta^{18}O$ = 0 - 2‰ with downwelling lake water with $\delta^{18}O$ > 4‰ (Table 7). If the Lake Asal water originates from seawater ($\delta^{18}O$ = 0.85‰; Table 7) modified towards heavier oxygen isotope values ($\delta^{18}O$ up to 2.79‰; Table 7) through seawater/rock interaction, then a further differential removal of the lighter oxygen isotope ($^{16}O$) during evaporation has likely caused the additional shift to heavier $\delta^{18}O$ values (e.g., Rohling, 2013) in the lake water ($\delta^{18}O$ > 4‰, Table 7).

The hydrothermal fluids fill the Lake Asal with light C isotope water ($\delta^{13}C$ = -2.73‰) isotopically similar to the local seawater ($\delta^{13}C$ = -2.89‰) (Table 7). Further, the strong evaporation likely has led to enrichment of the lake water in $^{13}C$ (e.g., Horton et al., 2016) and the lake has progressively evolved towards a heavy C isotope water body ($\delta^{13}C$ > 6‰; Table 7, Fig. 7). This inferred evolution to a heavy C and O isotope lake is recorded in the associated authigenic mineral precipitates, carbonate spires, showing gradually increasing $\delta^{13}C$ and $\delta^{18}O$ through time (Table 6). The $\delta^{13}C$ decrease in the surface water layer (Fig. 7) seems to be a result

of the Suess effect (Keeling, 1979): addition of isotopically lighter anthropogenic $CO_2$ from the atmosphere.

Close similarity of the Ca isotope composition of the Lake Asal hydrothermal fluids (Table 7) to that of the seafloor end-member hydrothermal fluids (Amini et al., 2008; Scheuermann et al., 2018) is an additional argument that the Lake Asal hydrothermal fluids are of seafloor-type. Explanation of how the heavy seawater ($\delta^{44}Ca$ = 1.92‰; Fantle and Tipper, 2014) evolves towards a light seafloor-type hydrothermal fluid [$\delta^{44}Ca_{\text{end-member hydrothermal fluid}}$ = 0.88‰; Amini et al. (2008), Scheuermann et al. (2018)] with a Ca isotope composition close to that of the mid-ocean ridge basalt (0.88‰) can be found elsewhere (Amini et al., 2008; Scheuermann et al., 2018). In the case of an oceanic "embryo" (e.g., Lake Asal) entirely fed by seafloor-type hydrothermal fluids the interesting question is: how has the oceanic "embryo" got Ca isotope composition markedly heavier than that of its potential source fluids (Table 7)? The observed lake water Ca isotope composition suggests isotope fractionation upon/after the hydrothermal fluid discharge. $\delta^{44}Ca$ vertical profile across the lake water body (Fig. 7) shows that the heaviest Ca isotope composition forms close to the lake bottom. The essential chemical reaction in which Ca is involved during the hydrothermal fluid discharge in the lake is the Ca-carbonate spire deposition. This takes place at the lake bottom. Hence, the Ca-carbonate spire formation appears to be responsible for the Ca isotope fractionation. Laboratory experiments showed that the inorganic precipitation of calcite from solution led to Ca isotope fractionation where the calcite had lighter Ca isotope composition than the solution (Tang et al., 2012; AlKhatib and Eisenhauer, 2017a,b). Based on these studies we can infer that the hydrothermal carbonates building spires at the lake bottom preferentially retain the light Ca isotope ($^{40}Ca$) of the hydrothermally derived Ca ($\delta^{44}Ca$ = 0.92‰) thus, leaving a fluid with heavy Ca isotope composition which fills the lake ($\delta^{44}Ca$ > 1.20‰). Calcium isotope composition of the Lake Asal Ca-carbonate spires that shows an increase in $\delta^{44}Ca$ through the time of spire formation (from 0.22‰ to 1.06‰; Table 6) accounts for this isotope fractionation. The oldest central part of the spire has Ca isotope composition (0.22‰) much lower than that of the venting hydrothermal fluid (~0.90‰). The further increase of $\delta^{44}Ca$ (to 1.06‰; Table 6) of the spire layers can be explained with mixing of the hydrothermal fluid with more heavy lake water ($\delta^{44}Ca$ > 1.20‰; Table 7).

The heavy Ca isotope composition of the Lake Abhé ($\delta^{44}Ca$ = 2.84‰; Table 7) cannot be explained by simple mixing of the two major sources of water to it: riverine ($\delta^{44}Ca_{\text{rivers}}$ = 0.2 –

1.7‰; Fantle and Tipper, 2014) and hydrothermal (0.74-0.93‰; Table 7). The heavy Ca isotope composition of the lake water can reasonably be explained with preferential sequestration of the light Ca isotope ($^{40}$Ca) from the fluids by the precipitating Ca-carbonates and residual enrichment of the lake water in the heavy Ca isotope ($^{44}$Ca).

If Lake Asal is fed by seawater-derived hydrothermal fluids, the lake water should have an isotopic composition close to that of modern seafloor hydrothermal fluids if no isotope fractionation occurs within the lake reservoir. The Lake Asal water has mostly negative Zn isotope composition ($\delta^{66}$Zn = -0.15 - +0.02‰; Table 7), which although matching the lighter end of the Zn isotope compositional range of the seafloor hydrothermal fluids ($\delta^{66}$Zn = -0.12 - +1.21‰; John et al., 2008) is still lighter than the average seafloor hydrothermal fluid ($\delta^{66}$Zn = +0.12‰; Little et al., 2014). Even if we assume that the seawater, which fills the lake has not been modified to hydrothermal fluid during its passage through the Asal Rift rocks the positive Zn isotope composition of seawater ($\delta^{66}$Zn = +0.34‰; John et al., 2005) cannot account for the negative $\delta^{66}$Zn of the Lake Asal water. It seems likely that the seafloor-type hydrothermal fluids have been subjected to fractionation upon entering the lake and this fractionation results in a water body with negative $\delta^{66}$Zn.

When the hydrothermal fluids emerge from the lake bottom they discharge part of their chemical load in the form of carbonate spires. The carbonate spires with their positive $\delta^{66}$Zn (0.07 - 0.23‰; Table 6) are potential candidates for fractionating the Zn isotopes.

Previous studies found that Zn adsorbed on calcite (Dong and Wasylenki, 2016) or coprecipitated with calcite (Mavromatis et al., 2019) was isotopically heavier than that in the co-existing fluid. In a high ionic strength fluid the average $\Delta^{66}Zn_{adsorbed\text{-}fluid}$ was 0.73‰ (Dong and Wasylenki, 2016). Dong and Wasylenki (2016) consider this as an equilibrium fractionation between dissolved Zn and calcite-sorbed Zn that is sensitive to aqueous Zn speciation. Their mass balance calculations showed that a pool of isotopically light Zn is complexed with $Cl^-$ in high ionic strength solutions, leading to a heavier pool of Zn adsorbed on the calcite surface.

The Lake Asal system includes (1) seafloor-type hydrothermal fluids, (2) highly saline (high ionic strength) lake water that is a result of hydrothermal fluid accumulation and its evolution as a lake body, and (3) carbonate spires that grow at the lake bottom as a result of the interaction between the first two components. The source fluid (component 1) has presumably positive Zn isotope composition [$\delta^{66}Zn_{average}$ = +0.12‰ (Little et al., 2014); ranging from -0.12 to +1.21‰

(John et al., 2008)], whereas the lake water (component 2) has negative ($\delta^{66}Zn_{average}$ = -0.06‰; Table 7) and the carbonate spires (component 3) have positive ($\delta^{66}Zn_{average}$ = 0.17‰; Table 6) Zn isotope compositions. A reasonable explanation of the observed isotopically light lake water and isotopically heavy carbonate spires is Zn isotope fractionation during carbonate spire formation due to Zn adsorption on carbonates (calcite and aragonite) (e.g., Dong and Wasylenki, 2016).

Overall, unlike an open and evolved modern ocean with $\delta^{13}C$ ranging from -6.56 to +3.10‰ (Cheng et al., 2019), $\delta^{18}O$ ranging from -1.5 to +1.8‰ (Carpenter and Lohmann, 1995) and positive Zn isotope composition ($\delta^{66}Zn$ = +0.34‰; John et al., 2005) the ocean at "embryonic" stage has heavy both C and O isotope composition ($\delta^{13}C$ > 6‰, $\delta^{18}O$ > 4‰; Table 7) and negative Zn isotope composition ($\delta^{66}Zn_{average}$ = -0.06‰). Calcium isotope compositions of both types of ocean are similarly heavy: $\delta^{44}Ca_{open\ evolved\ ocean}$ = 1.92‰ (Fantle and Tipper, 2014), $\delta^{44}Ca_{"embryonic"\ ocean}$ = 1.22-1.64‰ (Table 7).

*6.3. Hydrothermal discharge from the lake bottom and aeolian input to the lake surface*

Although we have not observed and sampled venting fluids from the Lake Asal bottom our data suggests that this lake is fed by hydrothermal fluids of seafloor type. The vertical profile across the Lake Asal water body at Site C1 (Fig. 1 B; Table 1) shows a number of evidence for hydrothermal discharge from the lake bottom close to this site. The lower end of C1 profile (samples C1-1 (23 m) and C1-2 (15 m)) has (1) low pH, high alkalinity and elevated T [high $CO_2$ content of the venting fluids will result in a decrease of pH and increase of alkalinity (Zeebe and Wolf-Gladrow, 2001)]; (2) low concentrations of $SO_4^{2-}$ (the end-member hydrothermal fluid has zero sulfate)); (3) high concentrations of Zn, Cu, Mn, Sn, Ag, Pb, Mo and Si (the hydrothermal fluids are rich in these elements); and (4) the lightest both $\delta^{18}O$ (towards the hydrothermal fluid value), and $\delta^{34}S_{SO4}$ (towards the hydrothermal fluid value), and $\delta^{66}Zn$ (Zn isotope fractionation during carbonate spire formation; see *6.2*) (Fig. 7). The low concentrations of V and Ni at the lake bottom (samples C1-1 (23 m; V = 2.16 ppb, Ni = 1.85 ppb) and C1-2 (15 m; V = 2.12 ppb, Ni = 1.70 ppb)), even below their content in the hydrothermal fluid (V = 74.1 ppb, Ni = 2.09 ppb; Fig. 7), can be explained by adsorption on and co-precipitation with hydrothermally precipitated carbonates (e.g., Olsson et al., 2014) at the lake bottom. All this data suggests a hydrothermal discharge from the lake bottom close to Site C1.

In addition to the near-bottom hydrothermal signature, the vertical distributions of the concentrations of some elements across the Lake Asal water body show another essential feature: surface maxima (Fig. 7). The surface maxima of $Cl^-$ and $SO_4^{2-}$ concentrations, which correlates positively with that of the temperature, can be explained as a result of the solar heating and salinity increase due to evaporation. An alternative explanation of the $Cl^-$ and $SO_4^{2-}$ content surface maxima as well as those of the concentrations of Fe, Mn, Cu, V, Ni, U and Co (Fig. 7) is that they are possibly a result of aeolian (windblown) input to the lake surface. Whereas Fe, Mn, Cu, V, Ni, U and Co can be supplied within the windblown dust (e.g., Mendez et al., 2010; Sholkovitz et al., 2010) from the nearby deserts, $Cl^-$ and $SO_4^{2-}$ can likely be delivered to the lake within the windblown marine aerosols (e.g., Fitzgerald, 1991) from the nearby (~200 km; Fig. 1 A) ocean. The sharp decrease in the concentrations of Fe, Mn, Cu, V, Ni, U and Co in the subsurface water layer (sample C1-4 (5 m)) (Fig. 7) seems to be a result of their oxidation or scavenging. Zinc isotope composition of the surface water layer (Fig. 7) also suggests for aeolian dust input. Unlike the waters below the surface (deeper than 5 m) that have negative $\delta^{66}Zn$ (see *6.2*) the surface water layer has positive $\delta^{66}Zn$ (Table 7, Fig. 7). This trend of heavier $\delta^{66}Zn$ from the bottom towards the lake surface can be explained with aeolian supply of dust having isotope composition of the instantly soluble Zn of 0.25‰ very close to $\delta^{66}Zn_{Earth\ crust}$ = 0.18‰ (Little et al., 2014).

This suggests that there are two genetically different sources of elements to the Lake Asal that are vertically separated: hydrothermal (lower, or bottom) and aeolian (upper, or surficial).

*6.4. Oceanic "embryos" in arid climate: acidic and metal rich*

We infer that Lake Asal is fed by seafloor-type hydrothermal fluids and that the hydrothermal fluid venting at Site 3 (3-nov) can be regarded as a fluid type that fills the lake. If no precipitation or accumulation of the elements supplied by the hydrothermal fluid occur in the lake, then the lake water should have chemical composition similar to that of the hydrothermal fluid. However, we observe enrichment of some elements and depletion of others in the lake water relative to the hydrothermal fluid (Table 5; Fig. 7). In respect to the elemental concentrations in the lake water relative to their concentrations in the hydrothermal fluid the studied elements can be divided in two groups: (1) elements that are enriched in the lake water relative to the hydrothermal fluid

(Zn, Cu, Mn, Sn, Pb, U, and Co), and (2) elements that are depleted in the lake water relative to the hydrothermal fluid (Fe, Ag, V, Mo, and Si) (Table 5; Fig. 7). The first group of elements has obviously been accumulated in the lake water, whereas the elements from the second group have been removed from the source fluid.

Previous studies showed that under hydrothermal conditions the chloride complexes are the predominant Zn (Mei et al., 2015; Zhong et al., 2015), Cu (Liu and McPhail, 2005; Zhong et al., 2015), Pb (Zhong et al., 2015), Mn (Tian et al., 2014), Sn (Schmidt, 2018) and Co (Liu et al., 2011) species. We can hypothesize that the chloride complexes of Zn, Cu, Pb, Mn, Sn and Co injected with the hydrothermal fluids into the hypersaline Lake Asal water have been stabilized and accumulated with time. The most remarkable accumulation is that of Zn showing concentration in the lake water two orders of magnitude higher than that in the hydrothermal fluid (Fig. 7). Uranium accumulation in the Lake Asal water is also notable (Fig. 7). In the starting fluid, seawater, U has an average concentration of 3.3 ppb (Ku et al., 1977). However, during the hydrothermal circulation through the oceanic crust U behaves coherently with Mg and is quantitatively removed (~98%) from seawater (Michard and Albarède, 1985; Chen et al., 1986). Consequently, the seafloor end-member hydrothermal fluids are depleted in U. Indeed, the Lake Asal hydrothermal fluid is two orders of magnitude depleted in U relative to the seawater (Table 5; Fig. 7). However, in the Lake Asal water U obviously accumulates: its concentration is two orders of magnitude higher than that in the hydrothermal fluid (Table 5; Fig. 7). The minimum in the U concentration at 5 m water depth (Fig. 7) may be due to scavenging on the particulate Fe-oxyhydroxides (e.g., German et al., 1991) inferred to happen at that depth (see *6.3*).

The low pH of the hydrothermal fluids filling the Lake Asal accounts for the mild acidity of the lake water (Table 1; Fig. 7). On the other hand, simple evaporation of seawater can result in a decrease in the pH from ~8.2 to 7.0 (McCaffrey et al., 1987; Isaji et al., 2017). However, evaporation alone cannot explain pH value of down to 6.54 like that in the Lake Asal (Table 1). Therefore, the only reasonable explanation for the mildly acidic water of the Lake Asal is its hydrothermal origin. Indeed, the pH of the Lake Asal hydrothermal fluids (Table 1) is within the pH range of the modern seafloor hydrothermal fluids (German and Von Damm, 2003). The pH variations in these fluids depend generally on the temperature, water/rock ratio and precipitation of some minerals (e.g., anhydrite) (Pierre et al., 2018). Thus, the pH variation in the hydrothermal fluids measured during different sampling campaigns (Table 1) may be ascribed to variations of

temperature, water/rock ratio and mineral precipitation in the discharge zone of the hydrothermal system. These variations likely account for the different pH of the Lake Asal hydrothermal fluid (Site 3) and Lake Asal bottom water (samples C1-1, C1-2) inferred to be recharged by hydrothermal fluids.

Our calculations show a striking accumulation of some metals (notably Li, Mn and Zn) in the Lake Asal water (Table 10) and suggest that an "embryonic" ocean located in an arid zone is metal rich and mildly acidic.

*6.5. Formation of carbonate spires in the Lake Asal: $(Mg/Ca)_{mol}$ control on spire mineralogy*

The vertical, spire-like form of the carbonate deposits at the Lake Asal shore suggests they formed underwater (e.g., Dekov et al., 2014). This seems reasonable in view of the substantial fluctuations of the Lake Asal water body in response to the climatic changes during the Holocene (Gasse and Fontes, 1989). The carbonate spires likely formed during the interaction of hydrothermal fluids with lake water, similar to the carbonate spires of the Lake Abhé (Dekov et al., 2014) and tufa towers of the alkaline lakes (Bischoff et al., 1993; Rosen et al., 2004). U-Th age dating of the spires suggests that they had grown from the central zone outwards (Table 6).

Mineralogical zonation of the spires, low-Mg calcite + aragonite in the central (oldest) zone and aragonite + low-Mg calcite in the outer (younger) layers (Table 2; Fig. 4), gives some clues for the conditions of spire formation. According to the previous studies, the inorganic carbonate precipitation in seawater is primarily controlled by seawater Mg/Ca molar ratio (Sandberg, 1975; Wilkinson, 1979; Hardie, 1996; Morse et al., 1997). At $(Mg/Ca)_{mol} \leq 1$ low-Mg calcite precipitates, whereas at $1 < (Mg/Ca)_{mol} \leq 2$ high-Mg calcite precipitates. At $(Mg/Ca)_{mol}$ from ~2 to the present-day seawater value of 5.2 aragonite precipitates along with high-Mg calcite. At ratios substantially above 5 only aragonite precipitates.

Thus, from the Lake Asal hydrothermal fluid with $(Mg/Ca)_{mol} = 0.24$ (Table 5) only low-Mg calcite can precipitate. Lake Asal water has $(Mg/Ca)_{mol} = 6.70$, which is well above that of the local seawater [$(Mg/Ca)_{mol} = 5.40$] (Table 5) and high enough for aragonite precipitation only. Mixing of these two fluids will result in mixed carbonates (low-Mg calcite, high-Mg calcite and aragonite) depending on the proportions of the fluids. Thus, the central (oldest) zone of the spires composed dominantly of low-Mg calcite had likely precipitated from a fluid mixture dominated

by a low $(Mg/Ca)_{mol}$ hydrothermal fluid [$(Mg/Ca)_{mol} < 2$; Fig. 9 A]. In contrast, the younger spire layers (LAs-2 and -1) composed dominantly of aragonite had precipitated from a fluid mixture dominated by a high $(Mg/Ca)_{mol}$ lake water [$(Mg/Ca)_{mol} > 2$; Fig. 9 B,C]. However, the Lake Asal water has high Mg/Ca molar ratio now and the studied spires formed ~15600 years ago (Table 6). Did the lake water have the same Mg/Ca molar ratio at the time of spire formation? Following our hypothesis that the Lake Asal water has originated from a seafloor-type hydrothermal fluid it seems logical to assume that at the beginning of the lake filling the primordial lake water had $(Mg/Ca)_{mol}$ close to that of the hydrothermal fluid (< 2). The high $(Mg/Ca)_{mol}$ of the recent lake water is obviously a result of long evolution of the low primary $(Mg/Ca)_{mol}$. Since the hydrothermal fluid is, in general, depleted in Mg (Table 5) it is not reasonable to assume that the $(Mg/Ca)_{mol}$ increase of the lake water may have been due to hydrothermal fluid portions rich in Mg. The only possibility for gradual increase in the $(Mg/Ca)_{mol}$ of lake water is the decrease of the Ca concentrations in it. The most plausible mechanism of Ca removal from the Lake Asal water seems to be Ca-carbonate deposition. In other words, the carbonate spire precipitation in the lake is a mineralogy self-control mechanism: precipitation of Ca-carbonate removes Ca from the lake water, increases $(Mg/Ca)_{mol}$ of the lake water and drives spire mineralogy from calcite to aragonite.

Overall, at the early stages of the Lake Asal development the lake water $(Mg/Ca)_{mol}$ was close to that of the hydrothermal fluid (<2) and the precipitated spires were composed of calcite (low-Mg calcite) (Fig. 9 A). With time the net removal of Ca to calcite (low-Mg calcite) spires at the lake bottom drove the $(Mg/Ca)_{mol}$ of lake water to high values (>2) and precipitation of aragonite dominated layers in the spires (Fig. 9 B,C). Mixed carbonate composition of the spire layers (low-Mg calcite dominated with aragonite, or aragonite dominated with low-Mg calcite) is a result of mixing of different proportions of the interplaying fluids: low $(Mg/Ca)_{mol}$ hydrothermal fluid and high $(Mg/Ca)_{mol}$ lake water.

Lake Abhé spire had also grown from the central zone outwards (Table 6) and is composed of alternating layers of low-Mg calcite and high-Mg calcite (Table 2). We do not have data on the $(Mg/Ca)_{mol}$ of Lake Abhé hydrothermal fluids, but may presume that they have $(Mg/Ca)_{mol} < 1$ as a result of Mg sequestration during water-rock interaction. The Lake Abhé water has $(Mg/Ca)_{mol} = 1.18$ (Table 5). Thus, the alternation of low-Mg and high-Mg calcite layers within the spire is

reasonably explained with fluctuation in the proportions of the mixing fluids: hydrothermal fluid and lake water.

*6.6. Hydrothermal fluid/lake water contribution to the spire composition: Sr isotope constraints*

We infer that the hydrothermal fluids venting at the Lake Asal shores are seawater, which has been modified during its interaction with the Asal Rift rocks: i.e., seafloor-type hydrothermal fluid. The hydrothermal fluid at Site 3 (sample 3-nov) was estimated to have chemical composition close to that of the actual end-member fluid (see *6.1.3*). Its Sr isotope composition is close to that of the local basalt and away from the Sr isotope composition of the seawater (Fig. 10 A; Tables 6, 7). Lake Asal water, which is accumulation of hydrothermal fluid modified through evaporation and mineral precipitation, has Sr isotope composition between those of the source fluid (hydrothermal fluid) and seawater (Fig. 10 A; Tables 6, 7). Hydrothermal carbonate spires at the Lake Asal bottom are a result of the interaction between the hydrothermal fluids and lake water. Therefore, simple mixing calculations based on the Sr concentrations and Sr isotope composition for these two fluids can give the proportions of the interacting fluids. We can see that at the beginning of the LAs spire formation 59% of its Sr is hydrothermally derived (Fig. 10 A). Meaning that the hydrothermal fluid accounts for 59% of the spire composition. The hydrothermal contribution to the spire composition increases to 68% in the younger spire layers (LAs-2 and -1; Fig. 10 A).

Similarly, mixing calculations for the Lake Abhé hydrothermal fluid and lake water show that high proportion of hydrothermal fluid (82-73%) accounts for the composition of the low-Mg calcite layers (LAb-1, -2, -4), whereas high proportion of lake water (88-96.5%) is responsible for the composition of the high-Mg calcite layers (LAb-3, -5, -6, -7, -8) (Fig. 10 B). In addition to the evidence that the Lake Abhé hydrothermal fluid is a result of interaction of water (groundwater?) with the local basalts the Sr isotope data suggest that the Lake Abhé water largely originates from the Awash River (Fig. 10 B).

Elemental concentrations and stable isotope ratios correlate with the proportions hydrothermal fluid/lake water that participated in the spire formation (Fig. 11). The correlation of Sr, Ba, REE and Th concentrations in the Lake Abhé spire with the lake water proportion (Fig. 11 A2, A4) suggests that the lake water is the major source of these elements in the spire. The evaporation

and related heavy C and O isotope composition of the lake water accounts for similar positive correlation of $\delta^{13}C$ and $\delta^{18}O$ of the spire with the lake water proportion (Fig. 11 A5). The correlation of the Cu concentration and magnitude of Eu anomaly (Eu/Eu*) with the hydrothermal fluid proportion (Fig. 11 A3) suggests that the hydrothermal fluid is the major source of Cu and Eu in the Lake Abhé spire.

Major hydrothermal supply of Cu, Zn, Ni and Co to the Lake Asal spire explains their increased concentrations in the spire layers with high hydrothermal proportion (Fig. 11 B2, B3). The decreasing Eu anomaly (Eu/Eu*) with increasing hydrothermal proportion in the spire layers (Fig. 11 B4) may be explained with progressive maturation of the hydrothermal system and exhausted in Eu source rocks. The increase in $\delta^{13}C$ and $\delta^{18}O$ with the decrease in lake water proportion in the spire layers (Fig. 11 B5) may be due to participation of smaller proportion of more evolved due to evaporation lake water: i.e., isotopically heavier. The positive $\delta^{66}Zn$ in the Lake Asal spires (Fig. 11 B6) was explained with Zn isotope fractionation due to preferential $^{66}Zn$ adsorption on carbonates (see *6.2*). The increased hydrothermal proportion in the spire layers is seemingly responsible for the heavier $\delta^{66}Zn$ (Fig. 11 B6).

*6.7. Oceanic "embryos" with light Fe?*

The correlation between the $\delta^{56}Fe$ values of the carbonate spire samples and hydrothermal fluid proportion participating in their precipitation (Fig. 11 A6, B6) implies for Fe isotope fractionation during spire formation. Due to analytical challenges we could not obtain Fe isotope data for the investigated fluids: hydrothermal and lake water (Table 7). However, in our interpretations we can use Fe isotope data from the previous works. If the fluids that fill Lake Asal are seafloor-type hydrothermal fluids (see *6.1*), they should have an Fe isotope composition similar to that of modern seafloor hydrothermal fluids, which ranges from -0.12 to -0.45‰ (Beard et al., 2003; Severmann et al., 2004). Lake Asal carbonate spire samples have heavier $\delta^{56}Fe$ values (-0.14 - +0.07‰; Table 6) relative to the seafloor vent fluids ($\delta^{56}Fe$ = -0.45 – -0.12‰, $\delta^{56}Fe_{average}$ = -0.29‰; Beard et al., 2003; Severmann et al., 2004), consistent with fractionation during oxidation of $Fe^{2+}_{aq}$ to $Fe^{3+}_{aq}$ (e.g., Severmann et al., 2004). Indeed, the $Fe^{2+}_{aq}$ dissolved in the low-oxygen Lake Asal hydrothermal fluid ($[O_2]$ = 0 – 0.08 mg/L, Site 3; Table 1) will be readily oxidized in the Lake Asal water with oxygen concentration of 1.90 – 8.80 mg/L

(Table 1). The oxidation of $Fe^{2+}_{aq}$ to $Fe^{3+}_{aq}$ and precipitation of $Fe^{3+}$-minerals in the spires will produce the observed positive Fe isotope fractionation and $\delta^{56}Fe$ increase relative to the parent hydrothermal fluid (Table 6). We may speculate that the carbonate spire formation at the Lake Asal bottom will result in deep lake water with Fe isotope composition lighter than that of the seafloor hydrothermal fluids: $\delta^{56}Fe < -0.12‰$. On the other hand, the Lake Asal surface receives Fe from the wind-blown dust (see *6.3*). The average Fe isotope composition of the aerosols, supposed to be the source of dissolved Fe in the Lake Asal surface water, is +0.10‰ (Beard et al., 2003). Hence, the Lake Asal water will have $\delta^{56}Fe$ ranging from the negative values of the seafloor hydrothermal fluids (< -0.12‰) to the positive values of the aeolian dust (+0.10‰). It appears that unlike an evolved open ocean with positive $\delta^{56}Fe$ (+0.24 – +0.71‰; Boyle et al., 2012) an "embryonic" ocean is at a state of "anemia" with light (rather negative) $\delta^{56}Fe$ (Tanaka and Hirata, 2018).

## 7. Summary: Scenarios of formation of the Lake Asal and Lake Abhé

Lake Asal, located at the point of interaction between an oceanic spreading ridge and a continental rift system, is considered to be an ocean at "embryonic" stage because the crust beneath it is of oceanic type and its water body is seawater-based. Scarce fresh water supply (rare rainfalls, questionable groundwater flux and no riverine input) seems to be a subordinate component in the lake water budget. Our data suggest that the lake is fed almost entirely by seafloor-type hydrothermal fluids. The dense network of faults and cracks related to extension in the Asal-Ghoubbet Rift provides pathways for the seawater to percolate down to the Asal tectonic depression (Fig. 12). During its passage to the Asal Rift the seawater is heated by the heat released from the magma reservoir located below the rift, reacts with the host rocks (mostly basalts) and evolves towards a seafloor-type hydrothermal fluid. These fluids fill the Asal depression and make the lake water body. Thus, the seawater/rock interaction seems to be the first control on the chemistry of an oceanic "embryo". Strong evaporation superimposed on the seafloor-type hydrothermal fluid pool is another control on its chemistry. The hyper salinity (high chloride content) caused by the evaporation leads to stabilization of many hydrothermally supplied metals as chloride complexes and their accumulation in the lake water. As a result, this type of "embryonic" ocean appears to be metal rich and mildly acidic. In addition, the

evaporation leads to a heavy C and O isotope composition of the water body. The interaction between the hydrothermal fluids and lake water results in deposition of carbonate spires at the lake bottom and this process appears to be a third control on the chemistry of an oceanic "embryo". Ca-carbonate precipitation changes the $(Mg/Ca)_{mol}$ of lake water and this results in changes in the carbonate mineralogy of the spires: from low-Mg calcite to aragonite. Adsorption on, co-precipitation with, and oxidation in Ca-carbonates results in Zn, Ca and Fe isotope fractionation and changes in the isotope composition of the lake water. In addition to the hydrothermal supply of chemical elements from the lake bottom the lake water body receives elements through the wind-blown dust. Thus, an oceanic "embryo" located in an arid zone has two genetically different sources of elements that are vertically separated: hydrothermal (lower, or bottom) and aeolian (upper, or surficial).

Lake Abhé forms in a continental rift: Gob Aad Basin (Fig. 13). However, unlike Lake Asal, Lake Abhé is generally fed by fresh water from the Awash River. Subjected to strong evaporation, Lake Abhé evolves towards saline and basic lake. In addition to the fresh riverine water the lake is fed by hot hydrothermal fluids. The Lake Abhé hydrothermal fluids, unlike those of Lake Asal, originate from fresh groundwater after its heating by local magmatic bodies and interaction with the host rocks. Carbonate chimneys form at the points of mixing between the hydrothermal fluids and lake water.

**Acknowledgements**

This research was supported by a Tokyo University of Marine Science and Technology internal grant, which is gratefully acknowledged. We are extremely grateful to the Djiboutian Government and Army for their efforts to facilitate our sampling campaigns. The numerous suggestions and constructive comments by an anonymous reviewer improved the paper significantly and are highly appreciated.

**Declaration of interests**

The authors declare that they have no known competing financial interests or personal relationships that could have appeared to influence the work reported in this paper.

## References

Alibo, D.S., Nozaki, Y., 1999. Rare earth elements in seawater: particle association, shale-normalization, and Ce oxidation. Geochim. Cosmochim. Acta 63, 363-372.

AlKhatib, M., Eisenhauer, A., 2017a. Calcium and strontium isotope fractionation in aqueous solutions as a function of temperature and reaction rate; I. Calcite. Geochim. Cosmochim. Acta 209, 296-319.

AlKhatib, M., Eisenhauer, A., 2017b. Calcium and strontium isotope fractionation during precipitation from aqueous solutions as a function of temperature and reaction rate; II. Aragonite. Geochim. Cosmochim. Acta 209, 320-342.

Amini, M., Eisenhauer, A., Böhm, F., Fietzke, J., Bach, W., Garbe-Schönberg, D., Rosner, M., Bock, B., Lackschewitz, K.S., Hauff, F., 2008. Calcium isotope ($\delta^{44/40}$Ca) fractionation along hydrothermal pathways, Logatchev field (Mid-Atlantic Ridge, 14°45'N). Geochim. Cosmochim. Acta 72, 4107-4122.

Aminot, A., Kérouel, R., 2007. Dosage automatique des nutriments dans les eaux marines: méthodes en flux continu. Ed. Ifremer, Méthodes d'analyse en milieu marin. 188 p.

Araoka, D., Yoshimura, T., 2019. Rapid purification of alkali and alkaline-earth elements for isotope analysis ($\delta^{7}$Li, $\delta^{26}$Mg, $^{87}$Sr/$^{86}$Sr, and $\delta^{88}$Sr) of rock samples using borate fusion followed by ion chromatography with a fraction collector system. Anal. Sci. 35, 751-757.

Audin, L., Quidelleur, X., Coulié, E., Courtillot, V., Gilder, S., Manighetti, I., Gillot, P.-Y., Tapponnier, P., Kidane, T., 2004. Palaeomagnetism and K-Ar and $^{40}$Ar/$^{39}$Ar ages in the Ali Sabieh area (Republic of Djibouti and Ethiopia): constraints on the mechanism of Aden ridge propagation into southeastern Afar during the last 10 Myr. Geophys. J. Int. 158, 327-345.

Bäcker, H., Clin, M., Lange, K., 1973. Tectonics in the Gulf of Tadjura. Mar. Geol. 15, 309-327.

Barberi, F., Tazieff, H., Varet, J., 1972. Volcanism in the Afar depression: Its tectonic and magmatic significance. Tectonophysics 15, 19-29.

Barberi, F., Civetta, L., Varet, J., 1980. Sr isotopic composition of Afar volcanics and its implication for mantle evolution. Earth Planet. Sci. Lett. 50, 247-259.

Barrat, J.-A., Jahn, B.M., Fourcade, S., Joron, J.L., 1993. Magma genesis in an ongoing rifting zone: The Tadjoura Gulf (Afar area). Geochim. Cosmochim. Acta 57, 2201-2202.

Barrat, J.-A., Boulègue, J., Tiercelin, J.J., Lesourd, M., 2000. Strontium isotopes and rare-earth element geochemistry of hydrothermal carbonate deposits from Lake Tanganyika, East Africa. Geochim. Cosmochim. Acta 64, 287-298.

Bastow, I.D., Keir, D., 2011. The protracted development of the continent-ocean transition in Afar. Nat. Geosci. 4, 248-250.

Bayon, G., Henderson, G.M., Etoubleau, J., Caprais, J.-C., Ruffine, L., Marsset, T., Dennielou, B., Cauquil, E., Voisset, M., Sultan, N., 2015. U-Th isotope constraints on gas hydrate and pockmark dynamics at the Niger delta margin. Mar. Geol. 370, 87-98.

Beard, B.L., Johnson, C.M., Von Damm, K.L., Poulson, R.L., 2003. Iron isotope constraints on Fe cycling and mass balance in oxygenated Earth oceans. Geology 31, 629-632.

Benson, L., 1994. Carbonate deposition, Pyramid Lake Subbasin, Nevada: 1. Sequence of formation and elevational distribution of carbonate deposits (Tufas). Palaeogeogr. Palaeocl. Palaeoecol. 109, 55-87.

Bischoff, J.L., Stine, S., Rosenbauer, R.J., Fitzpatrick, J.A., Stafford, Jr. T.W., 1993. Ikaite precipitation by mixing of shoreline springs and lake water, Mono Lake, California, USA. Geochim. Cosmochim. Acta 57, 3855-3865.

Boschetti, T., Awaleh, M.O., Barbieri, M., 2018. Waters from the Djiboutian Afar: A review of strontium isotopic composition and a comparison with Ethiopian waters and Red Sea brines. Water 10, 1700.

Boyle, E.A., John, S., Abouchami, W., Adkins, J.F., Echegoyen-Sanz, Y., Ellwood, M., Flegal, A.R., Fornace, K., Gallon, C., Galer, S., Gault-Ringold, M., Lacan, F., Radic, A., Rehkamper, M., Rouxel, O., Sohrin, Y., Stirling, C., Thompson, C., Vance, D., Xue, Z., Zhao, Y., 2012. GEOTRACES IC1 (BATS) contamination-prone trace element isotopes Cd, Fe, Pb, Zn, Cu, and Mo intercalibration. Limnol. Oceanogr.: Methods 10, 653-665.

Böhm, F., Gussone, N., Eisenhauer, A., Dullo, W.-C., Reynaud, S., Paytan, A., 2006. Calcium isotope fractionation in modern scleractinian corals. Geochim. Cosmochim. Acta 70, 4452-4462.

Branchu, P., Bergonzini, L., Delvaux, D., De Batist, M., Golubev, V., Benedetti, M., Klerkx, J., 2005. Tectonic, climatic and hydrothermal control on sedimentation and water chemistry of northern Lake Malawi (Nyasa), Tanzania. J. Afr. Earth Sci. 43, 433-446.

Bretzler, A., Osenbrück, K., Gloaguen, R., Ruprecht, J.S., Kebede, S., Stadler, S., 2011. Groundwater origin and flow dynamics in active rift systems – A multi-isotope approach in the Main Ethiopian Rift. J. Hydrol. 402, 274-289.

Carpenter, S.J., Lohmann, K.C., 1995. $\delta^{18}O$ and $\delta^{13}C$ values of modern brachiopod shells. Geochim. Cosmochim. Acta 59, 3749-3764.

Chen, J.H., Wasserburg, G.J., Von Damm, K.L., Edmond, J.M., 1986. The U–Th–Pb systematics in hot springs on the East Pacific Rise at 21°N and in the Guaymas Basin. Geochim. Cosmochim. Acta 50, 2467-2479.

Cheng, H., Edwards, R.L., Shen, C.-C., Polyak, V.J., Asmerom, Y., Woodhead, J., Hellstrom, J., Wang, Y., Kong, X., Spötl, C., Wang, X., Alexander, Jr. E.C., 2013. Improvements in $^{230}Th$ dating, $^{230}Th$ and $^{234}U$ half-life values, and U-Th isotopic measurements by multi-collector inductively coupled plasma mass spectrometry. Earth Planet. Sci. Lett. 371-372, 82-91.

Cheng, L., Normandeau, C., Bowden, R., Doucett, R., Gallagher, B., Gillikin, D.P., Kumamoto, Y., McKay, J.L., Middlestead, P., Ninnemann, U., Nothaft, D., Dubinina, E.O., Quay, P., Reverdin, G., Shirai, K., Mørkved, P.T., Theiling, B.P., van Geldern, R., Wallace, D.W.R., 2019. An international intercomparison of stable carbon isotope composition measurements of dissolved inorganic carbon in seawater. Limnol. Oceanogr.: Methods 17, 200-209.

Cotton, J., Le Dez, A., Bau, M., Caroff, M., Maury, R.C., Dulski, P., Fourcade, S., Bohn, M., Brousse, R., 1995. Origin of anomalous rare-earth element and yttrium enrichments in subaerially exposed basalts: evidence from French Polynesia. Chem. Geol. 119, 115-138.

Courtillot, V., Galdéano, A., Le Mouel, J.L., 1980. Propagation of an accreting plate boundary: A discussion of new aeromagnetic data in the Gulf of Tadjurah and Southern Afar. Earth Planet. Sci. Lett. 47, 144-160.

Courtillot, V., Achache, J., Landre, F., Bonhommet, N., Galibert, P.Y., Montigny, R., Féraud, G., 1984. Episodic spreading and rift propagation: New paleomagnetic and geochronologic data from the Afar passive margin. J. Geophys. Res. 89, 3315-3333.

Damak, F., Asano, M., Baba, K., Suda, A., Araoka, D., Wali, A., Isoda, H., Nakajima, M., Ksibi, M., Tamura, K., 2019. Interregional traceability of Tunisian olive oils to the provenance soil by multielemental fingerprinting and chemometrics. Food Chem. 283, 656-664.

D'Amore, F., Giusti, D., Abdallah, A., 1998. Geochemistry of the high-salinity geothermal field of Asal, Republic of Djibouti, Africa. Geothermics 27, 197-210.

Dekov, V.M., Egueh, N.M., Kamenov, G.D., Bayon, G., Lalonde, S.V., Schmidt, M., Liebetrau, V., Munnik, F., Fouquet, Y., Tanimizu, M., Awaleh, M.O., Guirreh, I., Le Gall, B., 2014. Hydrothermal carbonate chimneys from a continental rift (Afar Rift): Mineralogy, geochemistry and mode of formation. Chem. Geol. 387, 87-100.

Deng, Y., Ren, J., Guo, Q., Cao, J., Wang, H., Liu, C., 2017. Rare earth element geochemistry characteristics of seawater and porewater from deep sea in western Pacific. Sci. Rep. 7, 16539.

Dong, S., Wasylenki, L.E., 2016. Zinc isotope fractionation during adsorption to calcite at high and low ionic strength. Chem. Geol. 447, 70-75.

Doubre, C., Manighetti, I., Dorbath, C., Dorbath, L., Jacques, E., Delmond, J.C., 2007. Crustal structure and magmato-tectonic processes in an active rift (Asal-Ghoubbet, Afar, East Africa): 1. Insights from a 5-month seismological experiment. J. Geophys. Res. 112, B05405.

Elderfield, H., Greaves, M.J., 1982. The rare earth elements in seawater. Nature 296, 214-219.

Fantle, M.S., Tipper, E.T., 2014. Calcium isotopes in the global biogeochemical Ca cycle: Implications for development of a Ca isotope proxy. Earth-Sci. Rev. 129, 148-177.

Fitzgerald, J.W., 1991. Marine aerosols: A review. Atmos. Environ. Part A. General Topics 25, 533-545.

Fouillac, A.M., Fouillac, C., Cesbron, F., Pillard, F., Legendre, O., 1989. Water-rock interaction between basalt and high-salinity fluids in the Asal Rift, Republic of Djibouti. Chem. Geol. 76, 271-289.

Friedman, G.M., 1959. Identification of carbonate minerals by staining methods. J. Sediment. Petrol. 29, 87-97.

Gasse, F., Fontes, J.-C., 1989. Palaeoenvironments and palaeohydrology of a tropical closed lake (Lake Asal, Djibouti) since 10,000 yr B.P. Palaeogeogr. Palaeoclimatol. Palaeoecol. 69, 67-102.

German, C.R., Von Damm, K.L., 2003. Hydrothermal processes. In: Turekian, K.K., Holland, H.D. (Eds), *Treatise on Geochemistry*, Vol. 6 The Oceans and Marine Geochemistry, Elsevier, Oxford, pp. 181-222.

German, C.R., Fleer, A.P., Bacon, M.P., Edmond, J.M., 1991. Hydrothermal scavenging at the Mid-Atlantic Ridge: radionuclide distributions. Earth Planet. Sci. Lett. 105, 170-181.

Goldsmith, J.R., Graf, D.L., 1958. Relation between lattice constants and composition of the Ca-Mg carbonates. Am. Mineral. 43, 84-101.

Granina, L.Z., Klerkx, J., Callender, E., Leermakers, M., Golobokova, L.P., 2007. Bottom sediments and pore waters near a hydrothermal vent in Lake Baikal (Frolikha Bay). Russ. Geol. Geophys. 48, 237-246.

Hardie, L.A., 1996. Secular variation in seawater chemistry: An explanation for the coupled secular variation in the mineralogies of marine limestones and potash evaporites over the past 600 m.y. Geology 24, 279-283.

Heuser, A., Eisenhauer, A., Gussone, N., Bock, B., Hansen, B.T., Nägler, T.F., 2002. Measurement of calcium isotopes ($\delta^{44}$Ca) using a multicollector TIMS technique. Int. J. Mass Spectrom. 220, 387-399.

Hori, M., Takashima, C., Marsuoka, J., Kano, A., 2009. Carbon and oxygen stable isotopic measurements of carbonate and water samples using mass spectrometer with gas bench. Bulletin of the Graduate School of Social and Cultural Studies, Kyushu University 15, 51-57.

Horton, T.W., Defliese, W.F., Tripati, A.K., Oze, C., 2016. Evaporation induced $^{18}$O and $^{13}$C enrichment in lake systems: A global perspective on hydrologic balance effects. Quat. Sci. Rev. 131, 365-379.

Isaji, Y., Kawahata, H., Kuroda, J., Yoshimura, T., Ogawa, N.O., Suzuki, A., Shibuya, T., Jiménez-Espejo, F.J., Lugli, S., Manzi, V., Roveri, M., Ohkouchi, N., 2017. Biological and physical modification of carbonate system parameters along the salinity gradient in shallow hypersaline solar saltems in Trapani, Italy. Geochim. Cosmochim. Acta 208, 354-367.

John, S.G., Bergquist, B.A., Saito, M.A., Boyle, E.A., 2005. Zinc isotope variations in phytoplankton and seawater. Geochim. Cosmochim. Acta 69, A546.

John, S.G., Rouxel, O.J., Craddock, P.R., Engwall, A.M., Boyle, E.A., 2008. Zinc stable isotopes in seafloor hydrothermal vent fluids and chinmeys. Earth. Planet. Sci. Lett. 269, 17-28.

Keeling, C.D., 1979. The Suess effect: $^{13}$Carbon-$^{14}$Carbon interrelations. Environ. Int. 2, 229-300.

Klinkhammer, G.P., Elderfield, H., Edmond, J.M., Mitra, A., 1994. Geochemical implications of rare earth element patterns in hydrothermal fluids from mid-ocean ridges. Geochim. Cosmochim. Acta 58, 5105-5113.

Ku, T.-L., Knauss, K.G., Mathieu, G.G., 1977. Uranium in open ocean: concentration and isotopic composition. Deep-Sea Res. 24, 1005-1017.

Labidi, J., Cartigny, P., Birck, J.L., Assayag, N., Bourrand, J.J., 2012. Determination of multiple sulfur isotopes in glasses: A reappraisal of the MORB $\delta^{34}$S. Chem. Geol. 334, 189-198.

Little, S.H., Vance, D., Walker-Brown, C., Landing, W.M., 2014. The oceanic mass balance of copper and zinc isotopes, investigated by analysis of their inputs, and outputs to ferromanganese oxide sediments. Geochim. Cosmochim. Acta 125, 673-693.

Liu, W., McPhail, D.C., 2005. Thermodynamic properties of copper chloride complexes and copper transport in magmatic-hydrothermal solutions. Chem. Geol. 221, 21-39.

Liu, W., Borg, S.J., Testemale, D., Etschmann, B., Hazemann, J.-L., Brugger, J., 2011. Speciation and thermodynamic properties for cobalt chloride complexes in hydrothermal fluids at 35–440 C and 600 bar: An *in-situ* XAS study. Geochim. Cosmochim. Acta 75, 1227-1248.

Liu, H.-C., You, C.-F., Huang, K.-F., Chung, C.-H., 2012. Precise determination of triple Sr isotopes ($\delta^{87}$Sr and $\delta^{88}$Sr) using MC-ICP-MS. Talanta 88, 338-344.

Ludwig, K.R., 2011. Using Isoplot/Ex, Version 4.15. A geochronological toolkit for Microsoft Excel: Berkeley Geochronology Ctr. Spec. Pub. 4.

Manighetti, I., Tapponnier, P., Gillot, P.-Y., Jacques, E., Courtillot, V., Armijo, R., Ruegg, J.C., King, G., 1998. Propagation of rifting along the Arabia-Somalia plate boundary: Into Afar. J. Geophys. Res. 103, B3, 4947-4974.

Marechal, C.N., Telouk, P., Albarede, F., 1999. Precise analysis of copper and zinc isotopic compositions by plasma-source mass spectrometry. Chem. Geol. 156, 251-273.

Maruo, M., Doi, T., Obata, H., 2006. Onboard determination of submicromolar nitrate in seawater by anion-exchange chromatography with lithium chloride eluent. Anal. Sci. 22, 1175-1178.

Mavromatis, V., González, A.G., Dietzel, M., Schott, J., 2019. Zinc isotope fractionation during the inorganic precipitation of calcite – Towards a new pH proxy. Geochim. Cosmochim. Acta 244, 99-112.

McCaffrey, M.A., Lazar, B., Holland, H.D., 1987. The evaporation path of seawater and the coprecipitation of $Br^-$ and $K^+$ with halite. J. Sediment. Petrol. 57, 928-937.

Mei, Y., Sherman, D.M., Liu, W., Etschmann, B., Testemale, D., Brugger, J., 2015. Zinc complexation in chloride-rich hydrothermal fluids (25-600°C): A thermodynamic model derived from *ab initio* molecular dynamics. Geochim. Cosmochim. Acta 150, 265-284.

Mendez, J., Guieu, C., Adkins, J., 2010. Atmospheric input of manganese and iron to the ocean: Seawater dissolution experiments with Saharan and North American dusts. Mar. Chem. 120, 34-43.

Michard, A., Albarède, F., 1985. Hydrothermal uranium uptake at ridge crests. Nature 317, 244-246.

Michard, A., Albaréde, F., Michard, G., Minster, J.F., Charlou, J.-L., 1983. Rare earth elements and uranium in high-temperature solutions from East Pacific Rise hydrothermal vent field (13°N). Nature 303, 795-797.

Millero, F.J., 2003. Physicochemical controls on seawater. In: Turekian, K.K., Holland, H.D. (Eds), *Treatise on Geochemistry*, Vol. 6 The Oceans and Marine Geochemistry, Elsevier, Oxford, pp. 1-21.

Minami, T., Konagaya, W., Zheng, L., Takano, S., Sasaki, M., Murata, R., Nakaguchi, Y., Sohrin, Y., 2015. An off-line automated preconcentration system with ethylenediaminetriacetate chelating resin for the determination of trace metals in seawater by high-resolution inductively coupled plasma mass spectrometry. Anal. Chim. Acta 854, 183-190.

Morita, S., Takagi, T., Kon, Y., Araoka, D., 2016. The accuracy and determination limits of rock chemical analysis by X-ray fluorescence spectrometry at Mineral Resources Research Group, Geological Survey of Japan. GSJ Open-File Report 624, 36 p.

Morse, J.W., Wang, Q., Tsio, M.Y., 1997. Influences of temperature and Mg:Ca ratio on $CaCO_3$ precipitates from seawater. Geology 25, 85-87.

Needham, H.D., Choukroune, P., Cheminee, J.L., Le Pichon, X., Francheteau, J., Tapponnier, P., 1976. The accreting plate boundary Ardoukoba Rift (northeast Africa) and the oceanic Rift Valley. Earth Planet. Sci. Lett. 28, 439-453.

Olsson, J., Stipp, S.L.S., Makovicky, E., Gislason, S.R., 2014. Metal scavenging by calcium carbonate at the Eyjafjallajökull volcano: A carbon capture and storage analogue. Chem. Geol. 384, 135-148.

Paris, G., Sessions, A.L., Subhas, A.V., Adkins, J.F., 2013. MC-ICP-MS measurement of $\delta^{34}S$ and $\Delta^{33}S$ in small amounts of dissolved sulfate. Chem. Geol. 345, 50-61.

Parkhurst, D.L., Appelo, C.A.J., 2013. Description of input and examples for PHREEQC version 3 - A computer program for speciation, batch-reaction, one-dimensional transport, and inverse geochemical calculations. U.S. Geological Survey Techniques and Methods 6, A43, 497 p.

Pflumio, C., Boulègue, J., Tiercelin, J.-J., 1994. Hydrothermal activity in the Northern Tanganyika Rift, East Africa. Chem. Geol. 116, 85-109.

Pierre, S., Gysi, A.P., Monecke, T., 2018. Fluid chemistry of mid-ocean ridge hydrothermall vents: A comparison between numerical modeling and vent geochemical data. Geofluids 2018, Article ID 1389379.

Ragueneau, O., Savoye, N., Del Amo, Y., Cotton, J., Tardiveau, B., Leynaert, A., 2005. A new method for the measurement of biogenic silica in suspended matter of coastal waters: using Si:Al ratios to correct for the mineral interference. Cont. Shelf Res. 25, 697-710.

Renaut, R.W., Owen, R.B., Jones, B., Tiercelin, J.-J., Tarits, C., Ego, J.K., Konhauser, K.O., 2013. Impact of lake-level changes on the formation of thermogene travertine in continental rifts: Evidence from Lake Bogoria, Kenya Rift Valley. Sedimentology 60, 428-468.

Rohling, E.J., 2013. Oxygen isotope composition of seawater. In: Elias, S.A. (Ed.), *The Encyclopedia of Quaternary Science*, Vol. 2, Elsevier, Amsterdam, pp. 915-922.

Rosen, M.R., Arehart, G.B., Lico, M.S., 2004. Exceptionally fast growth rate of <100-yr-old tufa, Big Soda Lake, Nevada: Implications for using tufa as a paleoclimate proxy. Geology 32, 409-412.

Sandberg, P.A., 1975. New interpretations of Great Salt Lake ooids and of ancient non-skeletal carbonate mineralogy. Sedimentology 22, 497-537.

Sanjuan, B., Michard, G., Michard, A., 1990. Origine des substances dissoutes dans les eaux des sources thermales et des forages de la région Asal-Ghoubbet (République de Djibouti). J. Volcanol. Geotherm. Res. 43, 333-352.

Scheuermann, P.P., Syverson, D.D., Higgins, J.A., Pester, N.J., Seyfried, Jr. W.E., 2018. Calcium isotope systematics at hydrothermal conditions: Mid-ocean ridge vent fluids and experiments in the CaSO4-NaCl-H2O system. Geochim. Cosmochim. Acta 226, 18-35.

Schmidt, C., 2018. Formation of hydrothermal tin deposits: Raman spectroscopic evidence for an important role of aqueous Sn(IV) species. Geochim. Cosmochim. Acta 220, 499-511.

Schmidt, G.A., Bigg, G.R., Rohling, E.J., 1999. Global Seawater Oxygen-18 Database – v1.22″. http://data.giss.nasa.gov/o18data/.

Severmann, S., Johnson, C.M., Beard, B.L., German, C.R., Edmonds, H.N., Chiba, H., Green, D.R.H., 2004. The effect of plume processes on the Fe isotope composition of hydrothermally derived Fe in the deep ocean as inferred from the Rainbow vent site, Mid-Atlantic Ridge, 36°14'N. Earth Planet. Sci. Lett. 225, 63-76.

Shanks, III W.C., 2001. Stable isotopes in seafloor hydrothermal systems: Vent fluids, hydrothermal deposits, hydrothermal alteration, and microbial processes. Rev. Mineral. Geochem. 43, 469-525.

Sholkovitz, E.R., Sedwick, P.N., Church, T.M., 2010. On the fractional solubility of copper in marine aerosols: Toxicity of aeolian copper revisited. Geophys. Res. Lett. 37, L20601.

Sohrin, Y., Urushihara, S., Nakatsuka, S., Kono, T., Higo, E., Minami, T., Norisuye, K., Umetani, S., 2008. Multielemental determination of GEOTRACES key trace metals in seawater by ICPMS after preconcentration using an ethylenediaminetriacetic acid chelating resin. Anal. Chem. 80, 6267-6273.

Stein, R.S., Briole, P., Ruegg, J.-C., Tapponnier, P., Gasse, F., 1991. Contemporary, Holocene, and Quaternary deformation of the Asal Rift, Djibouti: Implications for the mechanics of slow spreading ridges. J. Geophys. Res. 96, B13, 21789-21806.

Stieltjes, L., 1975. Research for a geothermal field in a zone of oceanic spreading example of the Asal Rift (French territory of the Afar and the Issdas, Afar depression, East Africa). Proc. 2nd U.N. Symp. On the Development and Use of Geothermal Resources. San Francisco, U.S.A. 1, 613-623.

Tanaka, Y., Hirata, T., 2018. Stable isotope composition of metal elements in biological samples as tracers for element metabolism. Anal. Sci. 34, 645-655.

Tang, J., Niedermayr, A., Köhler, S.J., Böhm, F., Kısakürek, B., Eisenhauer, A., Dietzel, M., 2012. $Sr^{2+}/Ca^{2+}$ and $^{44}Ca/^{40}Ca$ fractionation during inorganic calcite formation: III. Impact of salinity/ionic strength. Geochim. Cosmochim. Acta 77, 432-443.

Taylor, S.R., McLennan, S.M., 1985. The Continental Crust: Its Composition and Evolution. Blackwell Scientific, Oxford, 312 p.

Tian, Y., Etschmann, B., Mei, Y., Grundler, P.V., Testemale, D., Hazemann, J.-L., Elliott, P., Ngothai, Y., Brugger, J., 2014. Speciation and thermodynamic properties of manganese(II) chloride complexes in hydrothermal fluids: *In situ* XAS study. Geochim. Cosmochim. Acta 129, 77-95.

Tiercelin, J.-J., Pflumio, C., Castrec, M., Boulègue, J., Gente, P., Rolet, J., Coussement, C., Stetter, K.O., Huber, R., Buku, S., Mifundu, W., 1993. Hydrothermal vents in Lake Tanganyika, East African Rift system. Geology 21, 499-502.

Vellutini, P., 1990. The Manda-Inakir Rift, Republic of Djibouti: a comparison with the Asal Rift and its geodynamic interpretation. Tectonophysics 172, 141-153.

Vigny, C., de Chabalier, J.-B., Ruegg, J.-C., Huchon, P., Feigl, K.L., Cattin, R., Asfaw, L., Kanbari, K., 2007. Twenty-five years of geodetic measurements along the Tadjoura-Asal rift system, Djibouti, East Africa. J. Geophys. Res. 112, B06410.

Weis, D., Kieffer, B., Maerschalk, C., Pretorius, W., Barling, J., 2005. High-precision Pb-Sr-Nd-Hf isotopic characterization of USGS BHVO-1 and BHVO-2 reference materials. Geochem. Geophys. Geosyst. 6, Q02002.

Wilkinson, B.H., 1979. Biomineralization, paleoceanography, and the evolution of calcareous marine organisms. Geology 7, 524-527.

Wright, T.J., Sigmundsson, F., Pagli, C., Belachew, M., Hamling, I.J., Brandsdóttir, B., Keir, D., Pedersen, R., Ayele, A., Ebinger, C., Einarsson, P., Lewi, E., Calais, E., 2012. Geophysical constraints on the dynamics of spreading centres from rifting episodes on land. Nat. Geosci. 5, 242-250.

Yoshimura, T., Araoka, D., Tamenori, Y., Kuroda, J., Kawahata, H., Ohkouchi, N., 2018. Lithium, magnesium and sulfur purification from seawater using an ion chromatograph with a fraction collector system for stable isotope measurements. J. Chromatogr. A 1531, 157-162.

Zan, L., Gianelli, G., Passerini, P., Troisi, C., Haga, A.O., 1990. Geothermal exploration in the Republic of Djibouti: Thermal and geological data of the Hanlé and Asal areas. Geothermics 19, 561-582.

Zeebe, R.E., Wolf-Gladrow, D., 2001. $CO_2$ in Seawater: Equilibrium, Kinetics, Isotopes. Elsevier, Amsterdam, 360 p.

Zhang, J., Quay, P.D., Wilbur, D.O., 1995. Carbon isotope fractionation during gas-water exchange and dissolution of $CO_2$. Geochim. Cosmochim. Acta 59, 107-114.

Zhong, R., Brugger, J., Chen, Y., Li, W., 2015. Contrasting regimes of Cu, Zn and Pb transport in ore-forming hydrothermal fluids. Chem. Geol. 395, 154-164.

**Fig. 1.** (A) Digital elevation model of the eastern part of the Afar Rift showing the extensional fault network in the Lake Abhé – Lake Asal area: a range of horsts and grabens. Vertical color scale = altitude in m; red lines = faults; rectangle encloses the Asal-Ghoubbet Rift (enlarged in B); for Legend see B. (B) Tectonics and volcanism of the Asal-Ghoubbet Rift with the sampling sites. F = Fieale volcano, SB = Shark Bay volcano.

**Fig. 2.** Inactive carbonate spires at the shores of the Lake Asal (A) (~1.20 m tall), and Lake Abhé (B) (~12 m tall).

**Fig. 3.** Cross-sections of the studied spires with sample locations: (A) spire LAs from the Lake Asal (samples LAs-3, -2, -1); (B) spire LAb from the Lake Abhé (samples LAb-1, -2, … -8). For location of the spires see Figure 1 A,B.

**Fig. 4.** Photomicrographs (thin section of sample LAs stained with Feigl's solution, optical polarizing microscope, transmitted light) of: (A) concentrically zoned Mg-calcite (Mg-cc) crystals (‖N; LAs-3); (B) same as at (A) at ×N; (C) aragonite needle-like crystals (ar; black) over Mg-calcite (Mg-cc; transparent) and overgrown by Mg-calcite (transparent) (‖N; transition between LAs-3 and LAs-2); (D) same as at (C) at ×N; (E) botryoids of needle-like aragonite (ar; black) overgrown by Mg-calcite (Mg-cc; transparent) (‖N; LAs-2); (F) same as at (E) at ×N; (G) needle-like aragonite crystals (ar; black) overgrown by Mg-calcite (Mg-cc; transparent) (‖N; LAs-1); (H) same as at (G) at ×N. For the positions of samples LAs-3, -2, -1 see Figure 3 B.

**Fig. 5.** Photomicrographs (thin section of sample LAb, optical polarizing microscope, transmitted light) of: (A) cross-section of botryoidal surface of the layer LAb-3 showing radial Mg-calcite (Mg-cc) crystals (‖N; LAb-3); (B) same as at (A) at ×N; (C) skeletal Mg-calcite (Mg-cc) crystals (‖N; LAb-1); (D) same as at (C) at ×N. For the positions of samples LAb-3, -1 see Figure 3 A.

**Fig. 6.** Post-Archean Australian Shale-normalized (Taylor and McLennan, 1985) REE distribution patterns of: (A) Lake Asal spire (LAs); (B) Lake Abhé spire (LAb) (open symbols = low-Mg calcite samples, closed symbols = high-Mg calcite samples; for sample mineralogy see Table 2); and (C) Lake Asal and Lake Abhé waters. For sample locations and IDs see Figure 3 and Table 1.

**Fig. 7.** Vertical distributions of pH, T, alkalinity, concentrations of major dissolved species and trace elements, and isotope ratios across the Lake Asal water body: C1 profile. For data values, see Tables 1, 5 and 7. HF = data values for the hydrothermal fluid reference sample 3-nov, Site 3, Lake Asal. Surface, intermediate, and bottom water layers are given in blue colors: from light blue (surface water) to deep blue (bottom water).

**Fig. 8.** Sulfate-chloride concentration diagram and mixing calculations between the Lake Asal water and end-member hydrothermal fluid. Seawater ($[Cl^-]$=19.6 g/L, $[SO_4^{2-}]$=2.77 g/L; (Table 5)) is the primary fluid from which the theoretical end-member hydrothermal fluid originates after seawater/rock interaction, and loss of $SO_4^{2-}$ and retention of $Cl^-$ ($[Cl^-]$=19.6 g/L, $[SO_4^{2-}]$=0 g/L). Upwelling end-member hydrothermal fluid mixes with downwelling Lake Asal water ($[Cl^-]_{average}$=277 g/L, $[SO_4^{2-}]_{average}$=3.47 g/L, (Table 5)) and vents at the lake bottom. Venting fluid (Site 3 hydrothermal fluid with $[Cl^-]$=27.2 g/L and $[SO_4^{2-}]$=0.31 g/L (Table 5)) does not lie on the mixing line between the theoretical end-member hydrothermal fluid and Lake Asal water. For more explanations see the text.

**Fig. 9.** Scenario of formation of the carbonate spires from the Lake Asal: (A) Hydrothermal fluids migrate along faults/fractures in the basalt basement and discharge at the lake bottom. Mixed hydrothermal fluid-lake water has $(Mg/Ca)_{mol}<2$, low-Mg calcite + aragonite precipitate and build the core of the spire. (B) and (C) $(Mg/Ca)_{mol}$ of the mixed hydrothermal fluid-lake water increases [$(Mg/Ca)_{mol}>2$] and aragonite + low-Mg calcite precipitate. The spire grows outwards.

**Fig. 10.** Sr isotope composition for: (A) Asal Rift basalt, Lake Asal hydrothermal fluid, Lake Asal spire, Lake Asal water (average) and seawater from the Ghoubbet-al-Kharab (Tables 6, 7);

(B) Lake Abhé basalt (Dama Ale volcano; Barberi et al., 1980), Lake Abhé hydrothermal fluid (average; Table 7), Lake Abhé spire (Table 6), Lake Abhé water (Table 7) and Awash River (Bretzler et al., 2011). Mixing between hydrothermal fluid and lake water can explain the isotope composition of the spires, for more discussion see the text. Percents above bars show the relative amount of hydrothermal fluid Sr in the carbonate.

**Fig. 11.** Distribution of hydrothermal fluid contribution (1), elemental concentrations and ratios (2, 3, 4), and isotope composition (5, 6) across the spires of the Lake Abhé (A) and Lake Asal (B).

**Fig. 12.** Scenario of the Lake Asal formation: (A) Initial stage of discrete hydrothermal ponds. The Asal Rift as a north-west propagation of the Asal-Ghoubbet Rift (Fig. 1 A) forms due to crustal extension and rifting. Asal Rift depression is below the sea level in the Ghoubbet-al-Kharab and the seawater is pumped by the hydraulic pressure into the depression through cracks and faults. Seawater is heated by the high heat flux released from the magma chamber beneath the rift, interacts with the rocks (dominantly basalts) and discharges in the Asal Rift depression as hot springs of seafloor-type. Hydrothermal fluids fill separated ponds. (B) Stage of full lake. Hydrothermal fluids fill the Asal depression and form the Lake Asal. Carbonate spires precipitate at the points of hydrothermal discharge on the lake bottom. Lake reaches maximum volume. (C) Recent stage of shrinking lake. The high evaporation results in a decrease in the lake volume, saturation of the lake water in a number of salts and salt precipitation. The lake evolves towards a hypersaline, mildly acidic and enriched in some metals oceanic "embryo".

**Fig. 13.** Scenario of the Lake Abhé formation. Lake Abhé is fed by the Awash River in the Gob Aad Basin nearby the Dama Ale active volcano (Fig. 1 A). Groundwater beneath the lake is heated by the local magma chamber, interacts with the rocks and discharges as hot hydrothermal fluid in the lake. Carbonate spires form at the points of hydrothermal discharge on the lake bottom. High evaporation causes saturation of the lake water in some salts. The lake evolves towards a saline and basic water body.

**Table 1** Investigated fluid samples from the Afar Rift.

| Sample ID | Site ID | Sample type | Location | Latitude (N) | Longitude (E) | Altitude (m) | pH[1] | T (°C)[1] | T (°C)[2] | Alkalinity (mM) | Density (g/cm$^3$) | DO[3] (mg/L)[2] | DIC[4] (mmol/L | Site discription |
|---|---|---|---|---|---|---|---|---|---|---|---|---|---|---|

| | | | | | | | | | | | | ) | |
|---|---|---|---|---|---|---|---|---|---|---|---|---|---|
| 1 | Site 1 | seawater | Ghoubbet-al-Kharab | 11° 31.611' | 42° 31.422' | 0 | 8.15 | 28.5 | 28.8 | -[5] | 1.028 | 8.32 | 1.86 | Ghoubbet-al-Kharab |
| 2-1 | Site 2-1 | lake water | Lake Asal | 11° 36.319' | 42° 24.866' | -150 | 7.01 | 33.7 | 33.9 | - | 1.212 | 4.00 | 0.55 | Lake Asal, southern shore, orange-black mictobial mat |
| 2-1-nov | Site 2-1 | lake water | Lake Asal | - " - | - " - | -151 | 6.63 | 35.4 | - | 2.04 | - | 8.80 | - | - " - |
| 2-2 | Site 2-2 | hot pond water | Lake Asal | 11° 36.319' | 42° 24.866' | -125 | 7.75 | 31.2 | - | - | - | 3.20 | - | small water pond with tiny fishes, ~200 m off Lake Asal, southern shore |
| 3 | Site 3 | hydrothermal fluid | Lake Asal | 11° 36.225' | 42° 24.843' | -125 | 6.93 | 77.0 | 77.0 | - | 1.026 | 0.08 | 0.36 | hot spring Korili |
| 3-nov | Site 3 | hydrothermal fluid | Lake Asal | - " - | - " - | - " - | 6.70 | 76.7 | - | 0.35 | 1.032 | 0.00 | 0.41 | - " - |
| 3-1 | Site 3-1 | hot pond water | Lake Asal | 11° 36.206' | 42° 24.838' | -125 | 8.20 | 34.2 | - | - | | 8.70 | - | small pond ~50 m upstream from site 3 (inhabited by tiny fishes) |
| 3-1-nov | Site 3-1 | hot pond water | Lake Asal | - " - | - " - | - " - | 7.73 | 34.3 | 34.2 | 0.69 | 1.026 | 4.39 | 0.68 | - " - |
| 3-2 | Site 3-2 | creek water | Lake Asal | 11° 36.227' | 42° 24.825' | -127 | 7.39 | 52.0 | - | - | - | 7.86 | - | creek ~40 m downstream from site 3 |
| 4 | Site 4 | lake water over the salt plane | Lake Asal | 11° 37.309' | 42° 23.749' | -150 | 7.03 | 27.7 | 27.7 | - | - | 1.90 | - | Lake Asal, SW shore, bright white salt crystal plane |
| 5 | Site 5 | hydrothermal fluid | Lake Asal | 11° 36.777' | 42° 25.569' | -140 | 7.24 | 39.3 | 39.0 | - | 1.040 | 6.30 | 0.95 | hot spring |
| 5-2 | Site 5-2 | hydrothermal fluid | Lake Asal | 11° 36.777' | 42° 25.569' | -140 | - | - | - | - | - | - | - | hot spring, a few meters east from site 5 |
| 6 | Site 6 | hydrothermal fluid | Lake Asal | 11° 36.790' | 42° 25.600' | -147 | 7.35 | 41.1 | - | - | 1.038 | 6.00 | 0.90 | hot spring, midstream |
| 7 | Site 7 | lake water | Lake Asal | 11° 36.853' | 42° 24.237' | -151 | 6.85 | 30.9 | 31.2 | - | - | 4.56 | - | Lake Asal, southern shore, transparent crystals (salt?) with reddish mat |
| 7-nov | Site 7 | lake water | Lake Asal | - " - | - " - | - " - | 6.71 | 32.5 | - | 1.94 | - | 6.00 | - | - " - |
| C1-5 (0 m) | C1 | lake water | Lake Asal | 11° 35.226' | 42° 24.663' | -150 | 6.77 | 27.3 | - | 2.08 | 1.212 | - | 3.14 | water column sampling site 1, 0 m depth |
| C1-4 (5 m) | C1 | lake water | Lake Asal | - " - | - " - | - " - | 6.75 | 26.9 | - | 2.08 | - | - | - | water column sampling site 1, 5 m depth |
| C1-3 (10 m) | C1 | lake water | Lake Asal | - " - | - " - | - " - | 6.89 | 25.1 | - | 2.12 | - | - | - | water column sampling site 1, 10 m depth |
| C1-2 (15 m) | C1 | lake water | Lake Asal | - " - | - " - | - " - | 6.55 | 28.3 | - | 2.12 | - | - | - | water column sampling site 1, 15 m depth |
| C1-1 (23 m) | C1 | lake water | Lake Asal | - " - | - " - | - " - | 6.54 | 27.4 | - | 2.25 | 1.213 | - | 3.49 | water column sampling site 1, 23 m depth |
| C2-4 (0 m) | C2 | lake water | Lake Asal | 11° 38.738' | 42° 25.457' | -151 | 6.81 | 27.5 | - | 2.10 | - | - | - | water column sampling site 2, 0 m depth |
| C2-3 (5 m) | C2 | lake water | Lake Asal | - " - | - " - | - " - | 6.82 | 27.3 | - | 2.06 | - | - | - | water column sampling site 2, 5 m depth |
| C2-2 (10 m) | C2 | lake water | Lake Asal | - " - | - " - | - " - | 6.81 | 27.1 | - | 2.12 | - | - | - | water column sampling site 2, |

| | | | | | | | | | | | | | |
|---|---|---|---|---|---|---|---|---|---|---|---|---|---|
| C2-1 (22 m) | C2 | lake water | Lake Asal | - " - | - " - | - " - | 6.79 | 26.8 | - | 2.08 | - | - | - | 10 m depth water column sampling site 2, 22 m depth |
| Site 10 lake | Site 10 | lake water | Lake Abhé | 11˚ 11.349' | 41˚ 52.529' | 239 | 9.65 | 39 | | 1093 | 1.137 | - | - | pigmented in reddish-brown lake water, Lake Abhé, eastern shore |
| hot spring 1 | Site 11 | hydrothermal fluid | Lake Abhé | 11˚ 08.846' | 41˚ 52.878' | 250 | 7.42 | 95.5 | - | 0.37 | 1.001 | 0.00 | 0.36 | active hydrothermal vent at the base of a chimney |
| hot spring 2 | Site 14 | hydrothermal fluid | Lake Abhé | 11˚ 06.832' | 41˚ 52.501' | 256 | - | - | - | 0.22 | 1.001 | - | - | active hydrothermal vent at the base of a steaming ~10 m tall chimney |

[1] *In situ* measurement, pH meter.
[2] *In situ* measurement, DO meter.
[3] DO = dissolved oxygen.
[4] DIC = dissolved inorganic carbon.
[5] Not measured.

**Table 2** Mineralogy (XRD) of the investigated spires from the Afar Rift.

| Sample ID[1] | Location | Mineralogy[2] |
|---|---|---|
| LAs-1 | Lake Asal | aragonite, low-Mg calcite (2.0 mol.% $MgCO_3$), low-Mg calcite (2.3 mol.% $MgCO_3$) |
| LAs-2 | - " - | aragonite (42%), low-Mg calcite (2.0 mol.% $MgCO_3$) (41%), low-Mg calcite (2.4 mol.% $MgCO_3$) (17%) |
| LAs-3 | - " - | low-Mg calcite (3.0 mol.% $MgCO_3$), aragonite, calcite |
| LAs-salt | - " - | halite, gypsum (traces) |
| LAb-1 | Lake Abhé | low-Mg calcite (1.1 mol.% $MgCO_3$) (65%), low-Mg calcite (3.4 mol.% $MgCO_3$) (35%) |
| LAb-2 | - " - | low-Mg calcite (1.5 mol.% $MgCO_3$) (60%), low-Mg calcite (2.6 mol.% $MgCO_3$) (40%) |
| LAb-3 | - " - | high-Mg calcite (4.5 mol.% $MgCO_3$), high-Mg calcite (5.1 mol.% $MgCO_3$), low-Mg calcite (0.9 mol.% $MgCO_3$) |
| LAb-4 | - " - | low-Mg calcite (1.2 mol.% $MgCO_3$) (77%), low-Mg calcite (1.3 mol.% $MgCO_3$) (23%) |
| LAb-5 | - " - | high-Mg calcite (4.0 mol.% $MgCO_3$) (72%), low-Mg calcite (0.8 mol.% $MgCO_3$) (20%), high-Mg calcite (6.4 mol.% $MgCO_3$) (8%) |
| LAb-6 | - " - | high-Mg calcite (4.0 mol.% $MgCO_3$) (72%), low-Mg calcite (0.8 mol.% $MgCO_3$) (20%), high-Mg calcite (6.4 mol.% $MgCO_3$) (8%) |
| LAb-7 | - " - | high-Mg calcite (4.0 mol.% $MgCO_3$) (72%), low-Mg calcite (0.8 mol.% $MgCO_3$) (20%), high-Mg calcite (6.4 mol.% $MgCO_3$) (8%) |
| LAb-8 | - " - | high-Mg calcite (4.0 mol.% $MgCO_3$) (100%) |

[1] For sample positions across the spire wall see Figure 3.

[2] $MgCO_3$ (in mol. %) in calcite crystal lattice was calculated using $d_{104}$ values and the approach of Goldsmith and Graf (1958).

**Table 3** Chemical composition of the investigated spires from the Afar Rift.

| Sample ID | Location | Al (ppm) | Si | Mg | Ti | P | Fe | Mn | Sr | Ba | Rb | Li | Cu | Co | Ni | V | Zn | Pb | Cd |
|---|---|---|---|---|---|---|---|---|---|---|---|---|---|---|---|---|---|---|---|
| LAs-1 | Lake Asal | 19392 | 2103 | 31417 | 967 | 235 | 4856 | 310 | 10620 | 449 | 4.27 | 51.8 | 10.1 | 3.86 | 7.03 | 22.3 | 8.78 | 1.88 | 0.18 |
| LAs-2 | - " - | 2855 | 2010 | 35508 | 342 | 205 | 2552 | 76.8 | 3262 | 78.6 | 2.84 | 40.6 | 6.03 | 1.53 | 4.19 | 10.9 | 4.58 | 0.48 | 0.07 |
| LAs-3 | - " - | 512 | 467 | 10515 | 157 | 203 | 1315 | 55.5 | 964 | 41.3 | 1.20 | 3.43 | 2.41 | 1.10 | 2.21 | 3.42 | 2.75 | 0.24 | 0.06 |
| LAs-salt | - " - | <0.002 | -[1] | 716 | 0.02 | 5.71 | 1.44 | 4.95 | 4.83 | 0.04 | 0.38 | 0.39 | 0.02 | 0.001 | 0.05 | <0.000003 | 0.07 | 1.75 | 0.38 |
| LAs-basalt | - " - | 110943 | - | 31098 | 5846 | 585 | 44886 | 904 | 291 | 76.6 | 3.30 | 2.67 | 63.7 | 48.1 | 149 | 160 | 103 | 1.72 | 0.17 |
| LAb-1 | Lake Abhe | 283 | 95.8 | 5446 | 63.5 | 127 | 590 | 32.8 | 243 | 96.4 | 1.04 | 4.93 | 2.87 | 0.67 | 1.02 | 5.50 | 1.78 | 0.24 | <0.000001 |
| LAb-2 | - " - | 106 | 56.3 | 5341 | 7.36 | 112 | 101 | 32.6 | 299 | 120 | 0.12 | 3.66 | 2.63 | 0.51 | 0.35 | 2.70 | 1.14 | 0.22 | <0.000001 |
| LAb-3 | - " - | 164 | 655 | 24717 | 24.8 | 318 | 426 | 29.4 | 487 | 772 | 0.78 | 16.7 | 1.80 | 0.85 | 1.02 | 60.0 | 0.54 | 0.61 | <0.000001 |
| LAb-4 | - " - | 7.76 | 256 | 4773 | 3.77 | 95.0 | 52.0 | 18.1 | 278 | 105 | 0.09 | 3.49 | 5.08 | 0.90 | 0.28 | 2.05 | 0.30 | 0.34 | <0.000001 |
| LAb-5 | - " - | 853 | 1488 | 20576 | 166 | 40.6 | 1275 | 308 | 569 | 914 | 0.95 | 11.1 | 3.76 | 1.36 | 1.97 | 46.2 | 1.81 | 1.40 | <0.000001 |
| LAb-6 | - " - | 645 | 1088 | 16109 | 67.1 | 541 | 753 | 482 | 679 | 131 | 0.60 | 6.99 | 3.03 | 0.71 | 1.25 | 22.7 | 2.55 | 2.72 | <0.000001 |
| LAb-7 | - " - | 184 | 2953 | 27173 | 30.0 | 718 | 265 | 395 | 640 | 121 | 1.24 | 10.5 | 3.42 | 0.53 | 0.98 | 46.8 | 2.12 | 2.99 | <0.000001 |
| LAb-8 | - " - | 562 | 543 | 23894 | 75.8 | 1688 | 680 | 545 | 592 | 111 | 0.70 | 4.50 | 3.51 | 0.81 | 1.48 | 33.2 | 2.76 | 3.16 | <0.000001 |
| BHVO-2 | - | 52956 | - | 24908 | 15863 | 1130 | 70425 | 1140 | 334 | 114 | 5.11 | 2.64 | 109 | 42.6 | 113 | 306 | 95.9 | 1.25 | 0.18 |
| CAL-S | - | 57.3 | - | 2119 | 7.09 | 43.1 | 270 | 10.1 | 235 | 1.34 | <0.001 | <0.002 | 0.30 | 0.03 | 0.91 | 1.42 | 15.8 | 0.46 | 0.29 |

[1] Not measured.

| Sample ID | Location | Mo (ppm) | Tl | Cr | W | Ga | Sc | Hf | Th | U | Y | La | Ce | Pr | Nd | Sm | |
|---|---|---|---|---|---|---|---|---|---|---|---|---|---|---|---|---|---|
| LAs-1 | Lake Asal | 0.30 | 0.20 | 9.73 | 0.37 | 1.59 | 5.99 | 2.63 | 1.75 | 8.34 | 12.6 | 11.5 | 23.7 | 2.75 | 11.3 | 2.35 | |
| LAs-2 | -"- | 0.16 | <0.001 | 5.23 | <0.002 | 0.86 | <0.001 | <0.02 | 0.24 | 5.91 | 1.36 | 1.38 | 3.03 | 0.36 | 1.47 | 0.30 | |
| LAs-3 | -"- | 0.07 | <0.001 | 3.36 | <0.002 | 0.42 | <0.001 | <0.02 | 0.06 | 3.05 | 0.26 | 0.27 | 0.61 | 0.07 | 0.28 | 0.06 | |
| LAs-salt | -"- | 0.02 | <0.001 | 0.08 | <0.002 | <0.0003 | <0.001 | <0.02 | 0.0004 | <0.003 | <0.02 | 0.02 | 0.04 | <0.00002 | 0.02 | <0.001 | |
| LAs-basalt | -"- | 0.36 | <0.001 | 162 | 243 | 15.2 | 15.2 | 2.42 | 0.82 | 0.23 | 10.9 | 6.16 | 14.6 | 1.92 | 8.73 | 2.12 | |
| LAb-1 | Lake Abhe | 0.06 | <0.001 | 1.05 | <0.002 | 0.17 | <0.001 | <0.02 | 0.16 | 2.73 | 0.62 | 0.23 | 0.82 | 0.07 | 0.30 | 0.07 | |
| LAb-2 | -"- | 0.24 | <0.001 | 0.72 | <0.002 | 0.02 | <0.001 | <0.02 | 0.49 | 0.78 | 2.79 | 0.46 | 3.10 | 0.16 | 0.72 | 0.19 | |
| LAb-3 | -"- | 0.06 | <0.001 | 1.06 | <0.002 | 0.13 | <0.001 | 0.02 | 3.03 | 2.18 | 24.3 | 8.30 | 51.9 | 2.89 | 13.1 | 3.18 | |
| LAb-4 | -"- | 0.09 | <0.001 | 0.19 | <0.002 | 0.01 | <0.001 | <0.02 | 0.06 | 0.80 | 0.28 | 0.06 | 0.49 | 0.02 | 0.09 | 0.02 | |
| LAb-5 | -"- | 1.04 | <0.001 | 2.95 | <0.002 | 0.29 | <0.001 | <0.02 | 3.27 | 1.36 | 33.8 | 10.0 | 57.6 | 3.58 | 16.3 | 4.04 | |
| LAb-6 | -"- | 0.74 | <0.001 | 1.30 | <0.002 | 0.17 | <0.001 | <0.02 | 3.40 | 0.67 | 40.9 | 17.1 | 83.4 | 5.91 | 26.5 | 6.38 | |
| LAb-7 | -"- | 1.82 | <0.001 | 1.00 | <0.002 | 0.12 | <0.001 | <0.02 | 3.35 | 0.42 | 38.5 | 13.7 | 53.9 | 4.81 | 21.7 | 5.26 | |
| LAb-8 | -"- | 1.23 | <0.001 | 1.48 | <0.002 | 0.19 | <0.001 | <0.02 | 4.10 | 1.41 | 30.9 | 15.8 | 83.3 | 5.36 | 23.7 | 5.57 | |
| BHVO-2 | - | 3.58 | <0.001 | 261 | 0.34 | 18.5 | 15.2 | 4.61 | 0.61 | 0.45 | 12.7 | 13.0 | 32.4 | 4.56 | 21.1 | 4.94 | |
| CAL-S | - | 0.17 | <0.001 | 2.34 | <0.002 | 0.02 | <0.001 | | <0.001 | 0.93 | 1.24 | 0.53 | 0.21 | 0.06 | 0.25 | 0.04 | |

Table 3 (*continued*)

| Sample ID | Location | Eu (ppm) | Gd | Tb | Dy | Ho | Er | Tm | Yb | Lu | Y | ΣREE | $(Ce/Ce^*)^2$ | $(Eu/Eu^*)^3$ | $La_{PAASN}/Lu_{PAASN}$ |
|---|---|---|---|---|---|---|---|---|---|---|---|---|---|---|---|
| LAs-1 | Lake Asal | 0.65 | 2.03 | 0.38 | 2.15 | 0.43 | 1.22 | 0.18 | 1.14 | 0.17 | 12.6 | 59.9 | 0.97 | 1.40 | 0.76 |
| LAs-2 | - " - | 0.09 | 0.26 | 0.05 | 0.27 | 0.05 | 0.15 | 0.02 | 0.14 | 0.02 | 1.36 | 7.58 | 0.99 | 1.50 | 0.77 |
| LAs-3 | - " - | 0.02 | 0.05 | 0.01 | 0.05 | 0.01 | 0.03 | 0.004 | 0.03 | 0.004 | 0.26 | 1.48 | 1.04 | 1.89 | 0.74 |
| LAs-salt | - " - | <0.0000004 | 0.002 | <0.0001 | <0.0002 | <0.00002 | <0.0001 | <0.0002 | <0.0004 | <0.00006 | <0.0002 | | | | |
| LAs-basalt | - " - | 0.82 | 1.98 | 0.39 | 2.37 | 0.48 | 1.32 | 0.19 | 1.17 | 0.17 | 10.9 | 42.5 | 0.97 | 1.89 | 0.40 |
| LAb-1 | Lake Abhe | 0.03 | 0.06 | 0.01 | 0.10 | 0.02 | 0.07 | 0.01 | 0.07 | 0.01 | 0.62 | 1.89 | 1.49 | 2.51 | 0.24 |
| LAb-2 | - " - | 0.07 | 0.19 | 0.05 | 0.36 | 0.09 | 0.28 | 0.05 | 0.30 | 0.04 | 2.79 | 6.05 | 2.60 | 1.84 | 0.13 |
| LAb-3 | - " - | 0.98 | 3.12 | 0.69 | 4.47 | 0.92 | 2.57 | 0.34 | 1.86 | 0.24 | 24.3 | 94.6 | 2.40 | 1.47 | 0.39 |
| LAb-4 | - " - | 0.03 | 0.02 | 0.01 | 0.04 | 0.01 | 0.03 | 0.01 | 0.03 | 0.00 | 0.28 | 0.86 | 3.25 | 5.39 | 0.14 |
| LAb-5 | - " - | 1.28 | 4.04 | 0.93 | 6.21 | 1.30 | 3.64 | 0.49 | 2.64 | 0.33 | 33.8 | 113 | 2.17 | 1.49 | 0.34 |
| LAb-6 | - " - | 1.97 | 6.13 | 1.33 | 8.45 | 1.67 | 4.52 | 0.58 | 3.04 | 0.37 | 40.9 | 167 | 1.88 | 1.48 | 0.53 |
| LAb-7 | - " - | 1.61 | 5.05 | 1.13 | 7.47 | 1.54 | 4.26 | 0.57 | 2.99 | 0.36 | 38.5 | 124 | 1.50 | 1.47 | 0.43 |
| LAb-8 | - " - | 1.68 | 5.29 | 1.09 | 6.63 | 1.29 | 3.48 | 0.47 | 2.62 | 0.34 | 30.9 | 157 | 2.05 | 1.45 | 0.53 |
| BHVO-2 | - | 1.68 | 4.01 | 0.73 | 3.93 | 0.71 | 1.78 | 0.23 | 1.33 | 0.18 | 12.7 | | | | |
| CAL-S | - | 0.01 | 0.06 | 0.01 | 0.07 | 0.02 | 0.06 | 0.01 | 0.05 | 0.01 | 1.24 | | | | |

[2] $Ce/Ce^* = 2Ce_{PAASN}/(La_{PAASN}+Pr_{PAASN})$.
[3] $Eu/Eu^* = 2Eu_{PAASN}/(Sm_{PAASN}+Gd_{PAASN})$.

**Table 4** Major element concentrations (XRF) of basalt and salt (evaporite) from the Lake Asal.

| Sample | Measured as oxides | Recalculated as chlorides and |
|---|---|---|

| ID | | | | | | | | | | | | | sulfates | | | | |
|---|---|---|---|---|---|---|---|---|---|---|---|---|---|---|---|---|---|
| | $SiO_2$ (wt.%) | $TiO_2$ | $Al_2O_3$ | $Fe_2O_3$ | MnO | MgO | CaO | $Na_2O$ | $K_2O$ | $P_2O_5$ | LOI[1] | Total | $MgCl_2$ | $CaSO_4$ | NaCl | KCl | Total |
| LAs-basalt | 47.6 | 0.95 | 21.9 | 7.62 | 0.12 | 5.87 | 13.9 | 1.92 | 0.20 | 0.14 | -[2] | 100.1 | - | - | - | - | - |
| LAs-salt | 0.00 | 0.00 | 0.00 | 0.00 | 0.00 | 0.21 | 0.07 | 51.5 | 0.03 | 0.00 | - | 51.8 | 0.51 | 0.17 | 97.1 | 0.04 | 97.9 |

[1] At 1050°C for 2 hours.
[2] Not measured.

**Table 5** Chemical composition of the investigated fluid samples from the Afar Rift[1].

| Sample ID | Site ID | Location | Sample type | Na (ppm) | K | Si | Mg | Ca | $(Mg/Ca)_{mol}$ | Cl | Br | $SO_4$ | $NO_3$ | Fe (ppb) | Mn | Cu |
|---|---|---|---|---|---|---|---|---|---|---|---|---|---|---|---|---|
| 1 | Site 1 | Ghoubbet-al-Kharab | seawater | 10319 | 518 | -[2] | 1300 | 397 | 5.40 | 19570 | - | 2768 | - | - | - | - |
| C1-5 (0 m) | C1 | Lake Asal | lake water | 64794 | 3929 | 6.08 | 8702 | 2140 | 6.71 | 290438 | 880 | 3830 | 0.120 | 23.9 | 1674 | 12.2 |
| C1-4 (5 m) | C1 | Lake Asal | lake water | - | - | 6.07 | - | - | - | 272781 | 876 | 3373 | 0.195 | 3.21 | 706 | 11.7 |
| C1-3 (10 m) | C1 | Lake Asal | lake water | - | - | 6.10 | - | - | - | 274333 | 885 | 3647 | 0.115 | 3.67 | 427 | 12.0 |
| C1-2 (15 m) | C1 | Lake Asal | lake water | - | - | 6.09 | - | - | - | 276439 | 874 | 3221 | 0.121 | 3.18 | 1064 | 12.8 |
| C1-1 (23 m) | C1 | Lake Asal | lake water | 64860 | 3918 | 6.15 | 8699 | 2141 | 6.70 | 273102 | 889 | 3275 | 0.219 | 4.69 | 878 | 11.7 |
| C2-4 (0 m) | C2 | Lake Asal | lake water | - | - | - | - | - | - | 262042 | - | 3825 | 0.296 | 3.36 | 832 | 12.0 |
| C2-3 (5 m) | C2 | Lake Asal | lake water | - | - | - | - | - | - | 266653 | - | 3207 | 0.151 | 4.10 | 1250 | 11.7 |
| C2-2 (10 m) | C2 | Lake Asal | lake water | - | - | - | - | - | - | 245728 | - | 2995 | 0.114 | 4.89 | 1416 | 11.8 |
| C2-1 (22 m) | C2 | Lake Asal | lake water | - | - | - | - | - | - | 246827 | - | 3167 | 0.123 | 15.5 | 992 | 11.6 |
| 3-1-nov | Site 3-1 | Lake Asal | hot pond water | 8908 | 467 | 24.6 | 369 | 3112 | 0.20 | 28716 | 87.1 | 333 | <0.1 | 4.25 | 170 | 0.76 |
| 3-nov | Site 3 | Lake Asal | hydrothermal fluid | 8532 | 463 | 30.2 | 400 | 2737 | 0.24 | 27216 | 83.2 | 313 | 0.474 | 24.3 | 439 | 5.37 |
| Site 10 lake | Site 10 | Lake Abhé | lake water | 49349 | 1328 | 64.2 | 2 | 2.80 | 1.18 | 57062 | - | 26428 | - | 154 | 14.6 | 2.05 |
| hot spring 1 | Site 11 | Lake Abhé | hydrothermal fluid | 1264 | 47 | 52.2 | 0.2 | 303 | - | 2016 | - | 336 | - | 1.20 | 4.19 | 0.03 |

| | | | | | | | | | | | | | | | | |
|---|---|---|---|---|---|---|---|---|---|---|---|---|---|---|---|---|
| hot spring 2 | Site 14 | Lake Abhé | hydrothermal fluid | 520 | 24 | - | 0.1 | 162 | - | - | - | - | - | 0.81 | 0.59 | 1.03 |
| blank | - | - | blank | - | - | - | - | - | - | - | - | - | - | 0.08 | <0.083 | 0.02 |
| CASS-4 | - | - | standard | - | - | - | - | - | - | - | - | - | - | 0.90 | 2.56 | 0.68 |
| CASS-4 ref. values | - | - | standard | - | - | - | - | - | - | - | - | - | - | 0.71 | 2.78 | 0.59 |

[1] Na, Mg, K, Ca, Cl, Br, $SO_4$ and $NO_3$ concentrations measured by IC, concentrations of the rest elements measured by ICP-MS.
[2] Not measured.

| Sample ID | Site ID | Location | Sample type | Zn (ppb) | Mo | V | Ni | Co | U | Sn | Pb | Ag | Cd | Li | Sr | B |
|---|---|---|---|---|---|---|---|---|---|---|---|---|---|---|---|---|
| 1 | Site 1 | Ghoubbet-al-Kharab | seawater | - | - | - | - | - | - | - | - | - | - | 478 | 7485 | - |
| C1-5 (0 m) | C1 | Lake Asal | lake water | 469 | 7.82 | 2.42 | 4.22 | 0.72 | 1.12 | 0.10 | 0.35 | 0.016 | 0.026 | 6273 | 80562 | <10 |
| C1-4 (5 m) | C1 | Lake Asal | lake water | 475 | 9.31 | 2.29 | 1.65 | 0.63 | 0.89 | 0.19 | 0.71 | 0.015 | 0.029 | - | - | <10 |
| C1-3 (10 m) | C1 | Lake Asal | lake water | 487 | 11.9 | 2.35 | 3.63 | 0.65 | 1.01 | 0.40 | 0.66 | 0.020 | 0.033 | - | - | <10 |
| C1-2 (15 m) | C1 | Lake Asal | lake water | 498 | 9.93 | 2.12 | 1.70 | 0.69 | 1.09 | 0.58 | 0.37 | 0.017 | 0.028 | - | - | <10 |
| C1-1 (23 m) | C1 | Lake Asal | lake water | 487 | 11.2 | 2.14 | 1.85 | 0.67 | 1.10 | 0.39 | 1.12 | 0.037 | 0.032 | 6296 | 79685 | <10 |
| C2-4 (0 m) | C2 | Lake Asal | lake water | 483 | 11.4 | 2.28 | 1.68 | 0.68 | 1.09 | 1.05 | 0.33 | 0.017 | 0.032 | - | - | - |
| C2-3 (5 m) | C2 | Lake Asal | lake water | 479 | 7.08 | 2.14 | 1.73 | 0.67 | 1.12 | 1.12 | 0.27 | 0.019 | 0.021 | - | - | - |
| C2-2 (10 m) | C2 | Lake Asal | lake water | 481 | 8.15 | 2.31 | 1.72 | 0.68 | 1.08 | 0.41 | 0.38 | 0.015 | 0.027 | - | - | - |
| C2-1 (22 m) | C2 | Lake Asal | lake water | 490 | 9.89 | 2.18 | 2.14 | 0.68 | 1.05 | 0.54 | 4.42 | 0.019 | 0.028 | - | - | - |
| 3-1-nov | Site 3-1 | Lake Asal | hot pond water | 0.66 | 23.4 | 48.4 | 0.42 | 0.13 | 0.03 | 0.16 | <0.008 | 0.019 | 0.530 | 2480 | 40313 | <10 |
| 3-nov | Site 3 | Lake Asal | hydrothermal fluid | 1.23 | 24.4 | 74.1 | 2.09 | 0.22 | 0.01 | 0.16 | 0.10 | 0.346 | 2.398 | 2148 | 37022 | <10 |
| Site 10 lake | Site 10 | Lake Abhé | lake water | 0.65 | - | - | 1.17 | 0.07 | - | 0.38 | 1.09 | <LD[3] | - | 15 | 479 | <10 |
| hot spring 1 | Site 11 | Lake Abhé | hydrothermal fluid | 0.70 | 88.5 | 2.61 | 0.05 | <0.013 | 0.002 | 0.16 | <0.008 | <LD | 0.234 | 297 | 2017 | <10 |

| | | | | | | | | | | | | | | | | | |
|---|---|---|---|---|---|---|---|---|---|---|---|---|---|---|---|---|---|
| hot spring 2 | Site 14 | Lake Abhé | hydrothermal fluid | 0.63 | 84.7 | 0.34 | 0.07 | 0.003 | 0.002 | 0.39 | 0.02 | <LD | 0.232 | 149 | 1491 | - |
| blank | - | - | blank | 0.08 | <0.084 | <0.010 | 0.08 | <0.013 | <0.001 | <LD | <0.008 | <LD | <0.0063 | - | - | - |
| CASS-4 | - | - | standard | 0.65 | 9.52 | 1.15 | 0.51 | 0.02 | 2.85 | 0.07 | 0.011 | 0.0057 | 0.050 | - | - | - |
| CASS-4 ref. values | - | - | standard | 0.38 | 8.78 | 1.18 | 0.31 | 0.03 | 3 | - | 0.010 | 0.0005-0.26 | 0.026 | - | - | - |

[3] Below the limits of detection.

**Table 5** (*continued*)

| Sample ID | Site ID | Location | Sample type | Y (ppb) | La | Ce | Pr | Nd | Sm | Eu | Gd | Tb | Dy | Ho | Er | Tm | Yb | Lu |
|---|---|---|---|---|---|---|---|---|---|---|---|---|---|---|---|---|---|---|
| 1 | Site 1 | Ghoubbet-al-Kharab | seawater | - | - | - | - | - | - | - | - | - | - | - | - | - | - | - |
| C1-5 (0 m) | C1 | Lake Asal | lake water | 0.007 | 0.009 | 0.005 | 0.001 | 0.004 | 0.001 | <0.001 | <0.013 | <0.0001 | <0.0002 | <0.0003 | <0.0002 | <0.0004 | <0.001 | <0.00004 |
| C1-4 (5 m) | C1 | Lake Asal | lake water | 0.009 | 0.009 | 0.006 | 0.001 | 0.004 | 0.002 | <0.001 | <0.013 | <0.0001 | <0.0002 | <0.0003 | <0.0002 | <0.0004 | <0.001 | <0.00004 |
| C1-3 (10 m) | C1 | Lake Asal | lake water | 0.008 | 0.011 | 0.005 | 0.001 | 0.004 | <0.0006 | <0.001 | <0.013 | <0.0001 | <0.0002 | <0.0003 | 0.001 | <0.0004 | <0.001 | 0.0001 |
| C1-2 (15 m) | C1 | Lake Asal | lake water | 0.010 | 0.010 | 0.005 | 0.001 | 0.005 | 0.002 | <0.001 | <0.013 | <0.0001 | <0.0002 | <0.0003 | <0.0002 | <0.0004 | <0.001 | 0.0001 |
| C1-1 (23 m) | C1 | Lake Asal | lake water | 0.008 | 0.010 | 0.007 | 0.001 | 0.005 | 0.001 | <0.001 | <0.013 | <0.0001 | <0.0002 | <0.0003 | <0.0002 | <0.0004 | <0.001 | <0.00004 |
| C2-4 (0 m) | C2 | Lake Asal | lake water | 0.009 | 0.008 | 0.005 | 0.001 | 0.005 | 0.003 | <0.001 | <0.013 | <0.0001 | <0.0002 | <0.0003 | <0.0002 | <0.0004 | <0.001 | <0.00004 |
| C2-3 (5 m) | C2 | Lake Asal | lake water | 0.007 | 0.008 | 0.005 | 0.001 | 0.004 | 0.001 | <0.001 | <0.013 | <0.0001 | <0.0002 | <0.0003 | <0.0002 | <0.0004 | <0.001 | <0.00004 |
| C2-2 (10 m) | C2 | Lake Asal | lake water | 0.007 | 0.010 | 0.006 | 0.001 | 0.004 | <0.0006 | <0.001 | <0.013 | <0.0001 | <0.0002 | <0.0003 | <0.0002 | <0.0004 | <0.001 | <0.00004 |
| C2-1 (22 m) | C2 | Lake Asal | lake water | 0.007 | 0.009 | 0.005 | 0.001 | 0.004 | <0.0006 | <0.001 | <0.013 | <0.0001 | <0.0002 | <0.0003 | <0.0002 | <0.0004 | <0.001 | <0.00004 |
| 3-1-nov | Site 3-1 | Lake Asal | hot pond water | 0.004 | 0.008 | 0.006 | <0.0002 | 0.003 | 0.001 | <0.001 | <0.013 | <0.0001 | <0.0002 | <0.0003 | <0.0002 | <0.0004 | <0.001 | <0.00004 |
| 3-nov | Site 3 | Lake Asal | hydrothermal fluid | 0.004 | 0.031 | 0.006 | <0.0002 | 0.003 | 0.003 | <0.001 | <0.013 | <0.0001 | <0.0002 | <0.0003 | <0.0002 | <0.0004 | <0.001 | <0.00004 |
| Site 10 lake | Site 10 | Lake Abhé | lake water | 13.69 | 0.272 | 9.603 | 0.189 | 1.068 | 0.340 | 0.113 | 0.418 | 0.153 | 1.598 | 0.521 | 2.298 | 0.479 | 4.068 | 0.753 |

| | | | | | | | | | | | | | | | | | | | |
|---|---|---|---|---|---|---|---|---|---|---|---|---|---|---|---|---|---|---|---|
| hot spring 1 | Site 11 | Lake Abhé | hydrothermal fluid | 0.001 | 0.001 | 0.002 | <0.0002 | <0.001 | <0.0006 | <0.001 | <0.013 | <0.001 | <0.0002 | <0.0003 | <0.0002 | <0.0004 | <0.001 | <0.0004 |
| hot spring 2 | Site 14 | Lake Abhé | hydrothermal fluid | <0.0002 | <0.0003 | <0.0005 | <0.0002 | <0.001 | <0.0006 | <0.001 | <0.013 | <0.001 | <0.0002 | <0.0003 | <0.0002 | <0.0004 | <0.001 | <0.0004 |
| blank | - | - | blank | <0.0002 | <0.0003 | <0.0005 | <0.0002 | <0.001 | <0.0006 | <0.001 | <0.013 | <0.001 | <0.0002 | <0.0003 | <0.0002 | <0.0004 | <0.001 | <0.0004 |
| CASS-4 | - | - | standard | 0.018 | 0.008 | 0.004 | 0.001 | 0.005 | 0.005 | 0.000 2 | <0.013 | 0.0002 | 0.001 | 0.0004 | 0.001 | 0.0002 | 0.001 | 0.0002 |
| CASS-4 ref. values | - | - | standard | 0.010 | 0.011 | 0.004 | 0.001 | 0.005 | 0.005 | 0.000 2 | 0.001 | 0.000 | 0.001 | 0.0004 | 0.001 | 0.0002 | 0.001 | 0.0002 |

**Table 6** Isotope composition of the investigated spires from the Afar Rift.

| Sample ID | Location | $\delta^{13}C_{VPDB}$ (‰) | 2SD (‰) | $\delta^{18}O_{VPDB}$ (‰) | 2SD (‰) | $\delta^{44/40}Ca_{NIST\ SRM-915a}$ (‰) | 95% conf. (‰) | n[1] | SE[2] (‰) | $\delta^{66/64}Zn_{NIST\ SRM\ 683}$ (‰) | 2SD[3] (‰) | $\delta^{56/54}Fe_{IRMM-14}$ (‰) | 2SD[4] (‰) | $\delta^{57/54}Fe_{IRMM-14}$ (‰) | 2SD[4] (‰) |
|---|---|---|---|---|---|---|---|---|---|---|---|---|---|---|---|
| LAs-1 | Lake Asal | 6.42 | 0.04 | 3.68 | 0.03 | 1.06 | 0.12 | 6 | 0.0[illegible] | 0.21 | 0.07 | 0.07 | 0.07 | 0.08 | 0.16 |
| LAs-2 | - " - | 4.73 | 0.01 | 2.02 | 0.01 | 0.95 | 0.11 | 6 | 0.06 | 0.23 | 0.07 | 0.04 | 0.07 | 0.04 | 0.16 |
| LAs-3 | - " - | 3.89 | 0.01 | 2.15 | 0.03 | 0.22 | 0.0[illegible] | 3 | 0.03 | 0.07 | 0.07 | -0.14 | 0.07 | -0.13 | 0.16 |
| LAs-basalt | - " - | -[5] | - | - | - | - | - | - | - | - | - | 0.08 | 0.07 | 0.01 | 0.16 |
| LAb-1 | Lake Abhe | 1.44 | 0.04 | 0.07 | 0.04 | - | - | - | - | 0.06 | 0.07 | 0.07 | 0.07 | 0.13 | 0.16 |
| LAb-2 | - " - | 1.61 | 0.02 | 0.22 | 0.00 | - | - | - | - | -0.09 | 0.07 | 0.05 | 0.07 | 0.01 | 0.16 |
| LAb-3 | - " - | 3.53 | 0.01 | 4.12 | 0.0[illegible] | - | - | - | - | -0.22 | 0.07 | -0.22 | 0.07 | -0.36 | 0.16 |
| LAb-4 | - " - | 1.85 | 0.01 | 1.5[illegible] | 0.05 | - | - | - | - | - | - | - | - | - | - |
| LAb-5 | - " - | 3.21 | 0.03 | 4.17 | 0.04 | - | - | - | - | -0.04 | 0.07 | 0.01 | 0.07 | 0.05 | 0.16 |
| LAb-6 | - " - | 4.52 | 0.02 | 5.14 | 0.05 | - | - | - | - | 0.20 | 0.07 | -0.09 | 0.07 | -0.07 | 0.16 |
| LAb-7 | - " - | 4.62 | 0.01 | 4.88 | 0.07 | - | - | - | - | -0.23 | 0.07 | - | - | - | - |
| LAb-8 | - " - | 3.41 | 0.02 | 6.06 | 0.04 | - | - | - | - | - | - | -0.14 | 0.07 | -0.25 | 0.16 |
| BHVO-2 | - | - | - | - | - | - | - | - | - | 0.18 | 0.07 | 0.04 | 0.07 | 0.06 | 0.16 |

[1] Number of measurements (for details see sub-section *4.9*).
[2] In order to provide direct comparability within the multi-isotope data set of this study, we added to the usual and significant 95% confidence the classical SE level.
[3] Calculated on replicate measurements of the bracketing standard NIST SRM 683.
[4] Calculated on replicate measurements of the bracketing standard IRMM-14.
[5] Not measured.

| Sample ID | Location | $^{87}Sr/^{86}Sr$ | 2SD | $(^{230}Th/^{232}Th)$[6] | 2SD | $^{238}U/^{232}Th$ (activity | 2SD | $^{234}U/^{238}U$ (activit | 2SD | $^{232}Th/^{238}U$ (activity | 2SD | $^{230}Th/^{238}U$ (activity | 2SD | Isochron age[7] (kyr | 2SD | $\delta^{234}U^{9}$ (initia | 2SD |
|---|---|---|---|---|---|---|---|---|---|---|---|---|---|---|---|---|---|

| | | | | | | | | | | | | | | | | | |
|---|---|---|---|---|---|---|---|---|---|---|---|---|---|---|---|---|---|
| | | | | (activity) | | ) | y) | | ) | | ) | | B.P.[8]) | | l) | | |
| LAs-1 | Lake Asal | 0.705413 | 0.000012 | 8.99 | 0.04 | 44.69 | 0.08 | 1.521 | 0.0001 | 0.02238 | 0.00004 | 0.201 | 0.001 | 13.7 | 1.2 | 554 | 13 |
| LAs-2 | - " - | 0.705408 | 0.000009 | 15.30 | 0.11 | 76.14 | 0.15 | 1.520 | 0.0001 | 0.01313 | 0.00003 | 0.201 | 0.001 | 14.4 | 0.7 | 548 | 8 |
| LAs-3 | - " - | 0.705630 | 0.000011 | 15.51 | 0.10 | 71.32 | 0.14 | 1.518 | 0.0001 | 0.01402 | 0.00003 | 0.218 | 0.001 | 15.6 | 0.7 | 550 | 9 |
| LAs-basalt | - " - | 0.704027 | 0.000017 | - | - | - | - | - | - | - | - | - | - | - | - | - | - |
| LAb-1 | Lake Abhe | 0.704021 | 0.000010 | 3.50 | 0.04 | 8.90 | 0.02 | 1.344 | 0.0001 | 0.11235 | 0.00027 | 0.394 | 0.005 | 20.9[10] | 3.2 | 355 | 10 |
| LAb-2 | - " - | 0.704082 | 0.000009 | 3.14 | 0.03 | 7.34 | 0.01 | 1.346 | 0.0001 | 0.13632 | 0.00027 | 0.428 | 0.004 | - | - | - | - |
| LAb-3 | - " - | 0.705637 | 0.000009 | 1.24 | 0.01 | 1.569 | 0.003 | 1.344 | 0.0001 | 0.63131 | 0.00137 | 0.788 | 0.003 | n.d. | - | - | - |
| LAb-4 | - " - | 0.704105 | 0.000010 | 8.67 | 0.04 | 44.12 | 0.08 | 1.522 | 0.0001 | 0.02267 | 0.00004 | 0.197 | 0.001 | 13.3 | 1.2 | 554 | 13 |
| LAb-5 | - " - | 0.705707 | 0.000021 | - | - | - | - | - | - | - | - | - | - | - | - | - | - |
| LAb-6 | - " - | 0.706104 | 0.000019 | - | - | - | - | - | - | - | - | - | - | - | - | - | - |
| LAb-7 | - " - | 0.706291 | 0.000025 | - | - | - | - | - | - | - | - | - | - | - | - | - | - |
| LAb-8 | - " - | 0.706142 | 0.000014 | - | - | - | - | - | - | - | - | - | - | - | - | - | - |
| BHVO-2 | - | 0.703470 | 0.000009 | - | - | - | - | - | - | - | - | - | - | - | - | - | - |

[6] All calculations of U-Th data have used the half-lives measured by Cheng et al. (2013).
[7] Two-point isochron ages were calculated using a sediment end-member at secular equilibrium (i.e., activity ratio = 1 ± 0.5; samples LAb-4, LAs-1, LAs-2, LAs-3). Ages were calculated using the program Isoplot/Ex 4.15 (Ludwig, 2011) using a Monte Carlo simulation of 1000 steps for error calculation.
[8] B.P. stands for "Before Present", where the "Present" is defined as the year 1950 A.D.
[9] Initial $\delta^{234}U = ([^{234}U/^{238}U]_{activity} - 1)x1000$, based on isochron $^{230}Th$ age and corrected from detrital contamination.
[10] A mean isochron age was calculated for samples LAb-1 and LAb-2.

**Table 7** Isotope composition of the investigated fluid samples from the Afar Rift.

| Sample ID | Site ID | Location | Sample type | $\delta^{13}C_{DIC}$ (‰ VPDB) | SD (‰) | $\delta^{18}O_{H2O}$ (‰ VSMOW) | SD (‰) | $\delta^{34}S_{SO4}$ (‰ VCDT) | SD (‰) | $\delta^{44/40}Ca_{NIST\ SRM\text{-}915a}$ (‰) | 95% conf. (‰) | n[1] | SE (‰) |
|---|---|---|---|---|---|---|---|---|---|---|---|---|---|
| 1 | Site 1 | Ghoubbet-al-Kharab | seawater | -2.89 | 0.04 | 0.85 | 0.13 | 20.7 | 0.3 | -[2] | - | - | - |
| C1-5 (0 m) | C1 | Lake Asal | lake water | 6.27 | 0.29 | 4.21 | 0.35 | 19.6 | 0.3 | 1.47 | 0.08 | 3 | 0.03 |
| C1-4 (5 m) | C1 | Lake Asal | lake water | 6.74 | 0.1 | 4.36 | 0.02 | 19.3 | 0.3 | 1.22 | 0.13 | 6 | 0.0 |

| | | | | | | | | | | | | | |
|---|---|---|---|---|---|---|---|---|---|---|---|---|---|
| | | | | | 4 | | | | | | | | 7 |
| C1-3 (10 m) | C1 | Lake Asal | lake water | 6.53 | 0.12 | 4.43 | 0.12 | 19.2 | 0.3 | 1.55 | 0.14 | 4 | 0.06 |
| C1-2 (15 m) | C1 | Lake Asal | lake water | 6.75 | 0.02 | 4.36 | 0.13 | 19.1 | 0.3 | 1.64 | 0.10 | 7 | 0.05 |
| C1-1 (23 m) | C1 | Lake Asal | lake water | 6.93 | 0.18 | 4.02 | 0.39 | 19.0 | 0.3 | 1.63 | 0.18 | 6 | 0.09 |
| C2-4 (0 m) | C2 | Lake Asal | lake water | 6.42 | 0.46 | 4.50 | 0.55 | 19.4 | 0.3 | - | - | - | - |
| C2-3 (5 m) | C2 | Lake Asal | lake water | 7.30 | 0.02 | 4.74 | 0.05 | 19.6 | 0.3 | - | - | - | - |
| C2-2 (10 m) | C2 | Lake Asal | lake water | 6.51 | 0.67 | 4.27 | 0.61 | 19.1 | 0.3 | - | - | - | - |
| C2-1 (22 m) | C2 | Lake Asal | lake water | 6.13 | 0.22 | 4.40 | 0.06 | 19.3 | 0.3 | - | - | - | - |
| 3-1-nov | Site 3-1 | Lake Asal | hot pond water | - | - | - | - | 9.9 | 0.3 | - | - | - | - |
| 3-nov | Site 3 | Lake Asal | hydrothermal fluid | -2.73 | 0.03 | 2.79 | 0.14 | 10.9 | 0.3 | 0.91 | 0.09 | 4 | 0.04 |
| 3-nov 1/2[2] | Site 3 | Lake Asal | hydrothermal fluid | - | - | - | - | - | - | 0.93 | 0.14 | 6 | 0.07 |
| Site 10 lake | Site 10 | Lake Abhé | lake water | -1.03 | 0.56 | 5.97 | 0.26 | - | - | 2.84 | 0.17 | 6 | 0.08 |
| hot spring 1 | Site 11 | Lake Abhé | hydrothermal fluid | -6.34 | 0.13 | -2.82 | 0.21 | - | - | 0.93 | 0.09 | 6 | 0.04 |
| hot spring 2 | Site 14 | Lake Abhé | hydrothermal fluid | -9.02 | 0.15 | -2.93 | 0.20 | - | - | 0.74 | 0.11 | 7 | 0.06 |
| hot spring 2 1/2[3] | Site 14 | Lake Abhé | hydrothermal fluid | - | - | - | - | - | - | 0.77 | 0.11 | 6 | 0.06 |
| IAPSO[4] | - | - | - | - | - | - | - | - | - | 1.85 | 0.17 | 9 | 0.09 |

[1] Number of measurements (for details see sub-section *4.9*).
[2] Not measured.
[3] Whole procedure duplicates done on half of the amount of the original sample (for details see sub-section *4.9*).
[4] Mean seawater standard.

| Sample ID | Site ID | Location | Sample type | $\delta^{66/64}Zn_{NIST\ SRM-683}$ (‰) | 2SD[5] (‰) | $\delta^{56/54}Fe_{IRMM-14}$ (‰) | 2SD[6] (‰) | $\delta^{57/54}Fe_{IRMM-14}$ (‰) | 2SD[6] (‰) | $^{87}Sr/^{86}Sr$ | 2SD |
|---|---|---|---|---|---|---|---|---|---|---|---|
| 1 | Site 1 | Ghoubbet-al-Kharab | seawater | - | - | - | - | - | - | 0.709159 | - |
| C1-5 (0 m) | C1 | Lake Asal | lake water | 0.02 | 0.07 | - | - | - | - | 0.706619 | 0.000036 |
| C1-4 (5 m) | C1 | Lake Asal | lake water | -0.06 | 0.07 | - | - | - | - | 0.706625 | 0.000016 |

| | | | | | | | | | | | |
|---|---|---|---|---|---|---|---|---|---|---|---|
| C1-3 (10 m) | C1 | Lake Asal | lake water | -0.07 | 0.07 | - | - | - | - | 0.706596 | 0.000018 |
| C1-2 (15 m) | C1 | Lake Asal | lake water | -0.04 | 0.07 | - | - | - | - | 0.706618 | 0.000018 |
| C1-1 (23 m) | C1 | Lake Asal | lake water | -0.15 | 0.07 | - | - | - | - | 0.706595 | 0.000036 |
| C2-4 (0 m) | C2 | Lake Asal | lake water | - | - | - | - | - | - | - | - |
| C2-3 (5 m) | C2 | Lake Asal | lake water | - | - | - | - | - | - | - | - |
| C2-2 (10 m) | C2 | Lake Asal | lake water | - | - | - | - | - | - | - | - |
| C2-1 (22 m) | C2 | Lake Asal | lake water | - | - | - | - | - | - | - | - |
| 3-1-nov | Site 3-1 | Lake Asal | hot pond water | - | - | - | - | - | - | 0.704387 | 0.000020 |
| 3-nov | Site 3 | Lake Asal | hydrothermal fluid | - | - | - | - | - | - | 0.704396 | 0.000010 |
| Site 10 lake | Site 10 | Lake Abhé | lake water | - | - | -0.68 | 0.07 | -0.97 | 0.16 | 0.706697 | 0.000035 |
| hot spring 1 | Site 11 | Lake Abhé | hydrothermal fluid | 0.26 | 0.04 | - | - | - | - | 0.703773 | 0.000052 |
| hot spring 2 | Site 14 | Lake Abhé | hydrothermal fluid | | - | - | - | - | - | 0.703744 | 0.000017 |

[5] Calculated on replicate measurements of the bracketing standard NIST SRM-683.
[6] Calculated on replicate measurements of the bracketing standard IRMM-14.

**Table 8** Elemental ratios in the investigated fluid samples from the Afar Rift.

| Sample ID | Site ID | Location | Sample type | Na/Cl | K/Cl | Ca/Cl | Mg/Cl | $SO_4$/Cl | Br/Cl | Reference |
|---|---|---|---|---|---|---|---|---|---|---|
| | | | seawater, average | 0.5566 | 0.0206 | 0.0213 | 0.0663 | 0.1400 | 0.0035 | Millero, 2003 |
| 1 | Site 1 | Ghoubbet-al-Kharab | seawater | 0.5271 | 0.0265 | 0.0203 | 0.0664 | 0.1414 | -[1] | This study |
| C1-5 (0 m) | C1 | Lake Asal | lake water | 0.2231 | 0.0135 | 0.0074 | 0.0300 | 0.0132 | 0.0030 | This study |
| C1-1 (23 m) | C1 | Lake Asal | lake water | 0.2375 | 0.0143 | 0.0078 | 0.0319 | 0.0120 | 0.0033 | This study |
| 3-1-nov | Site 3-1 | Lake Asal | hot pond water | 0.3102 | 0.0163 | 0.1084 | 0.0128 | 0.0116 | 0.0030 | This study |
| 3-nov | Site 3 | Lake Asal | hydrothermal fluid | 0.3135 | 0.0170 | 0.1006 | 0.0147 | 0.0115 | 0.0031 | This study |
| Site 10 lake | Site 10 | Lake Abhé | lake water | 0.8648 | 0.0233 | 0.00005 | 0.00003 | 0.4631 | - | This study |

| | | | | | | | | | | |
|---|---|---|---|---|---|---|---|---|---|---|
| hot spring 1 | Site 11 | Lake Abhé | hydrothermal fluid | 0.6270 | 0.0233 | 0.1503 | - | 0.1667 | - | This study |

[1] Not measured.

**Table 9** Chemistry of the end-member hydrothermal fluid, Lake Asal.

| | end-member hydrothermal fluid, Lake Asal[1] | seafloor hydrothermal fluids, overall range[2] |
|---|---|---|
| $^{87}Sr/^{86}Sr$ | 0.704184 | |
| Y (ppb) | 0.004 | |
| Cd | 2.40 | 0 - 20.2 |
| La | 0.031 | |
| Ce | 0.006 | |
| Nd | 0.002 | |
| U | 0.01[3] | |
| V | 74.0 | |
| Mn | 411 | 549 - 390060 |
| Fe | 24.0 | 391 to 1396250 |
| Co | 0.20 | <0.30 - 831 |
| Ni | 2.01 | 129 - 211 |
| Cu | 5.01 | 0 - 10295 |
| Zn | 1.23[3] | 0 - 196140 |
| Mo | 24.1 | |
| Pb | 0.08 | <4.14 - 808 |
| Ag | 0.35 | <0.11 - 24.8 |
| Sn | 0.15 | |

[1] Calculated from the estimation that the hydrothermal fluid venting at Site 3 is a mix of 97% actual end-member hydrothermal fluid and 3% lake water

[2] German and Von Damm (2006)

[3] Due to the accumulation of these elements in the lake water their contents in there are two orders of magnitude higher than those in the Site 3 hydrothermal fluid. Thus, the calculated concentrations in the end-member fluid are negative. Therefore, we use the concentrations of these elements in Site 3 hydrothermal fluid.

**Table 10** Metals accumulated in the Lake Asal water.

| | average concentration in Lake Asal water (mg/kg) | metals accumulated in Lake Asal water[1] (t) |
|---|---|---|
| Li | 6.290000 | 2516.000 |
| Mn | 1.026399 | 410.560 |
| Zn | 0.483303 | 193.321 |
| Cu | 0.011954 | 4.782 |
| Mo | 0.009632 | 3.853 |
| Fe | 0.007847 | 3.139 |
| Ni | 0.002256 | 0.903 |
| V | 0.002250 | 0.900 |
| U | 0.001061 | 0.424 |
| Pb | 0.000956 | 0.383 |
| Co | 0.000682 | 0.273 |
| Sn | 0.000532 | 0.213 |
| Cd | 0.000028 | 0.011 |
| Ag | 0.000019 | 0.008 |
| La | 0.000009 | 0.004 |
| Y | 0.000008 | 0.003 |
| Ce | 0.000006 | 0.002 |
| Nd | 0.000004 | 0.002 |
| Pr | 0.000001 | 0.0004 |

[1] Calculated using the average metal concentration in the Lake Asal water and the water volume of Lake Asal, 400 million $m^3$ (400000 million kg)

Highlights:

- Lake Asal (Afar Rift) is fed by seafloor-type hydrothermal fluids
- An oceanic “embryo” in arid climate is mildly acidic and metal rich
- It has heavy C, O and Ca, and light Zn isotope composition
- Lake chemistry is controlled by hydrothermal discharge and aeolian input

Figure 1

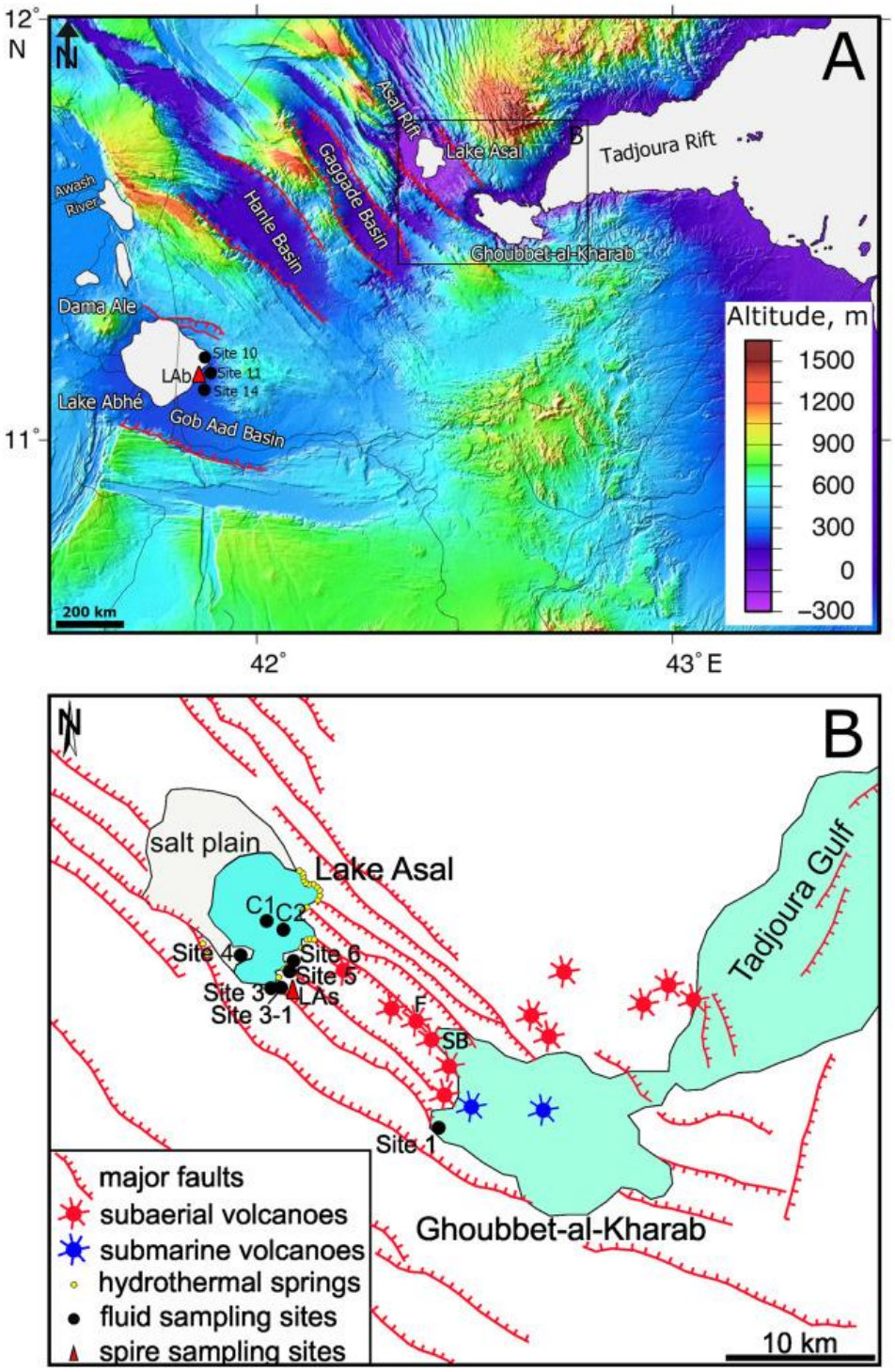
A
12° N
11°
42°
43° E
Asal Rift
Lake Asal
B
Tadjoura Rift
Awash River
Hanle Basin
Gaggade Basin
Ghoubbet-al-Kharab
Dama Ale
Site 10
LAb
Site 11
Site 14
Lake Abhé
Gob Aad Basin
Altitude, m
1500
1200
900
600
300
0
−300
200 km
B
salt plain
Lake Asal
Tadjoura Gulf
C1
C2
Site 4
Site 6
Site 5
Site 3
LAs
Site 3-1
F
SB
Site 1
Ghoubbet-al-Kharab
major faults
subaerial volcanoes
submarine volcanoes
hydrothermal springs
fluid sampling sites
spire sampling sites
10 km

Figure 2

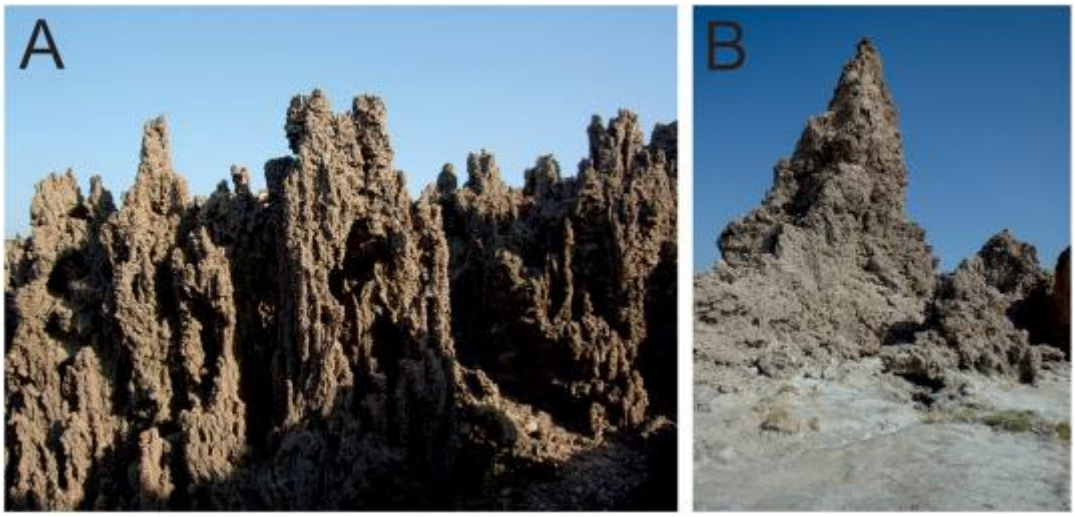


Figure 3

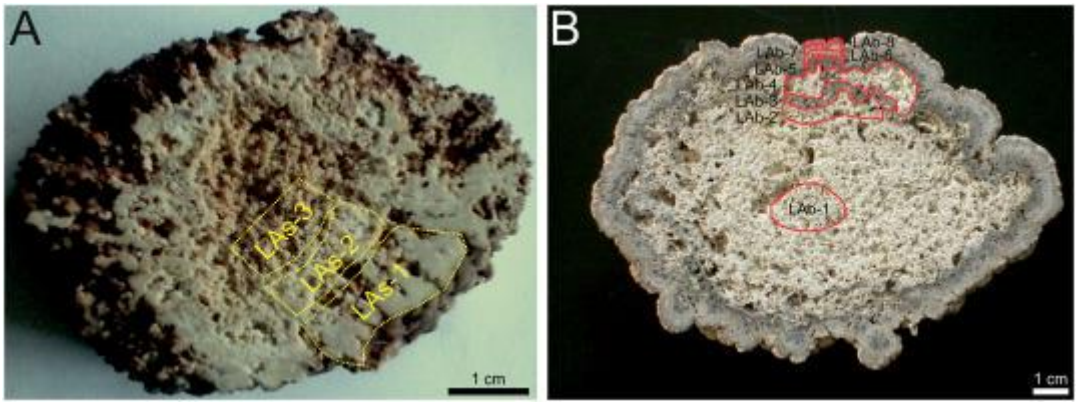

Figure 4

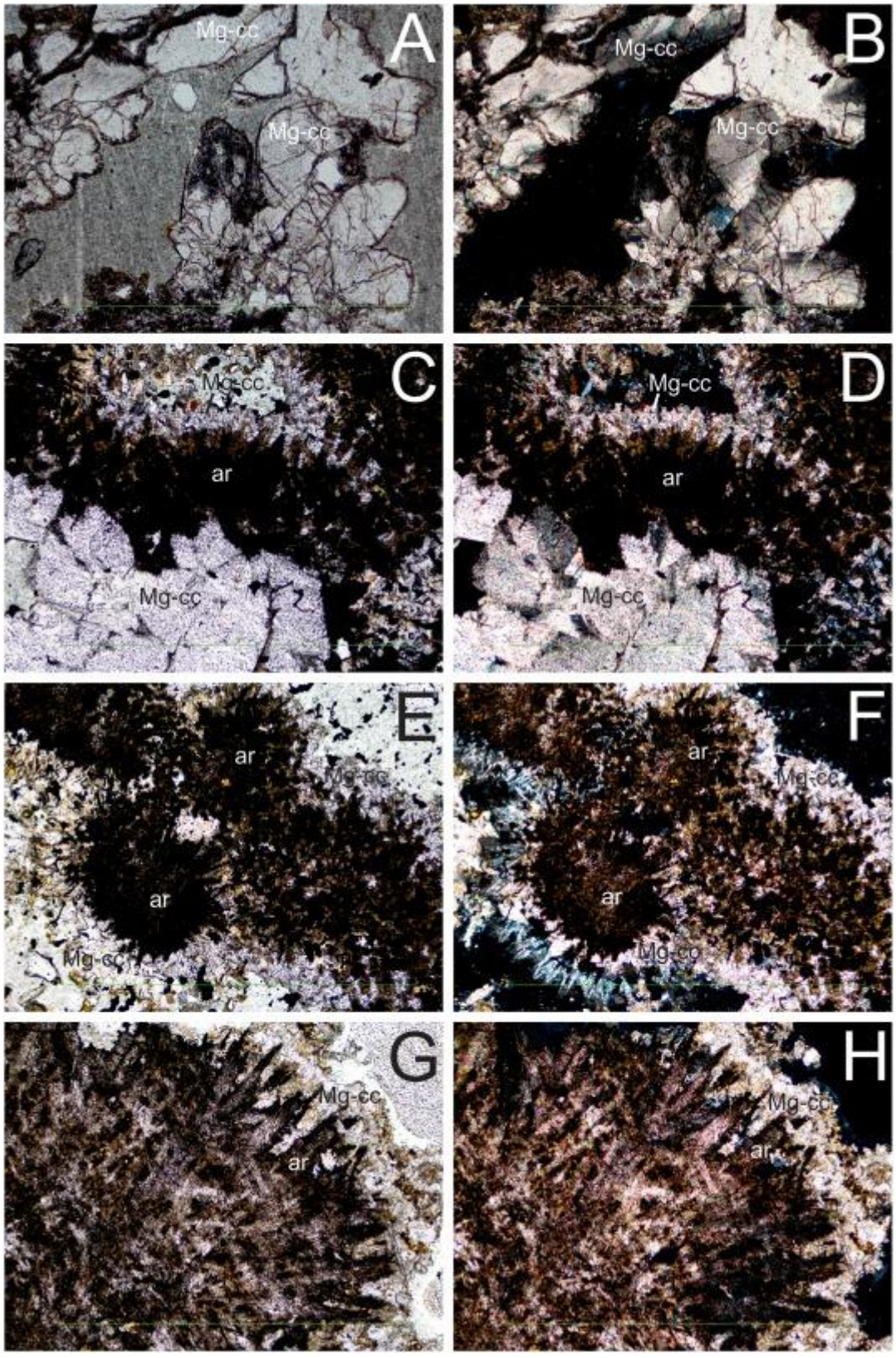
A
Mg-cc
Mg-cc
B
Mg-cc
Mg-cc
C
Mg-cc
ar
Mg-cc
D
Mg-cc
ar
Mg-cc
E
ar
ar
Mg-cc
F
ar
ar
Mg-cc
G
Mg-cc
ar
H
Mg-cc
ar

Figure 5

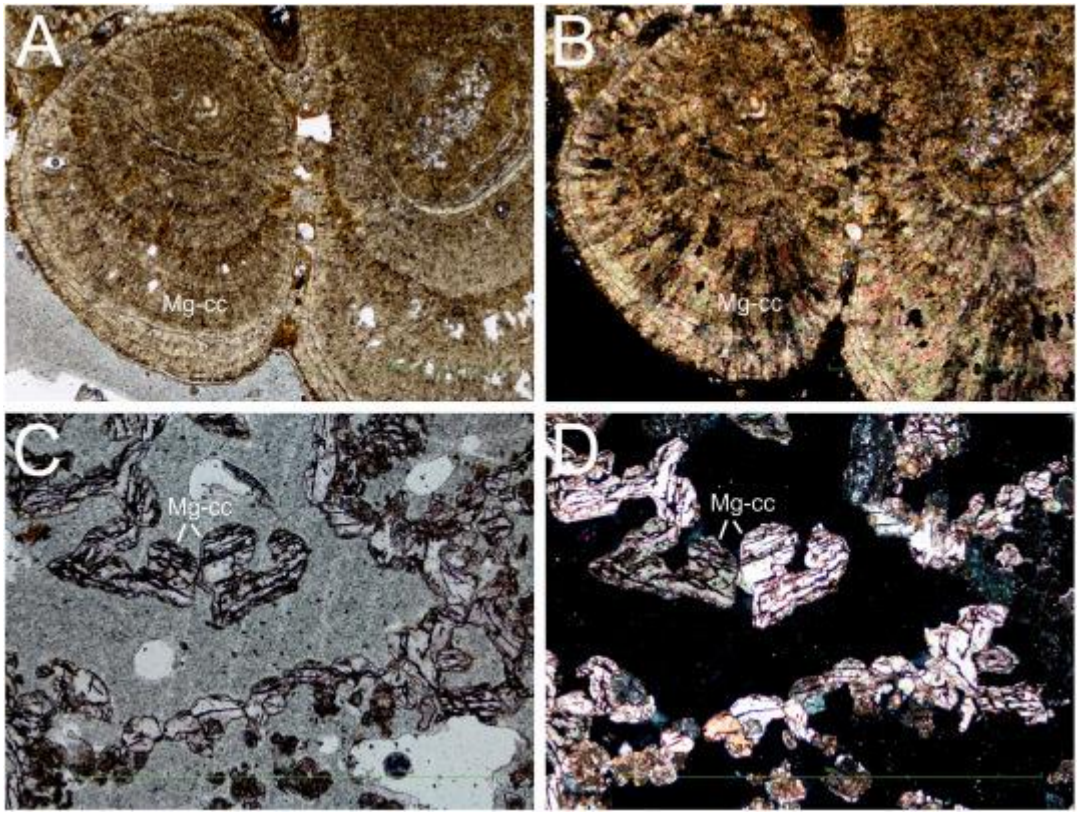

Figure 6

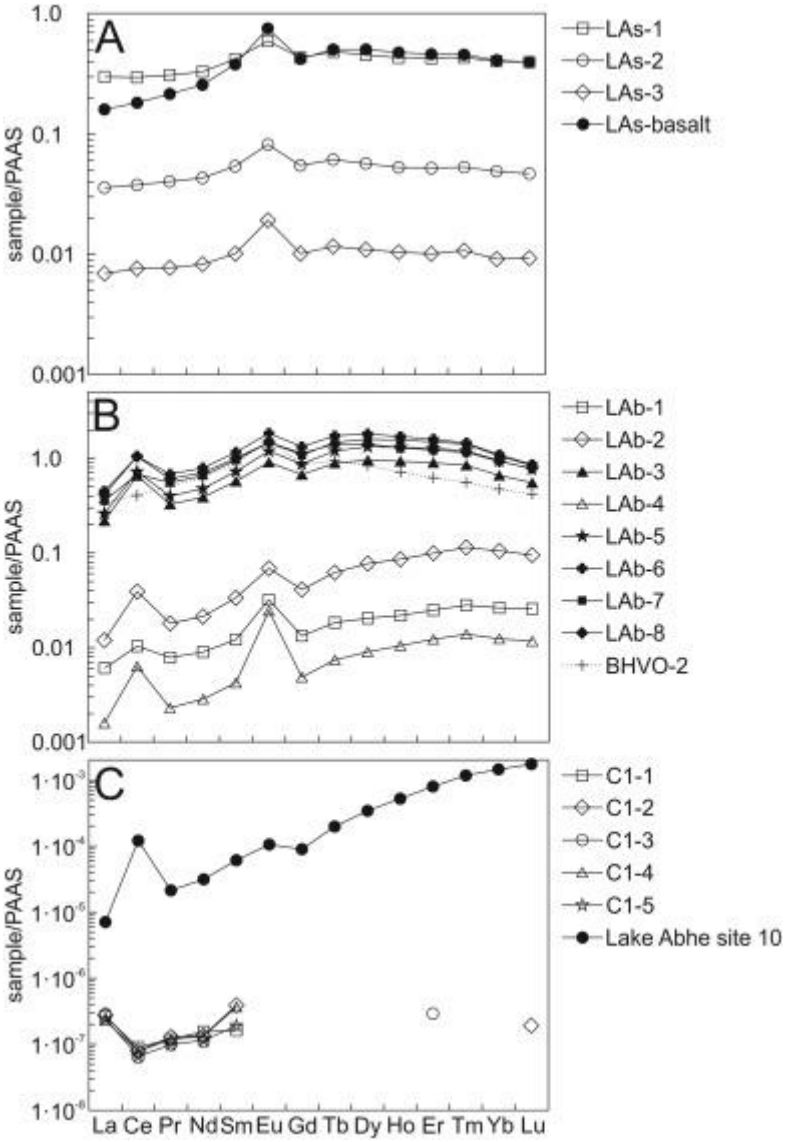
A
B
C
sample/PAAS
1.0
0.1
0.01
0.001
LAs-1
LAs-2
LAs-3
LAs-basalt
LAb-1
LAb-2
LAb-3
LAb-4
LAb-5
LAb-6
LAb-7
LAb-8
BHVO-2
C1-1
C1-2
C1-3
C1-4
C1-5
Lake Abhe site 10
La Ce Pr Nd Sm Eu Gd Tb Dy Ho Er Tm Yb Lu

Figure 7

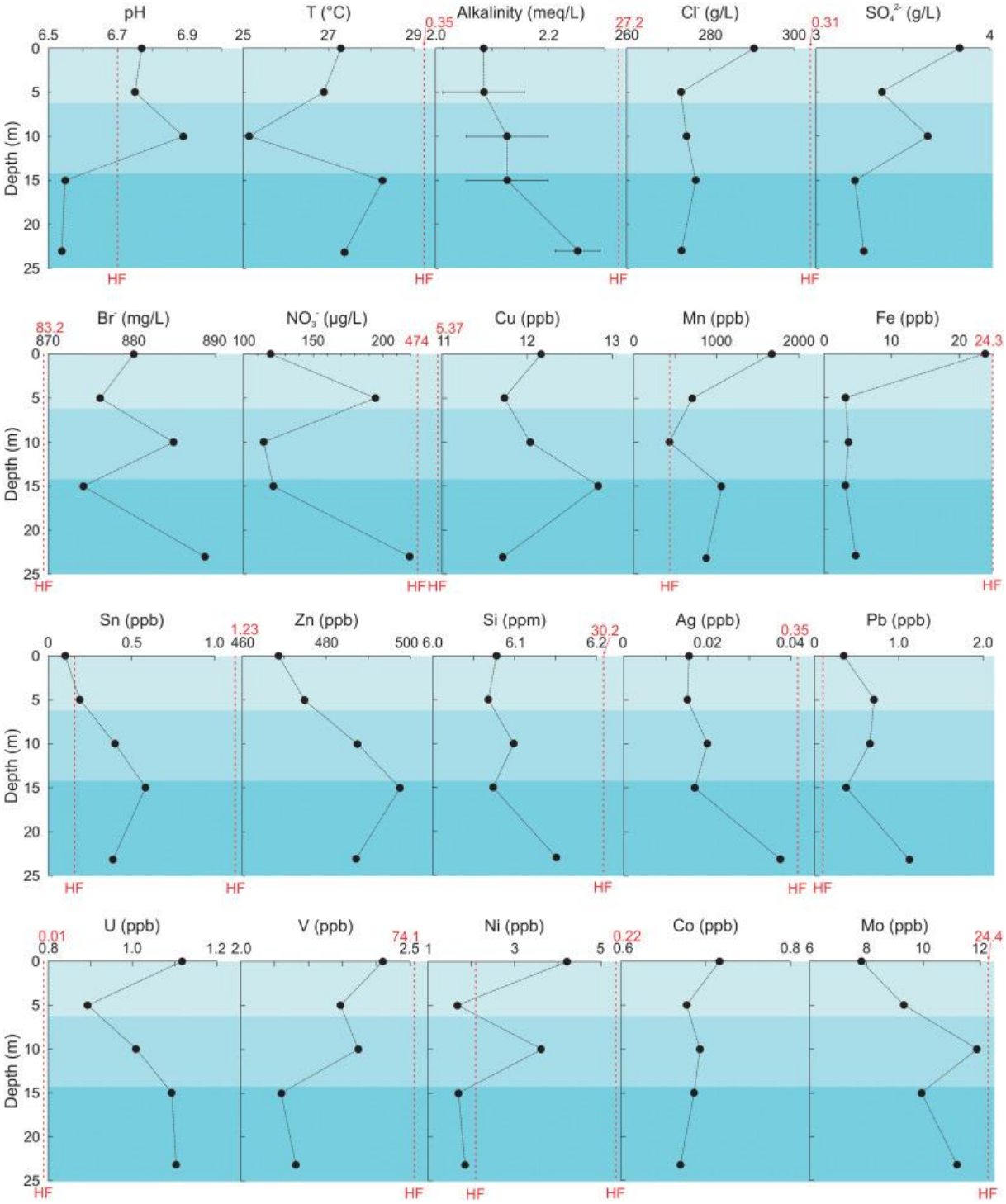
pH
6.5
6.7
6.9
T (°C)
25
27
29
0.35
Alkalinity (meq/L)
2.0
2.2
27.2
Cl⁻ (g/L)
260
280
300
0.31
SO4 2- (g/L)
3
4
Depth (m)
0
5
10
15
20
25
HF
Br⁻ (mg/L)
83.2
870
880
890
NO3⁻ (µg/L)
100
150
200
474
5.37
Cu (ppb)
11
12
13
Mn (ppb)
0
1000
2000
Fe (ppb)
10
20
24.3
Sn (ppb)
0
0.5
1.0
1.23
Zn (ppb)
460
480
500
Si (ppm)
6.0
6.1
6.2
30.2
Ag (ppb)
0.02
0.04
0.35
Pb (ppb)
1.0
2.0
U (ppb)
0.01
0.8
1.0
1.2
V (ppb)
2.0
2.5
74.1
Ni (ppb)
1
3
5
Co (ppb)
0.22
0.6
0.8
Mo (ppb)
6
8
10
12
24.4

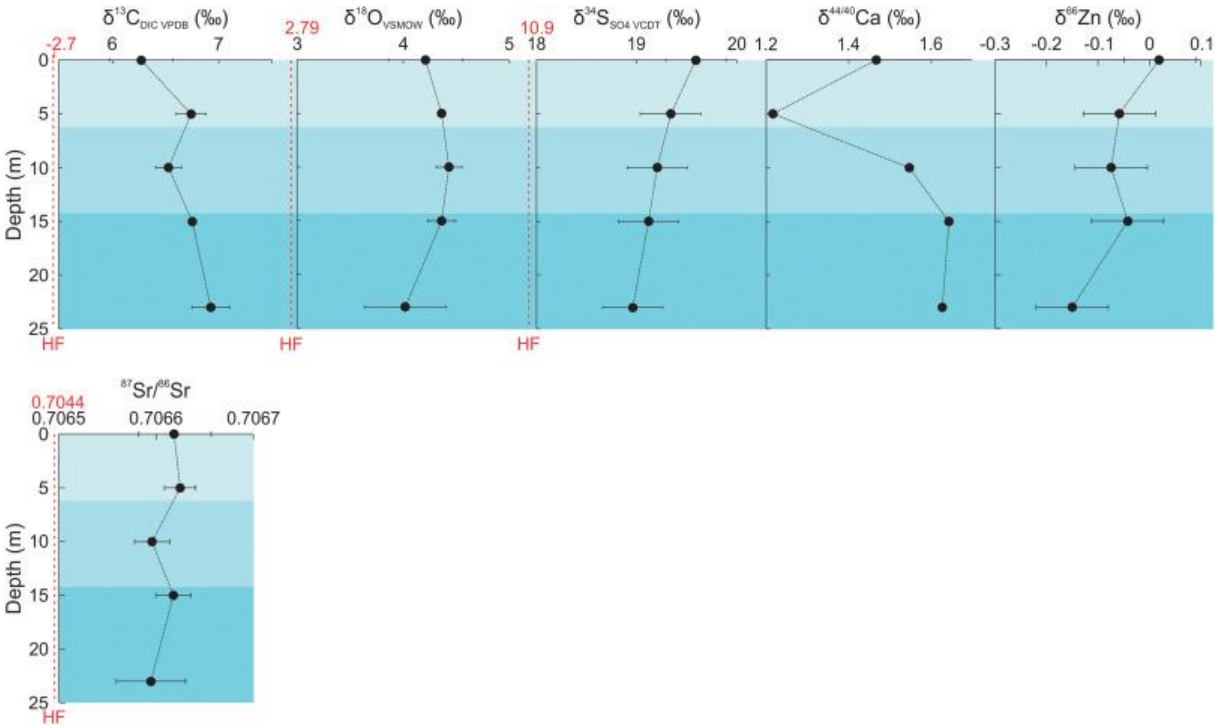
δ13CDIC VPDB (‰)
δ18OVSMOW (‰)
δ34SSO4 VCDT (‰)
δ44/40Ca (‰)
δ66Zn (‰)
-2.7
2.79
10.9
Depth (m)
HF
87Sr/86Sr
0.7044
0.7065
0.7066
0.7067

Figure 8

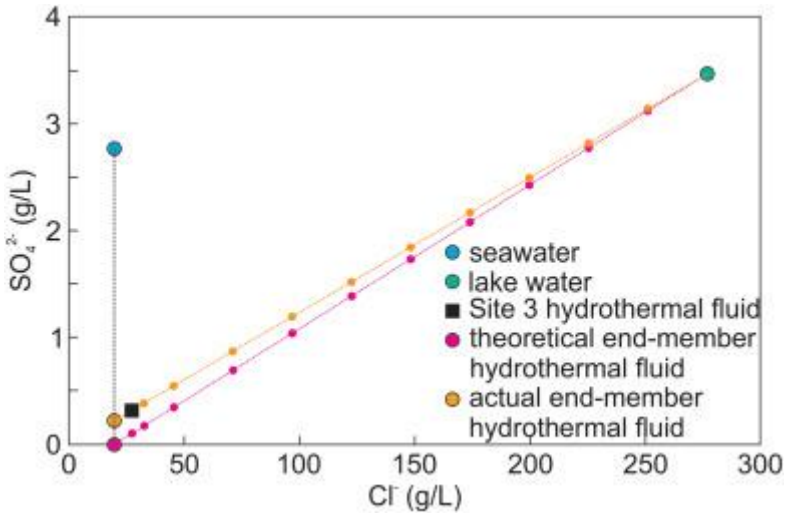
SO4 2- (g/L)
Cl- (g/L)
seawater
lake water
Site 3 hydrothermal fluid
theoretical end-member hydrothermal fluid
actual end-member hydrothermal fluid

Figure 9

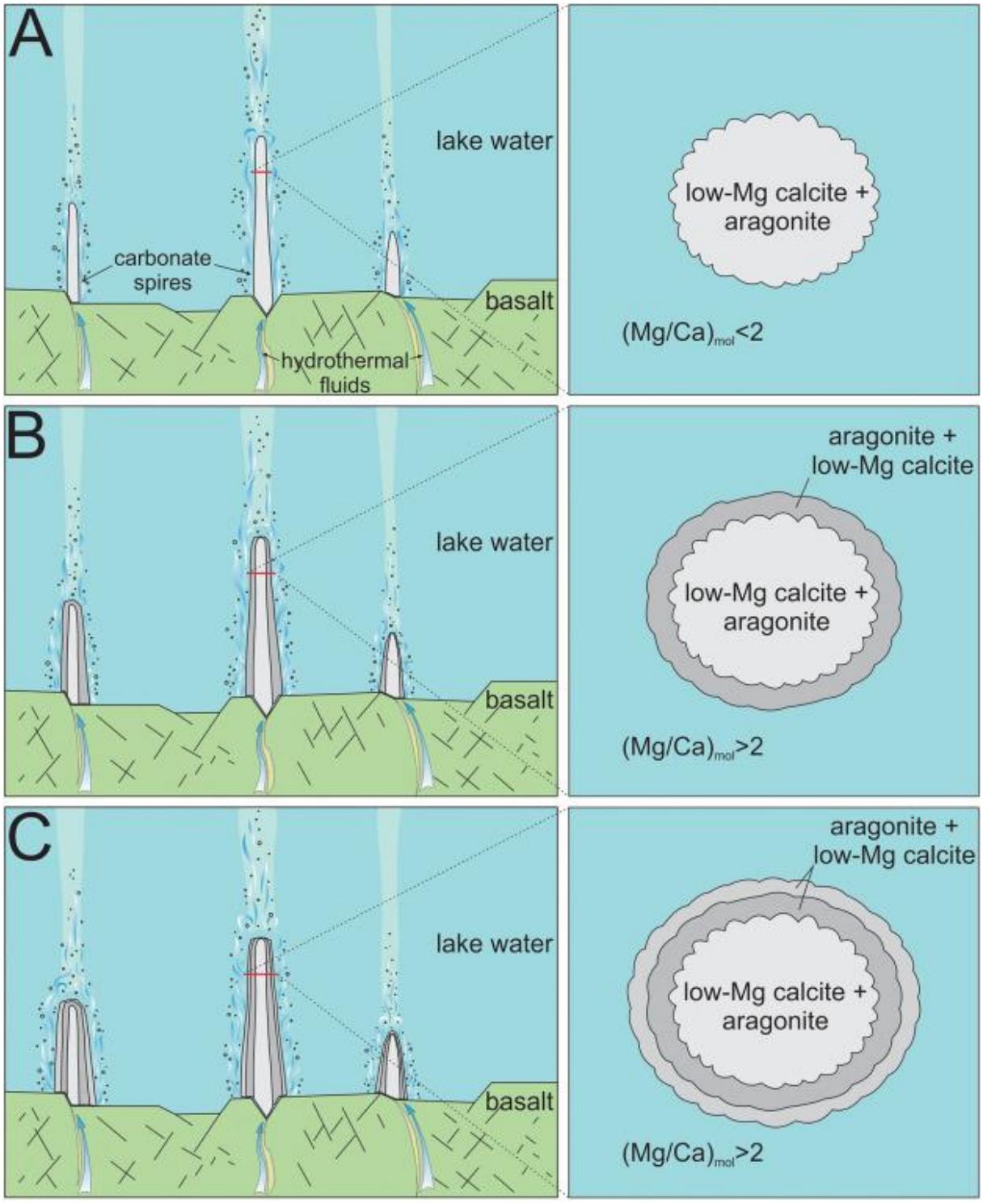
A
lake water
carbonate spires
basalt
hydrothermal fluids
low-Mg calcite + aragonite
(Mg/Ca)mol<2
B
lake water
basalt
aragonite + low-Mg calcite
low-Mg calcite + aragonite
(Mg/Ca)mol>2
C
lake water
basalt
aragonite + low-Mg calcite
low-Mg calcite + aragonite
(Mg/Ca)mol>2

Figure 10

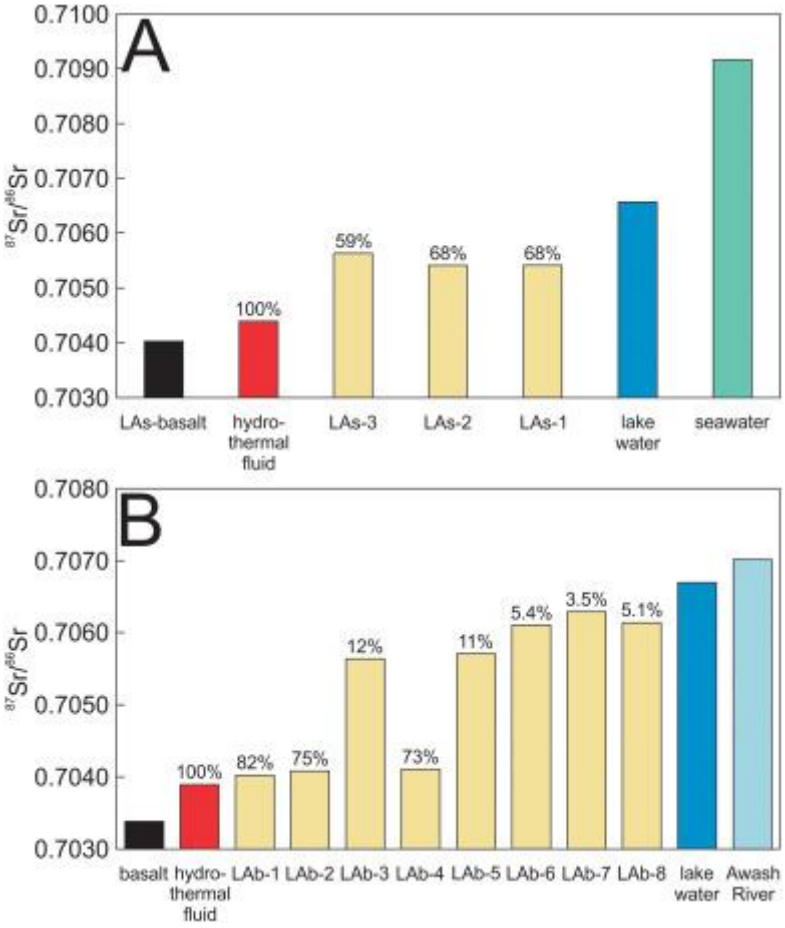
A
0.7100
0.7090
0.7080
0.7070
0.7060
0.7050
0.7040
0.7030
$^{87}Sr/^{86}Sr$
100%
59%
68%
68%
LAs-basalt
hydro-thermal fluid
LAs-3
LAs-2
LAs-1
lake water
seawater
B
0.7080
0.7070
0.7060
0.7050
0.7040
0.7030
$^{87}Sr/^{86}Sr$
100%
82%
75%
12%
73%
11%
5.4%
3.5%
5.1%
basalt
hydro-thermal fluid
LAb-1
LAb-2
LAb-3
LAb-4
LAb-5
LAb-6
LAb-7
LAb-8
lake water
Awash River

Figure 11

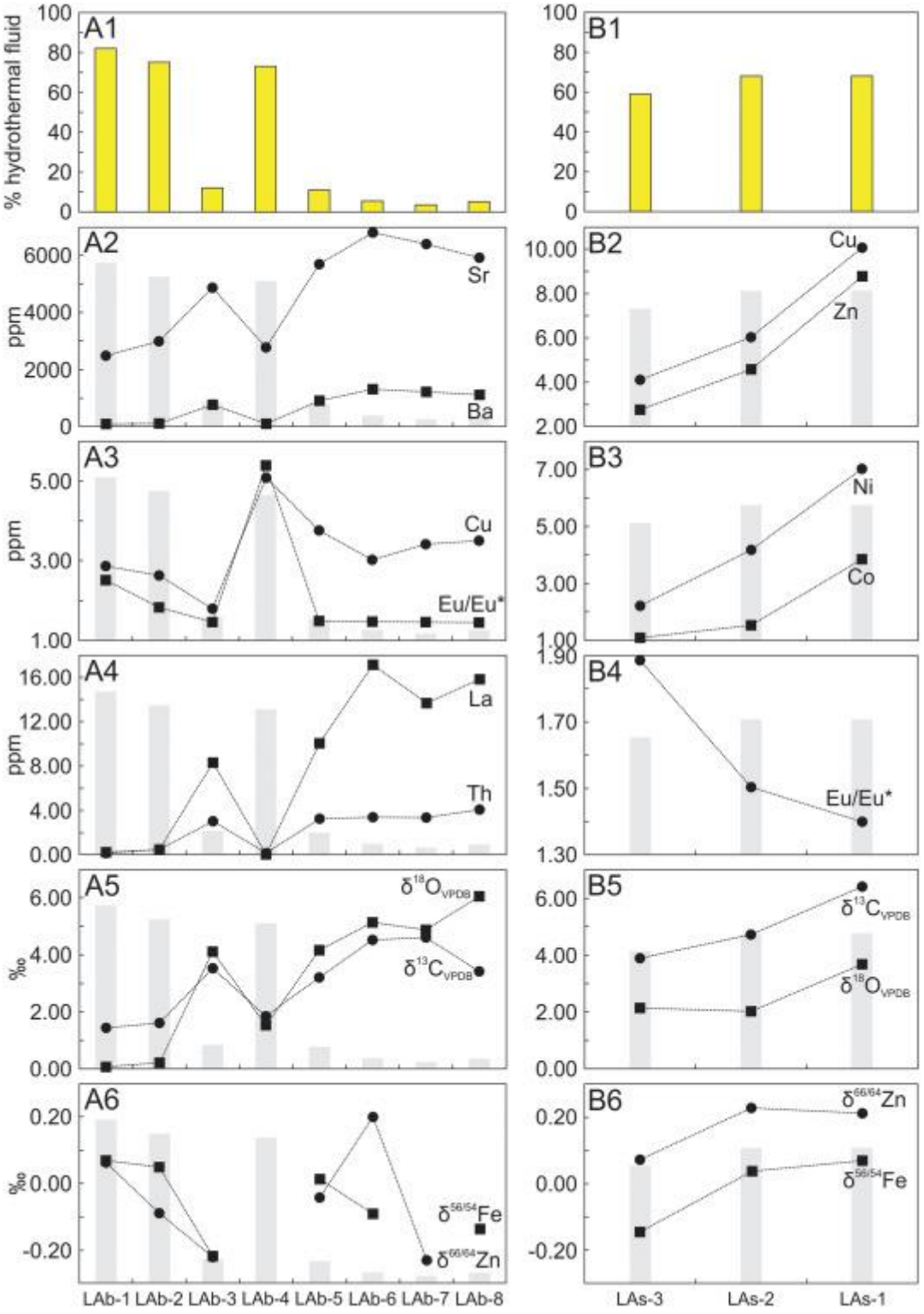
A1
% hydrothermal fluid
B1
A2
ppm
Sr
Ba
B2
Cu
Zn
A3
ppm
Cu
Eu/Eu*
B3
Ni
Co
A4
ppm
La
Th
B4
Eu/Eu*
A5
‰
δ18OVPDB
δ13CVPDB
B5
δ13CVPDB
δ18OVPDB
A6
‰
δ56/54Fe
δ66/64Zn
B6
δ66/64Zn
δ56/54Fe
LAb-1 LAb-2 LAb-3 LAb-4 LAb-5 LAb-6 LAb-7 LAb-8
LAs-3 LAs-2 LAs-1

Figure 12

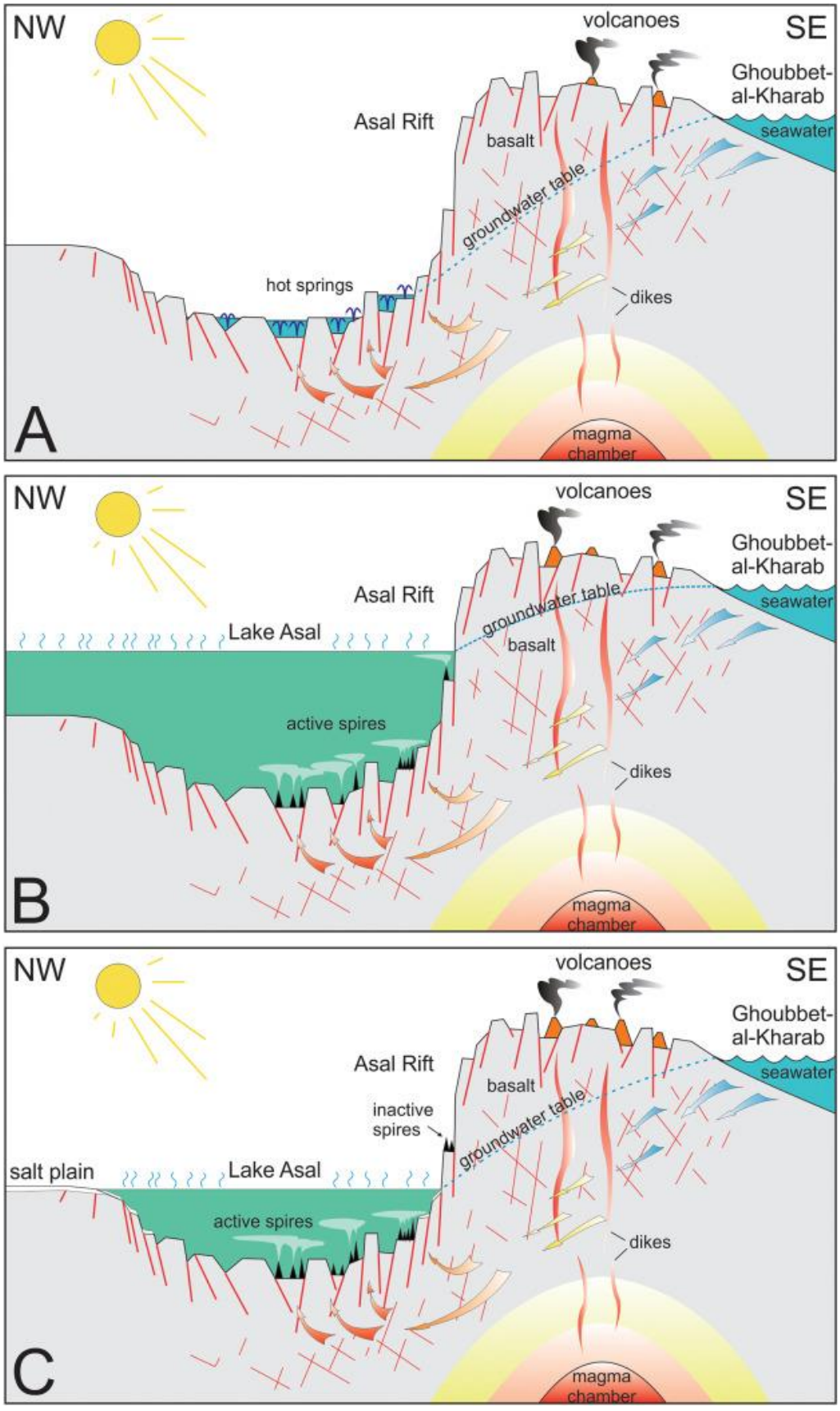
NW
volcanoes
SE
Ghoubbet-
al-Kharab
Asal Rift
basalt
seawater
groundwater table
hot springs
dikes
A
magma
chamber
NW
volcanoes
SE
Ghoubbet-
al-Kharab
Asal Rift
groundwater table
seawater
Lake Asal
basalt
active spires
dikes
B
magma
chamber
NW
volcanoes
SE
Ghoubbet-
al-Kharab
Asal Rift
basalt
seawater
inactive
spires
groundwater table
salt plain
Lake Asal
active spires
dikes
C
magma
chamber

Figure 13

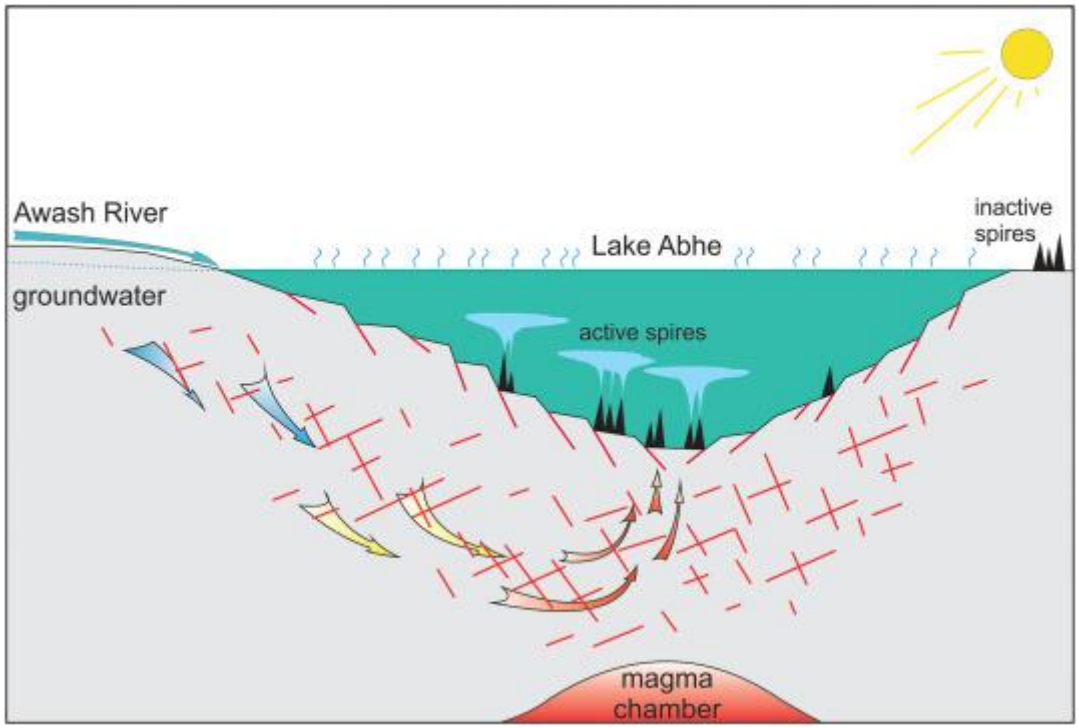
Awash River
Lake Abhe
inactive
spires
groundwater
active spires
magma
chamber